Novel methods for subcellular *in vivo* imaging of the cornea with the Rostock Cornea Module 2.0

Kumulative Dissertation

zur

Erlangung des akademischen Grades

doctor rerum naturalium (Dr. rer. nat.)

der Mathematisch-Naturwissenschaftlichen Fakultät

der Universität Rostock

Universität Rostock — Traditio et Innovatio

gegründet 1419

vorgelegt von

Sebastian Bohn, geb. am 23. Juni 1990 in Güstrow

aus Rostock

Rostock, 2021

Gutachter:

Prof. Dr. Heinrich Stolz
Universität Rostock, Institut für Physik

Univ.-Prof. Dr. Achim Langenbucher
Universität des Saarlandes, Institut für Experimentelle Ophthalmologie

Jahr der Einreichung: 2021
Jahr des Kolloquiums: 2021

Abstract

Corneal confocal laser scanning microscopy is an imaging technique offering early detection, assessment, and monitoring of various pathologies. These pathologies are not restricted to ocular diseases but also extend, for example, to various neuropathies. The Rostock Cornea Module, which transforms a laser scanning ophthalmoscope into a corneal laser scanning microscope, has played an important role in both clinical and scientific imaging of corneal cell layers for many years. In this cumulative dissertation, an improved version, the Rostock Cornea Module 2.0, was developed and tested in collaboration with the Department of Ophthalmology of the Rostock University Medical Center. Furthermore, this thesis covers several publications on the introduction of the module, its handling and imaging properties, novel methods for image acquisition and reconstruction, and results in different application areas. These include a concave contact cap design to attenuate eye movements, which improves volumetric image acquisition, three-dimensional volume reconstruction, and sectional imaging of corneal cell layers, an oscillating focal plane to improve large-area imaging of the subbasal nerve plexus, the integration of simultaneous optical coherence tomography, the wavelength dependence on corneal confocal microscopy, the clinical usage on healthy eyes and various pathologies, and the automated morphological characterization of corneal cell layers.

Zusammenfassung

Die korneale konfokale Laser-Scanning-Mikroskopie ist ein Bildgebungsverfahren, welches eine Früherkennung, Beurteilung und Verlaufskontrolle verschiedener Krankheitsbilder bietet. Diese Krankheitsbilder sind nicht auf Augenerkrankungen beschränkt, sondern erstrecken sich beispielsweise auch über diverse Neuropathien. Das Rostock Cornea Module, welches ein Laser-Scanning-Ophthalmoskop zu einem kornealen Laser-Scanning-Mikroskop transformiert, spielt diesbezüglich seit Jahren sowohl in der klinischen Anwendung als auch der Wissenschaft eine wichtige Rolle bei der Bildgebung der kornealen Zellschichten. Im Rahmen dieser kumulativen Dissertation wurde in Zusammenarbeit mit der Arbeitsgruppe Experimentelle Ophthalmologie der Universitätsmedizin Rostock eine verbesserte Version, das Rostock Cornea Module 2.0, entwickelt und erprobt. Darüber hinaus werden in mehreren Publikationen die Einführung des Moduls, seine Handhabungs- und Abbildungseigenschaften, neue Methoden zur Bildaufnahme und Bildrekonstruktion sowie Ergebnisse in verschiedenen Anwendungsgebieten behandelt. Darunter fallen ein konkaves Kontaktkappendesign zur Abschwächung der Augenbewegungen, welche die volumetrische Bildaufnahme, die dreidimensionale Volumenrekonstruktion und die Schnittbilderzeugung kornealer Zellschichten verbessert, eine oszillierende Fokusebene zur Verbesserung der großflächigen Abbildung des subbasalen Nervenplexus, die Möglichkeit zur Kombination mit anderen Bildgebungsverfahren wie der optischen Kohärenztomografie, Wellenlängenabhängigkeiten in der kornealen konfokalen Mikroskopie, der klinische Einsatz am gesunden Auge und verschiedenen Krankheitsbilder sowie die automatisierte morphologische Charakterisierung von kornealen Zellschichten.

Contents

Contents

List of abbreviations

List of Figures

Part I.

Dissertation thesis

1. Introduction

At 43 dpt, the cornea is the most refractive optical element of the eye, which has a total refractive power of 58.8 dpt under minimal accommodation [1]. Therefore, to receive a sharp optical image on the retina, the regular surface and transparency of the cornea play a major role. From the central to the peripheral area the average corneal thickness is about 550 µm to 700 µm, respectively [2]. As shown in Fig. 1.1, the cornea consists of several layers that are structured and arranged from anterior to posterior as follows [2, 3]:

- The corneal **epithelium** has a thickness of approximately 50 µm to 60 µm, is a nonkeratinized, stratified squamous epithelium, and consists of five to eight cell layers. Superficial cells are quite flattened and have microridges or micropliapses at their free surface. The deepest cells, the epithelial basal cells are anchored to the **basement membrane**. Furthermore, the epithelium is enriched in sensitive nerve endings.
- Beneath the basement membrane lies the **stroma**. Its most anterior substructure is the condensed, more or less amorphous, and 10 µm to 20 µm [4] thick **Bowman's layer**. Adjacent to this, the stroma continues as a sort of specialized transparent aponeurosis. The stromal cells are called keratocytes and are arranged with collagen fibers in many lamellae. In adjacent lamellae, the fibers cross at different angles, becoming orthogonal in the center of the cornea. The keratocytes are specialized fibroblasts that lie as flattened cells irregularly stellate between the lamellae. Their processes spread perpendicularly and parallel to the collagen fibers. The stroma does not contain any blood vessels or lymphatics, but numerous sensitive nerve endings.
- Following the stroma, there is a specialized basement membrane, the **Descemet's membrane**. It is 5 µm to 10 µm thick, a component of the

corneal endothelium, and homogeneous in younger individuals, whereas in older individuals cross bands appear in the anterior layer corresponding to a hexagonally arranged tropocollagen molecule. The endothelium is a simple squamous epithelium composed of metabolically active and highly interdigitated cells. Its cytoplasm contains moderately well-developed organelles and the nuclei are flattened.

All these corneal layers ensure with their various functions the preservation of the optical quality. The corneal epithelium serves as a barrier against the penetration of bacteria and foreign substances [2]. In the stroma, the keratocytes synthesize, besides the elastic and collagen fibers, the corneal ground substance. This substance contains high amounts of chondroitin and keratan sulfate, whereby the latter is responsible for the transparency [3]. Water from the stroma is removed by actively transporting sodium, potassium, and hydrogen carbonate ions from the endothelium into the anterior chamber. In addition, tight junctions protect the corneal stroma from water infiltration. Thus, the endothelium provides a pumping and sealing function [2].

Between the basal cells of the epithelium and their basal lamina lies the subbasal nerve plexus (SNP) [5]. This plexus comprises the densest part of the corneal innervation and forms a spiral or whorl-shaped pattern of nerve fibers oriented parallel to the surface. In the human cornea, the center of this spiral is located approximately 2 mm to 3 mm inferior and nasal to the corneal apex. The nerves in the SNP originate largely in widely distributed stromal nerves that penetrate Bowman's layer in the peripheral and intermediate areas of the cornea. After penetration, the stromal nerves immediately bend at a right angle and branch into 2 to 20 thinner nerve fascicles that correspond to the subbasal nerves. From the limbal plexus, additional subbasal nerves enter directly into the peripheral areas of the cornea. Finally, from the horizontally extending SNP, intraepithelial terminals ascend vertically or obliquely.

The ophthalmologist's routine instrument when examining a patient's cornea is the slit lamp, developed by Allvar Gullstrand in 1911 [7, 8]. In that year, he also received the Nobel Prize in medicine and physiology for his work in the field of dioptrics [9, 10]. Through further developments by Goldmann, Henker, Koeppe, Vogt, and others [11], the slit lamp advanced to become a universal
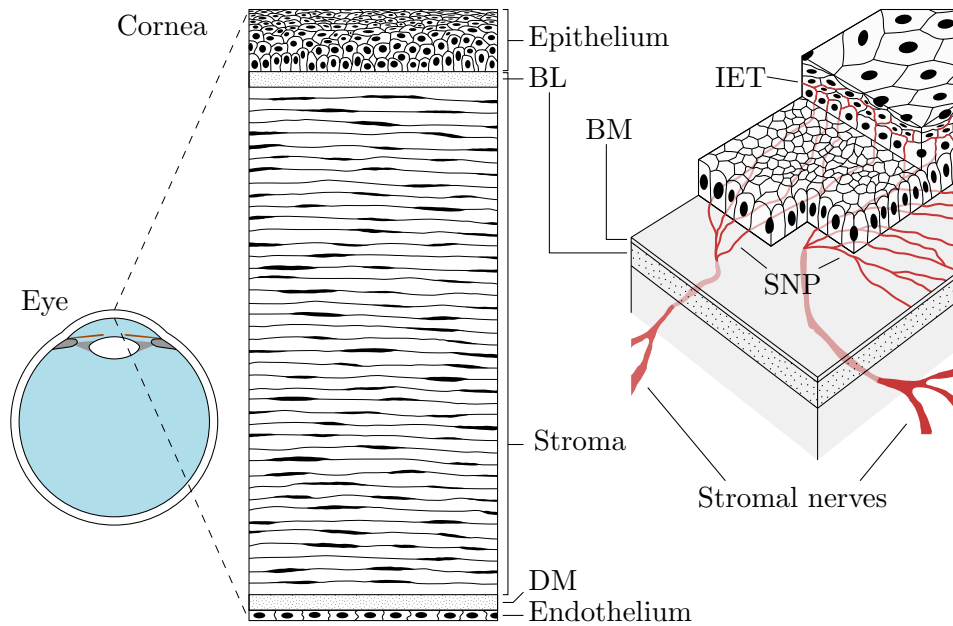
Figure 1.1.: Self-drawn sketches of corneal anatomy based on [3] and [6]. BL – Bowman's layer, BM – basement membrane, IET – intraepithelial terminals, DM – Descemet's membrane.

examination instrument in ophthalmology, which is still used versatilely for almost all segments of the eye [12, 13].

The slit lamp provides optical sectional images of the cornea with a magnification of up to 40x [13]. Using specular reflection, it is possible to resolve cell structures in the endothelium and quantify their density [14]. However, for subcellular resolution in all corneal layers, another imaging technique is generally used, namely, confocal laser scanning microscopy (CLSM). The combination of Heidelberg Retina Tomograph and Rostock Cornea Module (HRT-RCM; both Heidelberg Engineering GmbH, Heidelberg, Germany), which together provide a contact method for corneal CLSM, is often used for clinical and scientific investigations [15, 16]. The HRT-RCM was first introduced in 2002 [17]. Since then the use in the clinical field has focused on the diagnosis of acanthamoeba keratitis, the detection of keratomycosis, and the differential diagnosis and treatment planning of corneal dystrophies [15, 18–23].

In addition to these general clinical uses, research showed that CLSM reveals morphological changes in the corneal SNP due to various diseases as for ex-

ample, chronic migraine [24–26], trigeminal neuralgia [27], multiple sclerosis [28–31], familial amyloid neuropathy [32, 33], Parkinson's disease [34–37], and diabetic peripheral neuropathy [38–44]. Recently, the possibility of differentiating inflammatory from diabetic neuropathy was also demonstrated [45]. These studies show that corneal CLSM not only has its justified usage in ophthalmology but also offers a non-invasive diagnostic option for diseases affecting the nervous system. However, it is crucial to mention that the field of view (FOV) of a single CLSM image acquired with the HRT-RCM is relatively small (400 µm × 400 µm) and the nerve fibers are inhomogeneously distributed throughout the SNP [46]. Thus, multiple CLSM images from different locations within the SNP are necessary for sufficient morphological quantification [47, 48]. The group around Köhler *et al.* went one step further with their approach. They developed the EyeGuidance system, which is placed directly next to the HRT-RCM [49, 50]. During a corneal examination, the nonexamined eye looks at a fixation target moving along an expanding spiral path. As a result, the examined eye also follows this spiral path while single SNP images are continuously recorded. The spiral path is defined in such a way that the SNP images have sufficient overlap enabling a specialized image registration algorithm [51, 52] to create a large-scale mosaic. There is a long-standing collaboration with the group around Köhler et al. that also includes the project of my doctoral thesis of which the EyeGuidance system is an important element.

The goal of this work was to improve the general handling of the HRT-RCM, to upgrade the capabilities of volumetric imaging with precise closed-loop focal plane positioning, and to improve large-scale mosaicking of the SNP by adding an automated, continuous focus oscillation. Instead of building a new imaging platform, the focus was on the development of a new RCM version, the Rostock Cornea Module 2.0 (RCM 2.0), with the advantage that this new RCM 2.0 can be attached to existing HRT systems. Additionally, with simple modifications, the RCM 2.0 can be used with other CLSM platforms, too. This cumulative thesis presents the development of the RCM 2.0, the combination of EyeGuidance and RCM 2.0, the attachment of the RCM 2.0 onto another imaging platform that combines multiwavelength CLSM and optical coherence tomography, the clinical usage of the RCM 2.0 with examples of various ocular

diseases, and the improvement of morphological characterization of the human corneal epithelium using the RCM 2.0. The presented results are published in peer-reviewed journals and attached at the end of this thesis.

2. Subcellular *in vivo* imaging techniques of the cornea

This chapter provides an overview of the two most relevant corneal *in vivo* imaging techniques achieving subcellular resolution, namely the CLSM and optical coherence tomography (OCT). Since this thesis is about corneal confocal microscopy, the CLSM is described in more detail.

2.1. Confocal laser scanning microscopy

The term confocal arises from the geometry of conic sections, in which two conic sections are confocal if their foci coincide [53]. Accordingly, two optical systems are confocal if they have a common focus. In a confocal microscope, the reflected signal from the illumination focal plane is focused onto the detection aperture, usually a pinhole in front of the detector, in an optically conjugate plane [54]. Due to the detection aperture, reflected light outside the illumination focus is strongly suppressed. A general setup of a confocal scanning microscope is shown in Fig. 2.1. The illumination signal from a point light source, e.g. a light source (LS) with an illumination pinhole, is collimated by a lens (CL) and imaged as a point in the specimen. In the detection path, the reflected signal is coupled out using a beam splitter (BS), focused onto the detection pinhole via a lens (FL), and detected by a detector (D). A scanning unit (XY-scanner) deflects the illumination signal into a raster of illumination spots, and the same scanning unit descans the reflected signal. The plane of the scan pupil (SP) is relayed onto the entrance pupil (EP) of the objective lens (OL) via a lens system (L1, L2). It is important to note that the relay optics influence the scan angle and the beam diameter inversely, i.e., as the scan angle increases,
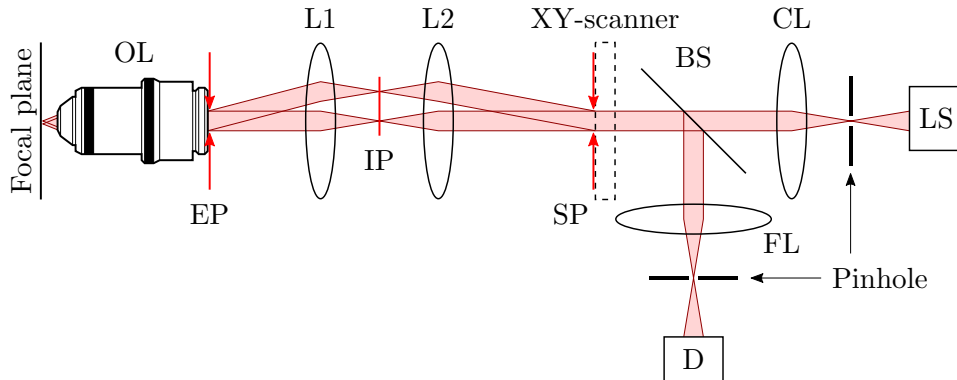
Figure 2.1.: General setup of a confocal scanning microscope. OL – objective lense, L1 and L2 – relay lenses, BS – beam splitter, CL – collimating lens, LS – light source, EP – entrance pupil, IP – intermediate image plane, SP – scan pupil, FL – focusing lens, D – detector.

the beam diameter decreases, and vice versa. The electrical signal from the detector is sequentially converted into a digital signal by an analog-to-digital converter, and the respective intensity corresponds to the gray values of the single pixels in the emerging image.

Compared to widefield microscopy, the resolution is increased by the confocal principle. Using the definition of the full width at half maximum (FWHM), lateral and axial resolution are described as follows [55]:

$$\text{FWHM}_{\text{lateral}} = \frac{0.37\lambda}{\text{NA}} \,, \tag{2.1}$$

$$\text{FWHM}_{\text{axial}} = \frac{0.64\lambda}{n - \sqrt{n^2 - \text{NA}^2}} \,, \tag{2.2}$$

where λ denotes the wavelength, NA the numerical aperture of the objective lens, and n the refractive index of the specimen. This describes the case of a perfect confocal microscope, i.e., with an infinitely small pinhole. For a finite pinhole, the equation of the axial resolution becomes

$$\text{FWHM}_{\text{axial}} = \frac{0.64\lambda}{n - \sqrt{n^2 - \text{NA}^2}} \sqrt{1 + \text{AU}^2} \,, \tag{2.3}$$

where AU refers to the pinhole size in dimensionless Airy units. One Airy unit corresponds to the diameter of the first minimum of the Airy disk.

The first confocal scanning microscope was developed and patented by Marvin Minsky [56] in 1957. A drawback of the confocal principle is the loss of signal strength, which is present in classical microscopy. After the maintenance of the brightest available light source at that time, the carbon arc proved to be too tedious, Minsky decided to use the second-brightest source, a zirconium arc. A photomultiplier was used as the detector. Instead of deflecting the light beam for scanning, Minsky chose to move the specimen's stage. To do this, a simple solenoid oscillated the stage vertically with a 60 Hz sinusoidal waveform and similarly, but much more slowly, with a sawtooth waveform in the horizontal direction.

The first laser scanning ophthalmoscope to image the retina was demonstrated by Webb et al. in 1980 [57]. An argon-krypton laser and a helium-neon laser were used as interchangeable light sources. The scanning unit consisted of a galvo mirror system, one resonantly sinusoidally oscillating at a fixed frequency of 7860 Hz horizontally and the other performing a 60 Hz vertical scan interlaced 4:1. This results in a frame rate of 15 Hz. However, since no pinhole was used for the detection, this is not a confocal laser scanning ophthalmoscope.

By adding a detection pinhole, the first confocal laser scanning ophthalmoscope was introduced by Webb et al. in 1987 [58]. In addition, a polygon scanner was used for fast vertical scanning.

In 1989, a tandem confocal scanning microscope was introduced by Cavanagh et al. that acquired *in vivo* images of the human cornea [59]. This microscope used a so-called Nipkow-disk [60] that has several pinholes arranged in a spiral pattern. Scanning is performed by rotating the Nipkow-disk. It is called tandem scanning because opposite pinholes of the Nipkow-disk are used for the scanning of the illumination path and the descanning of the detection path. A disadvantage of the Nipkow-disk is that the pinholes are only illuminated with a small portion of the illumination signal. Furthermore, if the pinholes are arranged too closely, the confocality decreases especially in the case of scattering thicker samples.

In addition to confocal point-to-point imaging, scanning slit confocal microscopy is also possible [61]. Using parallel illumination and detection along a line, i.e., using a line detector, this technique offers higher frame rates but

the confocality is given only in one spatial direction and hence the resolution anisotropic.

Another example of scanning elements are acousto-optic beam deflectors resulting in no-moving-parts confocal laser scanning microscopes [62].

As the first commercial confocal laser scanning ophthalmoscope, the HRT was available in 1990, whose successors, the HRTII and HRT3 were released in 1998 and 2005, respectively [16]. The addition of the RCM shifts the focal plane from the retina to the cornea, resulting in a corneal confocal laser scanning microscope [17]. The HRT uses a linearly polarized laser diode at 670 nm as a light source. With respect to Fig. 2.1, a polarizing beam splitter (PBS) is used that the linearly polarized laser light passes in the illumination path. An additional quarter-wave plate (QWP) as the last optical element in the illumination path of the HRT rotates the polarization of the reflected signal in total by 90°, causing this signal to be coupled out by the PBS for detection. Due to this combination of PBS and QWP, more signal is available for detection. An avalanche photodiode is used for detection. The scanning unit consists of a resonant mirror scanner for the fast horizontal direction and a galvanometric mirror scanner for the slow vertical direction. The RCM uses a water immersion objective (Achroplan 63x/0.95 W optimized for 670 nm; Zeiss, Jena, Germany), and the cornea is optically coupled using a sterile PMMA cap (TomoCap) and aqueous tear substitute gel. In addition, the HRT has an internal focus scan that captures image stacks of 80 µm in approximately 2 µm increments with the RCM [16]. In total, the HRT-RCM produces 8 bit grayscale images consisting of 384×384 pixels. The FOV is 400 µm $\times$ 400 µm, the lateral resolution is 1 µm and the axial resolution is 4 µm [63] [16].

2.2. Current trends in confocal laser scanning microscopy

As in previously mentioned studies, CLSM is generally used to obtain two-dimensional (2D) *en face* images. The slit lamp, however, offers the possibility to directly visualize optical sections of the cornea orthogonal to the surface. To create such cross-sections with the HRT-RCM, single *en face* images from

different depths with sufficiently small axial distance have to be acquired first. Then, this obtained image stack must be aligned by image registration procedures to remove motion artifacts. This results in volumes from which cross-sections can finally be generated. However, the HRT-RCM is limited in its ability to generate such image stacks and thus in its three-dimensional (3D) imaging, since the internal focus drive only provides a $80\,\mu m$ shift [64].

In corneal *in vivo* CLSM, the scanning speed plays a major role, since the negative influence of eye movements decreases with an increased frame rate. As mentioned above, motion artifacts can be eliminated by image registration, but the registration also benefits from a higher frame rate. This is because the lateral distance between two successive images is smaller and thus their overlap is larger. Therefore, more information is available for image registration. At the same time, a larger overlap of all images to each other in the stack also leads to a laterally larger cohesive volume. Thus, research regarding CLSM for 3D imaging often goes in the direction of accelerating the scan speed in the axial direction or avoiding a scan entirely by other techniques. For instance, it is shown in [65] how to accelerate the axial scan speed with an acoustic liquid lens. Furthermore, a technique called volumetric Lissajous confocal microscopy is presented. Here, the frequency of the acoustic liquid lens is adapted to the lateral scan mirrors in such a way that the laser focus of the confocal microscope follows a dynamic Lissajous trajectory. In conventional CLSM, the axial scan is the slowest one and volumes are created with axially consecutive *en face* images. In the volumetric Lissajous confocal microscopy, the axial scan is the fastest one and at the same time it takes the conventional CLSM to acquire one *en face* image, 3D structural information is obtained immediately. The spatial resolution of the resulting volume enhances with the accumulation of multiple scans. With the immediate availability of 3D information, scan parameters do not need to be determined before the acquisition, and the spatiotemporal resolution can be selected during or after the measurement. In addition, it was shown in [65] how to increase the temporal resolution with a few scans and an inpainting algorithm. This is a promising technology, but one that places high demands on hardware and software. Especially for samples with strong spontaneous motion, like the *in vivo* examination of the cornea, the

13

requirements increase. Due to the movement, 3D information from the same region of the sample is not always available. This means that additional scans may be necessary to obtain sufficient resolution and the speed advantage is lost.

As an example, how to completely avoid axial scanning and acquire information from all depths simultaneously to increase volumetric scanning speed, is shown in [66], where a microscope technique is described that provides confocal, multiplane imaging. To achieve this, the so-called Multi-Z confocal microscopy utilizes a high and low NA for the detection and illumination path, respectively. The high-NA detection leads to high signal collection efficiency and the low-NA illumination to an axially extended focus. To take advantage of this extended focus, multiple, axially distributed detectors with reflective pinholes acquire signals simultaneously from different depths. The reflective pinholes ensure that light that is rejected by one pinhole is sent on to the next pinhole. This process is repeated until the last detector, resulting in high signal efficiency. With the setup in [66], which consists of four detectors, volumetric imaging produces extended depth-of-field images. This Multi-Z confocal microscopy scales well, but in order to use it to generate corneal volumes where all cellular layers are resolved in the cross-sectional image, the number of detectors would have to be increased considerably. Consequently, the setup would become more complicated and expensive.

Another way to increase the speed of volumetric imaging in CLSM is to combine intentional longitudinal chromatic aberration with a broadband light source. The chromatic aberration is intentionally induced to focus the light of the broadband spectrum to different depths depending on the wavelength, thus creating spectrally encoded depth information. To induce the desired chromatic aberration, dedicated lenses or lens arrays are utilized whose design and materials result in sufficient dispersion for the relevant wavelength range. Finally, the technique used to decode the spectrally encoded depth information depends on the selected light source.

For example, in [67], a photonic crystal fiber is illuminated with a Ti:Sapphire femtosecond laser to generate a supercontinuum that provides a broadband light source of 590 nm to 775 nm. A series of plastic aspherical lenses are used

to induce chromatic aberration, and the reflected signal is captured with a spectrometer. As a result, this setup demonstrates volumetric imaging of a non-transparent biological tissue by chromatic CLSM for the first time [67].

Another example is the setup in [68, 69], where a single plano-convex lens made of N-SF11 induced the desired chromatic, and a mode-locked femtosecond laser with a spectral range of 1.48 µm to 1.56 µm is directly used as the light source. Although it offers great stability and high spatial coherence, it also has a considerable non-smoothness of the spectrum. To eliminate the spectral non-smoothness, a novel differential confocal setup is shown in [68]. This setup splits the reflected signal into two optical paths with different confocal settings, where two identical detectors are located at a focus and defocus position, respectively. These detectors consist of two single-mode optical fibers of the same type that direct the two signals to a spectrum analyzer. From the intensity ratio of the two confocal signals, an axial response is obtained. Now, the depth information is derived from the peak wavelength of this axial response. In [69], an additional axial response is obtained from the inverse of the intensity ratio. Thus, both the main-lobe and side-lobes of the axial responses can be used to obtain a seamless relationship between peak wavelength and depth information. In doing so, the depth range is increased by a factor of four without changing the optical setup. At this point, it should be mentioned that this method is intended for 3D surface profiling. In this form, the volumetric imaging of transparent biological tissues, such as the cornea, is not possible. Whether it is possible with modifications requires further investigation.

An additional example of a chromatic confocal microscope is shown in [70], where it does not require a spectrometer, since it uses a swept-source laser as the light source, which emits narrow linewidth laser light in a wide wavelength range of 770 nm to 820 nm at a maximum sweep frequency of 200 Hz. This provides a method to temporally decode the spectrally encoded depth information by a single photodetector. For this microscope, a set of acrylic lenses was used to ensure that its so-called chromatic probe achieves a large chromatic aberration. For comparison with a conventional chromatic confocal microscope, this setup was also operated using a broadband source and a spectrometer. Here, the two systems were examined in terms of acquisition times, i.e., different integration

times of the spectrometer versus corresponding sweep frequencies of the swept-source laser. Since the swept-source laser has a narrow linewidth for higher intensities compared to the broadband source, the swept-source-based setup provided considerably more accurate results and highly stable behavior for the lowest acquisition times than the conventional setup.

2.3. Optical coherence tomography

Another rapidly spreading technology, which was originally first applied *in vivo* to the posterior [71] and anterior [72] segment of the eye, is OCT. In the years that followed, it was applied in other fields besides ophthalmology, such as dermatology [73].

In principle, OCT is a low-coherence interferometry technique [74]. The signal from a broadband light source, e.g. a superluminescent diode, or a spectrally scanning source, e.g. a frequency swept laser source, is split between a reference and sample arm using a beam splitter. The back reflected light from the sample and the reference mirror in the sample arm are combined by a beam splitter. Interference between the two beams only occurs if the optical path lengths of the reference and sample arms are equal within the short coherence length, which is in the order of micrometers.

Fig. 2.1 shows the similarities and differences of various OCT implementations. The first implementation of the OCT is the time-domain OCT (TD-OCT) [75]. Here, the reference arm length is modulated for a depth scan. Therefore, the reference mirror is scanned axially for each sample point, resulting in intensity modulations, so-called interference fringe bursts, which are recorded by the detector. From the envelope of this signal, the amount of backscattered light can be derived directly. Thus, a reflection depth profile of the sample is obtained at the beam position, also called amplitude scan (A-scan) in reference to ultrasound imaging. A 2D depth profile (B-scan) is obtained if the beam or the sample is additionally scanned along a lateral direction. With the addition of the second lateral direction, volumes can be generated from multiple B-scans.

The successor over TD-OCT is Fourier domain OCT (FD-OCT), where mechanical scanning of the optical path length is not required and an interference
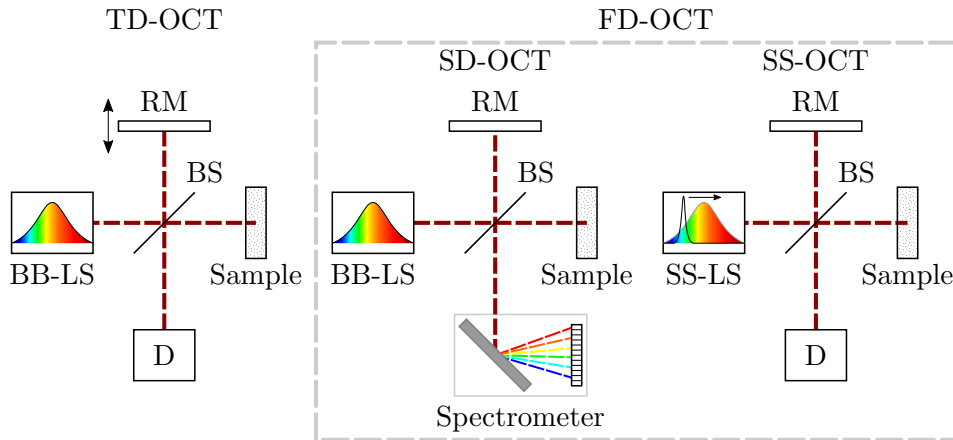
Figure 2.2.: Schematic of time-domain (TD), spectral domain (SD), and swept-source (SS) OCT. RM – reference mirror, BS – beam splitter, BB-LS - broadband light source, SS-LS – frequency swept laser source, D – detector.

spectrum, also called spectral interferogram, is recorded instead. This interferogram consists of the superposition of the spectrum of the light source and several interference fringe patterns, which are created by the backscattered light of corresponding structures in the sample. The modulation frequency is inversely proportional to the corresponding structure depth and the modulation amplitude is proportional to the square root of the reflectance [74]. From this spectral interferogram, the A-scan is calculated by the Fourier transform of the interferogram. Two techniques have been established for FD-OCT, spectral domain OCT (SD-OCT) [76] and swept-source OCT (SS-OCT) [77]. As shown in Fig. 2.2, SD-OCT uses a spectrometer to record the spectral interferogram. SS-OCT, in contrast, uses a sweeping light source that rapidly sweeps a spectral filter in the laser resonator to change the lasing wavelength. Synchronously, the spectral components of the backscattered light are recorded with a fast detector, resulting in the aforementioned spectral interferogram. The advantage over TD-OCT is that now all depth information of the sample is available in this spectral interferogram, simultaneously in the case of SD-OCT or after one frequency sweep in the case of SS-OCT. This results in a dramatic increase in imaging speed, as compared to the mechanical movement of a mirror, the acquisition of a spectrum by a camera or the frequency sweep of a swept-source

laser is drastically faster. Here, SS-OCT is the fastest method. For example, swept-source lasers in the MHz range have already been used for retinal imaging [78].

Since OCT is an interferometric technique, its axial resolution does not depend on the optics used but on the coherence length of the light source [74]:

$$\delta z = l_c = \frac{2 \ln (2)}{\pi} \cdot \frac{\lambda_0{}^2}{\Delta \lambda_{\text{FWHM}}} \,. \tag{2.4}$$

Here δz describes the axial resolution, l_c the coherence length, λ_0 the central wavelength, and $\Delta \lambda_{\text{FWHM}}$ the wavelength range. The lateral resolution, in contrast, depends on the optical elements and is again calculated according to Eq. (2.1).

With OCT, it is important to note that the total depth that can be imaged is determined by the focal depth. In order to increase the depth of focus, the utilized NA of the objective lens must be decreased and vice versa. Thus, a suitable compromise between the imaging depth and lateral resolution must be selected for the specific application.

Although the main application of OCT is retinal imaging, several OCT methods for corneal imaging have been researched in recent years. These include, for instance, SD-OCT [79], ultrahigh resolution SD-OCT [80, 81], Garbor-domain OCT [82], full-field OCT [83–86], curved-field OCT [87], and polarization sensitive micrometer OCT [88].

Most of these OCT methods are applied in non-contact mode. On the one hand, this has advantages in terms of subject compliance, on the other hand, it increases the influence of eye movements, which results in a higher demand for fast sampling rate or post-processing. In addition, the refractive index difference between the cornea and the air makes it difficult or impossible to image the uppermost layers due to strong back reflections. One advantage of CLSM over OCT is that the lateral resolution is independent of the imaging depth of a volume. For the smallest cell structures, such as in the epithelium, the lateral resolution is important for both en face images and cross-sections. Which technology should ultimately be preferred is thus dependent on several factors. For example, if only *en face* images are needed, CLSM should be used, as this is

possible with a lower budget due to lower laser source requirements. For cross-sections, where the lateral resolution is not crucial, but the axial resolution, e.g., for thickness measurements, OCT should be preferred. Ultimately, both technologies could be combined and support each other.

3. Materials and methods

This chapter provides an overview of the methods and materials used in the peer-reviewed publications published as part of this thesis.

3.1. Rostock Cornea Module 2.0

Fig. 3.1 shows the original RCM and two iterations of the self-developed RCM 2.0. Every *in vivo* examination of the cornea by each RCM version requires the use of a topical anesthetic (e.g. Proparakain-POS; Ursapharm, Saarbrücken, Germany). In addition, a carbomer gel (e.g. Vidisic; Bausch & Lomb/Dr. Mann Pharma, Berlin, Germany) is applied as a tear substitute and immersion medium between cornea and TomoCap, which is a sterile single-use contact cap, as well as between TomoCap and objective lens. The original RCM uses a diverging lens and a water immersion objective lens (Achroplan 63x/0.95 W; Zeiss, Jena, Germany) to shift the focal plane from the retina into the cornea. Different diverging lenses can be used to change the FOV. By default, a FOV of $400\,\mu m \times 400\,\mu m$ is used. To change the focal plane, the TomoCap and thus the cornea is moved axially by hand via a mechanical drive. This is disadvantageous because the contact pressure from the TomoCap to the cornea changes while the focus is shifted. Depending on the direction of change, this can either lead to loss of contact or increase the pressure so much that compression artifacts appear in the form of folds at the level of Bowman's layer. These folds are called Kobayashi structures (K-structures) [89] and form a characteristic pattern over the entire cornea, the so-called anterior corneal mosaic (ACM) [90]. These K-structures are a particular problem for imaging thin layers such as the SNP because the folds result in interrupted imaging of the nerve fibers once the deformation height exceeds the depth of field, as is

HRT + Rostock Cornea Module

HRT + Rostock Cornea Module 2.0
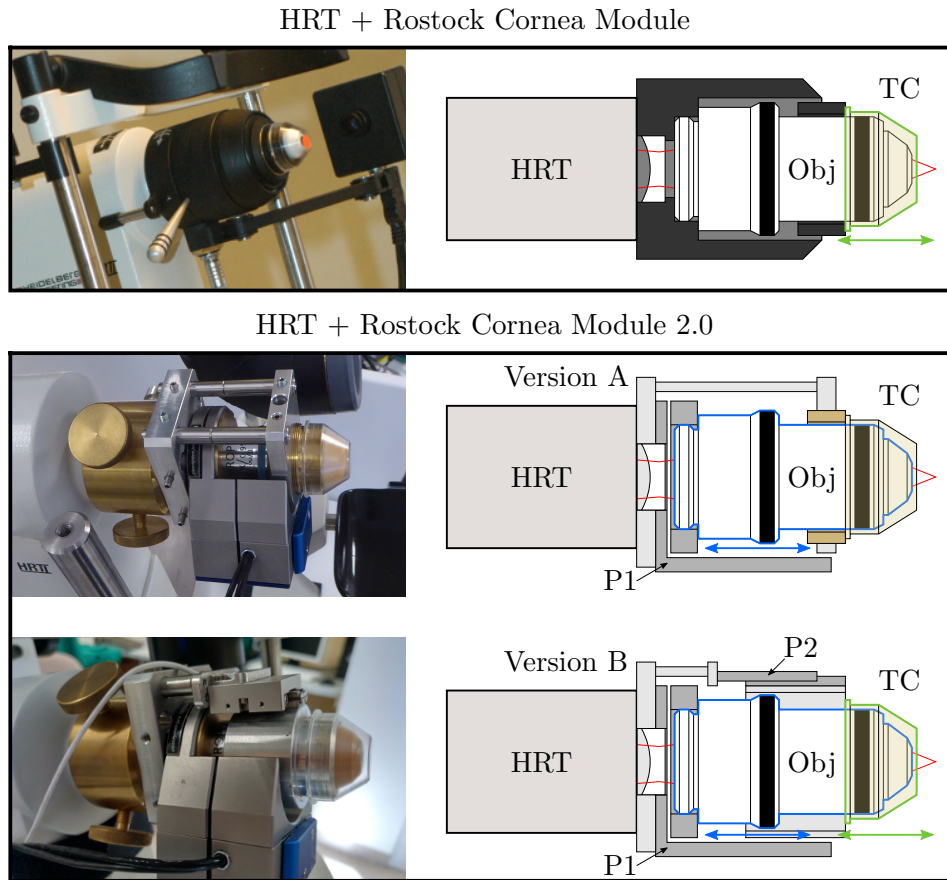
Figure 3.1.: Photographs (left) and sketches (right) of the original RCM (top) and the initial version A and revised version B of RCM 2.0 (bottom). TC – TomoCap, Obj – objective lens, P1 – first piezo actuator, P2 – second piezo actuator.

exemplarily shown in Fig. 3.2.

This drawback is addressed by the RCM 2.0. Here, the focal plane is changed mainly by the axial translation of the objective lens instead of the TomoCap. For this purpose, a piezo actuator (MIPOS 600 SG OEM; piezosystem jena GmbH, Jena, Germany) is used, which offers a travel range of $500\,\mu m$ in closed-loop operation and $600\,\mu m$ in open-loop operation. This piezo actuator is controlled and monitored by a self-written LabVIEW program. The focal plane is then controlled either by program input or by a joystick. In addition, the focus can be driven in different scan functions, e.g. sine, triangle, or rectangle. Almost all

mechanical adapter parts were self-designed during the curse of this dissertation and manufactured by the mechanical workshop of the Institute of Physics of the University of Rostock. Exceptions are the mounting rods, which belong to an optical cage system (Thorlabs GmbH, Bergkirchen, Lübeck, Germany, Newton, NJ, USA). Furthermore, some adapter parts were designed to be compatible with this cage system, which enables more simplified modularity to other instruments.

In the initial version of the RCM 2.0, see Fig. 3.1 version A, the TomoCap is moved axially to the desired position by hand via a thread and then locked in place prior to an examination. This determines the initial position of the focal plane. If a corneal layer of interest is outside the travel range of the objective lens, the examination must be aborted and the TomoCap position readjusted. This is especially critical while imaging volumes, as an improperly adjusted initial focus will reduce the axial extent of the volume. Since the readjustment of the TomoCap unnecessarily prolongs the overall examination time, an additional piezo actuator (SLC-1720-020-W-L; SmarAct GmbH, Oldenburg, Germany) was introduced in the revised version of the RCM 2.0, see Fig. 3.1 version B, to control the axial position of the TomoCap. This piezo actuator has a 12 mm travel range with a submicron resolution and is used to adjust the initial focal plane while in contact with the eye. This way, the second piezo actuator provides a precise, quick, and convenient adjustment of the focal plane that is possible during an examination, too. Additionally, this actuator allows the possibility of creating compound depth stacks with extended depth. Overall, the piezo actuators of the RCM 2.0 result in more precise, faster, more convenient, and more versatile control over the focal plane.

In the published manuscripts [P1–P4], the initial version of the RCM 2.0 was used. In [P3, P4], the modularity of RCM 2.0 was utilized to allow its adaptation to the SPECTRALIS platform (Heidelberg Engineering GmbH, Heidelberg, Germany). In [P5, P6] the revised version of the RCM 2.0 was applied. *In vivo* examinations with the RCM 2.0 were performed on human corneae in all publications. In addition, *ex vivo* examinations were performed on enucleated porcine eyes at [P4, P5] and lamb eyes at [P4].

In addition to improving the RCM, an alternative TomoCap was developed to
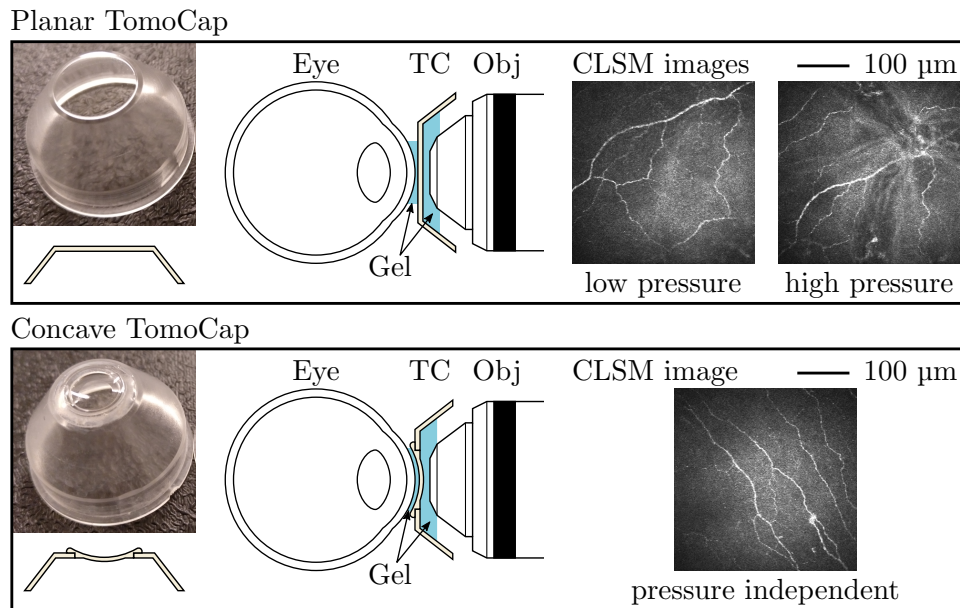
Planar TomoCap

Concave TomoCap

Figure 3.2.: The planar and concave TomoCap in comparison. SNP images with the planar TomoCap show K-structures at high contact pressure. No K-structures are formed with the concave TomoCap, regardless of the pressure. TC – TomoCap, Obj – objective lens.

attenuate involuntary eye movements and simultaneously avoiding the formation of K-structures. Attenuated eye movements result in fewer motion artifacts, and thus, subsequent images of an axial scan have a larger lateral area in common. With the standard TomoCap, eye movements can be attenuated with a higher contact pressure on the cornea, but this also creates the K-structures that impede the imaging of continuous nerve fibers in the SNP. To address these issues, a concave contact cap with a radius of curvature equal to the average human cornea (7.8 mm) was developed.

Fig. 3.2 shows a comparison of the planar standard and the concave TomoCap as well as images of the SNP created with corresponding caps and contact pressures, showing K-structures where applicable. The concave contact surface ensures that the cornea does not deform, regardless of the contact pressure, and thus no K-structures are formed. Additionally, the concave contact surface in combination with the immersion gel and its viscosity creates a suction effect that attenuates eye movements. This is explained in more detail and quantified in

[P1]. Although the concave TomoCap is preferred for the acquisition of volume stacks or single images, the planar TomoCap is still preferred for laterally large-area mosaics, since otherwise the required guided eye movements would be restricted.

3.2. Image processing

Since eye movements introduce non-affine distortions in CLSM images, image registration with only affine transformation is insufficient to remove motion artifacts induced by unavoidable eye movements. Therefore, an elastic image registration by Allgeier et. al that is tailored to the scanning system of the HRT is used in post-processing [51, 52].

As the cornea translates maximally 1 µm in the acquisition time of a single image row of 65 µs, influences of eye movement in this time scale are neglected, and an image row is assumed to be undistorted. The algorithm divides the single images into subimages or slices consisting of a constant number of pixel lines. For each subimage, a displacement vector to the preceding image is calculated using a phase correlation function. These displacement vectors are then used to estimate the trajectory of the eye movement. Subsequently, from this trajectory, offset vectors are interpolated for all single image rows. As a result, the single image rows are then merged to images with strongly reduced motion artifacts.

To visualize the effect of elastic registration, three consecutive stromal images of a depth scan before and after registration are shown in Fig. 3.3. Each image has been respectively colored in a yellow, magenta, and cyan tone. If these colored images are now superimposed to form a composite image, associated structures that have the same position in all three images would appear in a gray tone. If they overlap only in two images, the result is a corresponding mixed tone. In the example in Fig. 3.3, the composite of the unregistered images shows the keratocyte nuclei shift due to eye movements within the acquisition of these three images. In the upper region of the composite, the reddish tone of the structures shows that the movement does not begin until below this region in the second current image. This becomes even more apparent with the
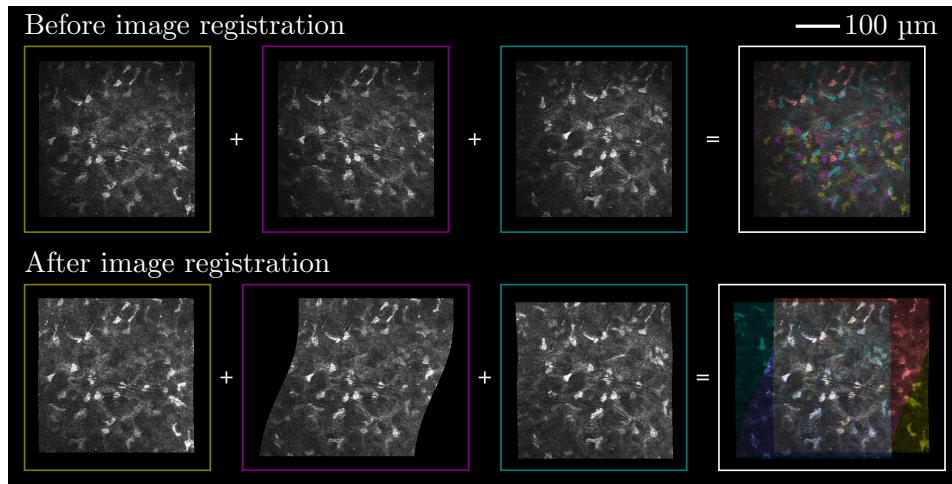
Figure 3.3.: Visualization of elastic image registration in three successive stromal images of a depth scan. Composite images were generated from colored images for the unregistered and registered cases.

registered images. The second image shows a deformation that corresponds to eye movement. In the registered composite, the success of elastic registration is evident.

Besides reducing motion artifacts, elastic registration is used to create large-area mosaics consisting of single images by guided eye movements.

To assemble individual images of a depth scan into a volume, the subsequent images are assembled after registration using software such as ImageJ [91]. The axial spacing of the individual images depends on the focus scanning speed and the frame rate, which is 30 fps in the case of the HRT. For sufficiently small scan speeds, the axial shift of individual pixels within an image can be neglected. For most of the depth scans in the work shown here, this is the case since the axial distances for volume generation are usually 1 µm or less. Finally, sectional images in arbitrary spatial directions can be created from the generated volumes.

4. Results

In this chapter, the results of the publications are briefly summarized. It follows the chronological order of the publications, starting with the introduction and presentation of the initial version of the RCM 2.0 and a prototype of the concave TomoCap. Afterwards, it continues with the application of the RCM 2.0 in large-area imaging of the SNP. Then, the adaptation of the RCM 2.0 with a different imaging platform, where the combination with OCT occurred and corneal CLSM was performed with different wavelengths, is presented. Finally, the introduction of the revised version of the RCM 2.0 is done, testing the clinical relevance of CLSM imaging in different pathologies and its applicability for morphological characterization of the epithelium.

4.1. Cellular *in vivo* 3D imaging of the cornea by confocal laser scanning microscopy

Sebastian Bohn, Karsten Sperlich, Stephan Allgeier, Andreas Bartschat, Rubi Prakasam, Klaus-Martin Reichert, Heinrich Stolz, Rudolf F. Guthoff, Ralf Mikut, Bernd Köhler, and Oliver Stachs

The goal of this publication was to provide a solution to the problems of the original RCM in corneal *in vivo* CLSM as described in Sec. 3.1. This work introduces the initial version of the RCM 2.0 and a prototype of the concave TomoCap, demonstrating the solution approach already described in Sec. 3.1. To assemble the concave TomoCap, the anterior concave part of a three-mirror gonioscopy lens was cut off, the resulting cut surface polished, and glued to a standard TomoCap after its contact surface was removed.

In vivo corneal image stacks were acquired on which the elastic image registration algorithm, described in Sec. 3.2, was first compared with a rigid one. Here it was clearly shown that the elastic registration was superior to the rigid one since also non-affine motion artifacts could be addressed, see Fig. 5 of [P1].

To quantify the constraint of each cap design, the two parameters mean lateral image-to-image shift value and mean approximate overlapping area were introduced and calculated based on the centers of gravity of the elastically registered images. Therefore, several image stacks were recorded from three healthy subjects with the planar and concave contact caps. Details can be found in Sec. 2.3 of [P1].

Overall, a 70 % to 80 % eye movement reduction was found within the images of the subjects using the concave instead of the planar contact cap. Concerning the approximate overlapping area, the loss to the perfect image stack without eye movement was considered. Here it could be shown that depending on the stack depth and the test person, the loss of the overlapping area was reduced by 74 % to 80 % using the concave contact cap in comparison to the planar one.

In addition, cross-sections in several directions (Figs. 6 and 9 in [P1]) and various 3D representations (Figs. 8 and 10 in [P1]) were generated from the acquired corneal image stacks, including a 396 µm deep cuboid with a 266 µm × 268 µm lateral extent. The corneal cross-sections produced were of such high quality that the different cellular layers and structures were well observable.

4.2. 3D confocal laser-scanning microscopy for large-area imaging of the corneal subbasal nerve plexus

Stephan Allgeier, Andreas Bartschat, **Sebastian Bohn**, Klaus-Martin Reichert, Karsten Sperlich, Marcus Walckling, Ralf Mikut, Veit Hagenmeyer, Oliver Stachs, and Bernd Köhler

For large-scale imaging of the SNP using CLSM, several images from different regions are stitched together to create a mosaic. An established system for this is the EyeGuidance system that guides the nonexamined eye along an expanding spiral path resulting in the examined eye also following this path. In this way, images of a larger area are continuously obtained for a mosaic generation. With the limited depth of field, this system is highly sensitive to small deviations of the focal plane from the SNP layer. These deviations are already caused by slight eye movements perpendicular to the focal plane, by the curvature of the cornea especially at the outer area, and by deformation of the cornea due to excessive contact pressure, see K-structures and ACM in Sec. 3.1. Therefore, this work evaluates the combination of the EyeGuidance system and the RCM 2.0 utilizing an oscillating focal plane in a feasibility study.

Three dedicated computers that respectively control the image acquisition via the HRT, the guided eye movement via the EyeGuidance system, and the oscillating focal plane via the RCM 2.0 communicate over a TCP/IP network to allow a synchronized start of all systems. A triangular function with a peak-to-peak amplitude of 40 µm was chosen for the oscillating focal plane, see Fig. 3 in [P2]. While the initial focus lies in the SNP, the oscillation provides images of the surrounding epithelium and stroma. If the SNP moves out of the initial focus during the examination, the oscillation ensures that the data set still contains SNP images.

For evaluation, different parameters specifying the oscillating focal plane and the spiral motion of the guided eye movement were tested. These parameters included the velocity, amplitude, and period of the focus oscillation, and the

fixation target velocity. Here, the emphasis was on the focus oscillation velocity. The lateral spiral motion of the fixation target was adjusted to the focus oscillation velocity in each case so that after one period the CLSM images were approximately 200 µm laterally separated from each other. Mosaics were acquired from nine subjects at four different focus oscillation velocities of 60.6 µm/s, 121.2 µm/s, 181.8 µm/s, and 242.4 µm/s, with an acquisition time of 40 s.

Three different approaches were used and compared to montage the mosaics from the elastically registered 3D image sets, see Fig. 5 in [P2]. The first approach used all images, resulting in mosaics that show superimpositions of all tissue layers. Nerve fibers are visible only with low contrast compared to single SNP images. The second approach uses only images acquired at the initial axial position of the focus oscillation to generate the mosaic. This corresponds to the 2D EyeGuidance process with a constant focal plane [49]. The results in [P2] show that using this method, the proportion with optimally focused SNP was shown to vary widely among the mosaics. Some contained even more epithelium or stroma than SNP structures while others contained almost only SNP. The third approach uses a dedicated tissue classification algorithm [92] to exclude images without SNP structures. This results in mosaics that consist almost entirely of SNP tissue.

Regarding the oscillation parameters, it was found that with increased focus oscillation velocity and correspondingly increased speed of the spiral motion, the expansion rate of the mosaics also increases. With the tissue classification, the average expansion rates were found to be $0.031\,\mathrm{mm^2/s}$, $0.059\,\mathrm{mm^2/s}$, $0.081\,\mathrm{mm^2/s}$, and $0.111\,\mathrm{mm^2/s}$, respectively. In terms of reliability to acquire images promising a successful SNP mosaic, differences only became apparent using the highest velocity. Here, the examinations had to be repeated for two of the nine test subjects, as the live stream of the single images did not indicate good data sets. In the case of the first subject, a second examination was sufficient. For the second one, the examination was stopped after three unsuccessful attempts. An additional data set could not be used due to insufficient image quality. Here, however, the reason was an inhomogeneity of the contact gel, which was not noticed during the examination. Furthermore, it is not possible

to establish a correlation between oscillation velocity and reliability due to the low number of test subjects. Systematic differences in mosaic image quality were not found between the oscillation speeds.

4.3. *In vivo* corneal confocal microscopy aided by optical coherence tomography

Sebastian Bohn, Karsten Sperlich, Heinrich Stolz, Rudolf F. Guthoff, and Oliver Stachs

In vivo corneal CLSM is often compromised by the lack of information regarding the position and orientation of the imaging plane during the examination. To solve this issue, the modularity of the RCM 2.0 was exploited in this publication to attach it to the SPECTRALIS OCT2 platform (Heidelberg Engineering GmbH, Heidelberg, Germany). This a retinal imaging system that combines OCT with a confocal laser scanning ophthalmoscope for *en face* imaging and eye-tracking purposes. With the attachment of the RCM 2.0, a CLSM system has was created that provides simultaneous information on position and orientation during the examination by OCT. This section briefly explains the necessary modification, results, and additional information gained from this multimodality.

The optical elements of the RMC 2.0 change the optical path of the measuring arm. Therefore, the length of the reference arm must be adjusted accordingly. *En face* images using CLSM are generated at 815 nm and OCT B-scans at 880 nm with a FWHM bandwidth of 80 nm. It should be noted that all *en face* CLSM images show a central back reflection, as the objective lens of the RCM 2.0 does not have an optimal anti-reflective coating.

Several examples of simultaneously acquired in vivo corneal *en face* and B-scan images were successfully obtained. The B-Scans reveal a number of distinct interfaces or planes can be seen in the B-scans, see Fig. 3 and 4 of [P3]. Due to the strong focusing by the RCM 2.0 objective lens, the focal plane of the

CLSM modality shows up as the line with the strongest intensity in the B-scan if it is inside the cornea. Because of the weak reflectivity of the immersion gel, it can even be seen outside the cornea. Furthermore, the anterior and posterior corneal surface, as well as the contact surface of the TomoCap, can be seen, even if they are not in close vicinity of the CLSM focal plane. With all these lines, information about the position and orientation of the CLSM focal plane was deduced. This multimodality may also be used during the alignment process to ensure that the *en face* CLSM image is parallel to the corneal surface, even before the contact cap touches the cornea. This shortens the examination time and makes the entire procedure more comfortable for the subjects or patients and thus increasing compliance. In the B-scan, the full corneal thickness can be measured directly. For the thickness of corneal substructures, an oblique section and information from both modalities are used, being the angle between the corneal surface and the CLSM focal plane from the B-scan and the projected length of the corresponding structure in the CLSM image. In Fig. 5 of [P3], the layer thicknesses of the epithelium and Bowman's layer were calculated exemplarily. The example thicknesses measured in the manuscript agree well with values from the literature and other methods.

4.4. Multiwavelength confocal laser scanning microscopy of the cornea

Sebastian Bohn, Karsten Sperlich, Thomas Stahnke, Melanie Schünemann, Heinrich Stolz, Rudolf F. Guthoff, and Oliver Stachs

Besides OCT, the SPECTRALIS is equipped with three different wavelengths for the scanning laser ophthalmoscope. This allows imaging of retinal layers in different depths at 488 nm, 518 nm, and 815 nm. In addition, this allows various fluorescence imaging modes, e.g., autofluorescence and fluorescein angiography.

Here, these wavelengths were used to investigate whether, in addition to depth-dependent scattering losses, other wavelength-dependent differences occur in confocal reflectance microscopy of corneal layers.

For this purpose, the combination of RCM 2.0 and SPECTRALIS was used to perform CLSM imaging *in vivo* on a human cornea and *ex vivo* on lamb and porcine corneae. Images were compared between wavelengths with regard to image quality and differences in the depicted structures. For human corneas, images of the epithelium, SNP, stroma, and endothelium were acquired, see Figs. 3–7 of [P4]. Images of the lamb and porcine corneae were acquired at the blue and near-infrared wavelengths of the epithelium, stroma, and endothelium, see Figs. 9–10 of [P4]. As in the previous manuscript, all *en face* CLSM images show a central back reflection since the anti-reflective coating the RCM 2.0 objective lens is not optimized for the three wavelengths.

In the human cornea, the effect of wavelength- and depth-dependent scattering losses in the form of a diffuse background are most apparent in the SNP and Stroma. Nevertheless, nerve fibers and keratocyte nuclei are visible without limitations for all wavelengths. Since the epithelium is the topmost corneal layer, no scattering losses are apparent there. Structural differences depending on the wavelength are shown in the superficial epithelial cells and the endothelium. In the first, cell borders, nuclei, and cytoplasm are more prominent at 488 nm and 518 nm than at 815 nm. In contrast, in the near-infrared, cell borders and cytoplasm have a more uniform, homogeneous reflectance. The cellular structure of the endothelium in the human cornea is clear at short wavelengths and is difficult or impossible to detect in the near-infrared. Additionally, some nuclei are visible as bright spots at 488 nm.

Compared to the human cornea, the animal corneae show differences in wavelength-dependent appearances of the cellular structures. The cell nuclei and cytoplasm of the superficial epithelial cells in the lamb cornea reflect more strongly and the latter with a somewhat different structure at 815 nm than at 488 nm. In the porcine cornea, the cell nuclei and cytoplasm reflect similarly at both wavelengths, but the cytoplasm also reflects in the near-infrared with a somewhat different structure. The stromal keratocyte nuclei are difficult to depict at the short wavelength in the animal corneae, but this may be also related to the advanced time after the enucleation of the eyes. In the endothelium of the animal corneae, the cellular structures are visible at both short and long wavelengths. While no nuclei are visible in the lamb cornea at

488 nm, some are visible as bright spots in the porcine cornea. At 815 nm, they appear darkened in the lamb and porcine corneae.

4.5. *In vivo* Histology of the Cornea – from the "Rostock Cornea Module" to the "Rostock Electronic Slit Lamp" – a Clinical "Proof of Concept" Study

Sebastian Bohn, Thomas Stahnke, Karsten Sperlich, Stephan J. Linke, Sanaz Farrokhi, Maren Klemm, Stephan Allgeier, Bernd Köhler, Klaus-Martin Reichert, Martin Witt, Oliver Stachs, and Rudolf F. Guthoff

With the initial version of the RCM 2.0, there was still the problem of the cumbersome initial focal plane adjustment via the TomoCap by hand. This often led to an unclear starting position of the focal plane and the entire travel range of the RCM 2.0 objective lens could not be fully utilized. To approach this problem, the revised version of the RCM 2.0 with the piezo actuator moving the TomoCap was introduced and used in this and the following work. This should improve clinical usage by giving more control over the initial focus position before and during the measurement, as well as the ability to generate image stacks larger than 500 µm axially. In addition, an improved version of the concave TomoCap is presented, which has a smaller diameter of 10 mm, simplifying the coupling procedure.

The revised version of the RCM 2.0 was first successfully tested on an enucleated porcine bulb. The entire corneal thickness of more than 900 µm could be assembled from multiple image stacks, see Fig. 2 of [P5]. A sagittal cross-section is generated from the reconstructed 3D volume and shown with specific *en face* images of different layers. Subsequently, the imaging was tested on healthy volunteers and selected patients with corneal diseases. In each case, cross-sectional images were again generated from volume data and corresponding

en face images were shown. Due to the concave cap, it was possible to generate corneal cross-sectional images in their full thickness and high quality.

In Fig. 5 of [P5] the case of a keratoconus patient eight months after cross-linking treatment is shown. While a normal epithelium and endothelium is observed, the rest of the cornea differs from a healthy one. The SNP is highly rarefied, a highly reflective network is adjacent to Bowman's layer, and various changes are seen throughout the stroma. Opacified zones of hyperreflective cytoplasm of keratocytes are found in the anterior stroma. Slightly deeper, keratocytes with low contrast and no distinguishable nuclei are visible. In the middle stroma, highly reflective keratocyte nuclei with needle-shaped structures are visible. Following in the posterior stroma the keratocytes are low reflecting without visible nuclear structure.

Fig. 7 of [P5] shows a case of recurrent keratitis in which opacities in the anterior cornea are already visible in the slit lamp and OCT images. In the CLSM images in Fig. 8 of [P5], these opacities show up as a dense network of keratocyte structures with extremely highly reflective cytoplasm. Furthermore, massive infiltrates with dendritic cells, which are antigen-presenting cells, are found in the epithelial basal cells and also appear in Bowman's layer. In the deeper stroma, cell nuclei can no longer be demarcated. In addition, a 3D reconstruction from Bowman's layer to the highly reflective stroma is also shown for this case.

As a final case, the cornea of a patient one month after photorefractive keratectomy is shown in Fig. 9 of [P5]. As expected, no subbasal nerve structures and no equivalent to Bowman's layer are shown. Strongly reflective round structures are visible at the transition to the stroma. The anterior stroma is characterized by highly branched and highly reflective keratocytes, decreasing with increasing depth until the stroma appears normal in the deepest layers.

This work demonstrated that the revised version of RCM 2.0 produced not only 2D images but 3D volumes of various pathologies of such high quality that sectional images with cellular resolution were generated in slit lamp geometry.

4.6. Morphological characterization of the human corneal epithelium by *in vivo* confocal laser scanning microscopy

Katharina A. Sterenczak, Karsten Winter, Karsten Sperlich, Thomas Stahnke, Stephan J. Linke, Sanaz Farrokhi, Maren Klemm, Stephan Allgeier, Bernd Köhler, Klaus-Martin Reichert, Rudolf F. Guthoff, **Sebastian Bohn**, and Oliver Stachs

With increasing interest in the cellular alteration of the cornea in ocular surface diseases, quantitative cellular characterization of the epithelium is becoming more important. This study presents a CLSM-based 3D *in vivo* image processing pipeline for morphological characterization and quantification of human epithelial cell layers.

For this purpose, 3D CLSM using the RCM 2.0 and the concave TomoCap was performed on 25 volunteers at both eyes in an age range of 25 to 62 years (mean age 44 years) to obtain full-thickness volume datasets of the epithelium.

After successful image registration and automated cell segmentation, the data sets were quantified by certain morphological parameters in dependence on a normalized depth scale that was defined from 0 to 1 according to superficial cells and SNP, respectively. The parameters included cell density, cell area, cell diameter, polygonality, neighborhood count, and Clark-Evans aggregation index (CE-Index) to analyze the cell pattern.

After manually checking all scans for contrast, signal-to-noise ratio, and the presence of superficial cells and SNP, a total of 43 scans of the 25 volunteers were used for segmentation and quantification. The concave TomoCap led to attenuated eye movements and thus to the median lateral projected area, in which all registered images of a stack contain information, of $45\,723\,\mu m^2$. Additionally, the piezo actuator controlling the TomoCap position proved to simplify and accelerate the acquisition process. Segmentation was most efficient for intermediate cells.

Morphological parameters varied from anterior to posterior as follows: Mean cell density increased with approx. 5200 cells/mm^2 to 8200 cells/mm^2 and correspondingly mean cell area and mean cell diameter decreased from 161.5 µm^2 to 90.3 µm^2 and 15.9 µm to 12.3 µm, respectively. Aggregation described by CE-Index increased gradually from 1.45 to 1.53. The mean neighborhood count first increased from 5.50 to a maximum of 5.66 and then decreased to 5.45. The mean polygonality gradually decreased from 4.93 to 4.64 sides of the cells.

In addition, the 25 volunteers were divided into three age groups. However, there was no age dependence of the morphological parameters found. This work demonstrated that the usability of a CLSM-based *in vivo* imaging pipeline for cellular characterization of the human corneal epithelium could be remarkably improved by the revised version of the RCM 2.0 and the concave TomoCap.

5. Summary

With the introduction of the RCM 2.0 in [P1], the focus control via the piezo actuator proved to be advantageous because the TomoCap no longer moves during the through-focusing, thus preventing compression artifacts or contact losses. Both effects are further enhanced by the concave cap. The adapted contact surface prevents compression of the cornea and additionally attenuates eye movements. Especially when considering 3D imaging, [P1] demonstrated that the combination of RCM 2.0, concave TomoCap, and elastic registration provides the best corneal CLSM 2D images and 3D reconstructions to date. The piezo actuator providing axial objective lens positioning ensures high precision, resulting in better depth assignment of each image and improving the quality of sagittal slices. The attenuation of eye movements using concave TomoCap demonstrably enables the acquisition of volumes with laterally more overlapping information. In contrast to the conventional RCM, the here developed RCM 2.0 now offers a range of scanning parameters and various scanning functions.

This is exploited in [P2], where an oscillating focal plane was successfully employed for a concept of reliable automated generation of large-scale SNP mosaics. Compared to the previous 2D methods, axial deviations of the SNP do no longer pose a problem.

At this point, it should be mentioned that in the use case of large-area mosaic imaging, the planar cap should be preferred over the concave cap, since large eye movements are desired in this case. Another disadvantage of the concave TomoCap is that the coupling process is more difficult due to the size of the cap and the resulting visual blockage. However, while in [P1] the lateral diameter of the concave contact area was 12 mm, other caps with smaller diameters of 10 mm and 9 mm were manufactured during this dissertation project and proved to be easier in handling. Another way to simplify and speed up the

coupling process would be to use an OCT approach as a supporting modality, as shown in [P3]. Although OCT image quality here cannot compete with other techniques using OCT as the main modality, it was shown to be a very useful tool for CLSM. In addition to the simplified coupling, it also provides supplementary information such as the position and orientation of the focal plane during imaging. At this point, it should also be mentioned again that OCT should not necessarily be seen as a competitor to CLSM, but that both imaging techniques are alternatives for different application purposes. As work [P3] also shows, these two techniques can support each other.

Furthermore, it was shown in [P3] that the RCM 2.0 can be used with other devices after minor modifications. The possible applications with other devices are further emphasized in [P4]. To make optimal use of multiple wavelengths, as in this case, a suitable lens with appropriate anti-reflective coatings should be used. However, changing the objective lens is an uncomplicated task with the RCM 2.0.

The results from [P5] demonstrate the clinical advantages of the RCM 2.0. Cross-sectional images obtained from the 3D datasets are similar to slit-lamp images that ophthalmologists are accustomed to but offer tremendously higher resolution. Additionally, the 3D information provides an *en face* image at every depth, which expands diagnostic capabilities. Furthermore, the advantage of the second piezo actuator to control the TomoCap became apparent in [P5]. Volumes axially larger than $500\,\mu m$ could be assembled, and the initial position of a volume acquisition can be adjusted faster and more precisely, even while already in contact with the cornea.

Finally, [P6] presents the results of the first automated quantification of corneal epithelial cells. Again, the RCM 2.0 with two piezo actuators and the concave TomoCap proved to be helpful. Depth-dependent characteristic quantities of the epithelium were obtained from the recorded 3D data sets. However, the quantification was performed only on the *en face* images. Future attempts will extend this to 3D morphology. A weakness that became evident is the unreliable imaging of the superficial cells with sufficient quality for automated evaluation. This occurs when the distance between the cap surface and the cornea is too small, resulting in interfering surface reflections from

the TomoCap. To address this, another TomoCap design has already been developed, which has a small indentation in the center of the concave contact surface to ensure a certain minimum distance between the cap surface and the cornea. The modularity of the RCM 2.0 has proven to be advantageous since it is now easy to transform existing laser scanning ophthalmoscopes into versatile corneal confocal microscopes. In clinical usage, the same device may be used for both retinal and corneal imaging. This saves costs and space that would come with a completely new device.

In conclusion, the RCM 2.0 in combination with the HRT, but potentially also with other laser scanning ophthalmoscopes, proves to be an extremely useful multi-functional tool to perform *in vivo* 2D and 3D CLSM both for scientific and clinical use. At this point, however, the development of RCM 2.0 is still not finished. For example, research is being conducted on further scanning strategies with regard to large-scale SNP mosaicking, including automated focus adjustment in combination with real-time tissue classification. Furthermore, work is ongoing to extend large-area mosaicking to other tissue layers and into the third dimension. Regarding the folds caused by the K-structures, an attempt is being made to control and monitor their formation by incorporating a force sensor into the RCM 2.0. In this context, it is also assumed that the folds can be used for orientation in order to better compare mosaics over longer periods of time.

Personal contribution statement

[P1] - S. Bohn et. al, Biomed. Opt. Express 9(6), 2511–2525 (2018)
Design and assembly of the initial version of the RCM 2.0; programming of the RCM 2.0 control and monitoring system; design and development of the concave TomoCap; data acquisition, analysis, and processing; creation of all figures; drafting of the entire manuscript; critical revision.

[P2] - S. Allgeier et. al, Scientific reports 8(1), 7468 (2018)
Partial programming of the communication interface (EyeGuidance, HRT, RCM 2.0); data acquisition, partial creation of figures; partial drafting of the manuscript, mainly regarding RCM 2.0, critical revision.

[P3] - S. Bohn et. al, Biomed. Opt. Express 10(5), 2580–2587 (2019)
Design and assembly of the modular RCM 2.0 adapter; data acquisition, analysis, and processing; creation of all figures; drafting of the entire manuscript; critical revision.

[P4] - S. Bohn et. al, Biomed. Opt. Express 11(10), 5689–5700 (2020)
Design and assembly of the modular RCM 2.0 adapter; data acquisition, analysis, and processing; creation of all figures; drafting of the entire manuscript; critical revision.

[P5] - S. Bohn et. al, Klin. Monbl. Augenheilkd. 237(12), 1442–1454 (2020)
Design and assembly of the revised version of the RCM 2.0 including the piezo actuator controlling the TomoCap position; partial data acquisition, analysis, and processing; creation of all CLSM figures and RCM 2.0 figures; partial drafting of the manuscript; critical revision.

[P6] - Sterenczak et. al, Quant. Imaging. Med. Surg. 11(5), 1737–1750 (2021)
Design and assembly of the revised version of the RCM 2.0 including the piezo actuator controlling the TomoCap position; data acquisition; partial data analysis and processing; creation of RCM 2.0 figures; partial drafting of the manuscript; critical revision.

List of publications

[P1]   S. Bohn, K. Sperlich, S. Allgeier, A. Bartschat, R. Prakasam, K.-M. Reichert, H. Stolz, R. F. Guthoff, R. Mikut, B. Köhler, and O. Stachs. "Cellular in vivo 3D imaging of the cornea by confocal laser scanning microscopy." Biomedical Optics Express 9(6), 2511–2525 (2018).

[P2]   S. Allgeier, A. Bartschat, S. Bohn, S. Peschel, K.-M. Reichert, K. Sperlich, M. Walckling, V. Hagenmeyer, R. Mikut, O. Stachs, and B. Köhler. "3D confocal laser-scanning microscopy for large-area imaging of the corneal subbasal nerve plexus." Scientific reports 8(1), 7468 (2018).

[P3]   S. Bohn, K. Sperlich, H. Stolz, R. F. Guthoff, and O. Stachs. "In vivo corneal confocal microscopy aided by optical coherence tomography." Biomedical Optics Express 10(5), 2580–2587 (2019).

[P4]   S. Bohn, K. Sperlich, T. Stahnke, M. Schünemann, H. Stolz, R. F. Guthoff, and O. Stachs. "Multiwavelength confocal laser scanning microscopy of the cornea." Biomedical Optics Express 11(10), 5689–5700 (2020).

[P5]   S. Bohn, T. Stahnke, K. Sperlich, S. J. Linke, S. Farrokhi, M. Klemm, S. Allgeier, B. Köhler, K.-M. Reichert, M. Witt, O. Stachs, and R. F. Guthoff. "In vivo Histology of the Cornea - from the 'Rostock Cornea Module' to the 'Rostock Electronic Slit Lamp' - a Clinical 'Proof of Concept' Study." Klinische Monatsblätter fur Augenheilkunde 237(12), 1442–1454 (2020).

[P6]   K. A. Sterenczak, K. Winter, K. Sperlich, T. Stahnke, S. Linke, S. Farrokhi, M. Klemm, S. Allgeier, B. Köhler, K.-M. Reichert, R. F. Guthoff, S. Bohn, and O. Stachs. "Morphological characterization of the human corneal epithelium by in vivo confocal laser scanning microscopy." Quantitative imaging in medicine and surgery 11(5), 1737–1750 (2021).

References

[1] U. Eysel. "Sehen: Licht, Auge und Abbildung." In: *Physiologie des Menschen.* Ed. by R. Brandes, F. Lang, and R. F. Schmidt. Springer Berlin Heidelberg, 2019, 723–731.

[2] F. Grehn. "Hornhaut." In: *Augenheilkunde.* Berlin, Heidelberg: Springer Berlin Heidelberg, 2019, 141–188.

[3] R. V. Krstic. "Sensory Systems." In: *Human Microscopic Anatomy.* Springer Berlin Heidelberg, 1991, 505–583.

[4] O. Kermani, W. Fabian, and H. Lubatschowski. "Real-Time Optical Coherence Tomography-Guided Femtosecond Laser Sub-Bowman Keratomileusis on Human Donor Eyes." American Journal of Ophthalmology 146(1), 42–45 (2008).

[5] C. F. Marfurt. "Corneal nerves: anatomy." In: *Encyclopedia of the Eye.* Ed. by D. A. Dartt. Elsevier, 2010, 485–492.

[6] A. J. Rózsa and R. W. Beuerman. "Density and organization of free nerve endings in the corneal epithelium of the rabbit." Pain 14(2), 105–120 (1982).

[7] A. Gullstrand. "Die Nernstspaltlampe in der ophthalmologischen Praxis." In: M.-M. Gellrich. *Die Spaltlampe.* Ed. by D. Schmidt. Heidelberg: Kaden, Heidelberg, 2011, 165–179.

[8] M.-M. Gellrich. "History of the Slit Lamp." In: *The Slit Lamp: Applications for Biomicroscopy and Videography.* Berlin, Heidelberg: Springer Berlin Heidelberg, 2014, 189–210.

[9] A. Gullstrand. *Einführung in die Methoden der Dioptrik des Auges des Menschen.* Verlag von S. Hirzel, 1911.

References

[10] NobelPrize.org, Nobel Media AB. *The Nobel Prize in Physiology or Medicine 1911.* 2021. URL: https://www.nobelprize.org/prizes/medicine/1911/summary/ (visited on 05/08/2021).

[11] A. Vogt. *Lehrbuch und Atlas der Spaltlampenmikroskopie des Lebenden Auges.* Springer Berlin Heidelberg, 1931.

[12] M.-M. Gellrich. *Die Spaltlampe.* Ed. by D. Schmidt. Heidelberg: Kaden, Heidelberg, 2011.

[13] R. Martin. "Cornea and anterior eye assessment with slit lamp biomicroscopy, specular microscopy, confocal microscopy, and ultrasound biomicroscopy." Indian journal of ophthalmology 66(2), 195–201 (2018).

[14] G. E. Rose. "Clinical assessment of corneal endothelial cell density: an original system of grading using a slit-lamp biomicroscope." British Journal of Ophthalmology 70(7), 510–515 (1986).

[15] R. F. Guthoff, A. Zhivov, and O. Stachs. "In vivo confocal microscopy, an inner vision of the cornea – a major review." Clinical & Experimental Ophthalmology 37(1), 100–117 (2009).

[16] O. Stachs, R. F. Guthoff, and S. Aumann. "In Vivo Confocal Scanning Laser Microscopy." In: *High Resolution Imaging in Microscopy and Ophthalmology: New Frontiers in Biomedical Optics.* Ed. by J. F. Bille. Cham: Springer International Publishing, 2019, 263–284.

[17] J. Stave, G. Zinser, G. Grümmer, and R. Guthoff. "Der modifizierte Heidelberg-Retina-Tomograph HRTErste Ergebnisse einer In-vivo-Darstellung von kornealen Strukturen." Der Ophthalmologe 99(4), 276–280 (2002).

[18] L. Daas, A. Viestenz, M. Bischoff, A. Hasenfus, and B. Seitz. "Confocal microscopy for the diagnostics of fungal keratitis." Der Ophthalmologe: Zeitschrift der Deutschen Ophthalmologischen Gesellschaft 113(9), 767–771 (2016).

[19] R. Chopra, P. J. Mulholland, and S. C. Hau. "In Vivo Confocal Microscopy Morphologic Features and Cyst Density in Acanthamoeba Keratitis." American Journal of Ophthalmology 217, 38–48 (2020).

[20] S. Li, J. Bian, Y. Wang, S. Wang, X. Wang, and W. Shi. "Clinical features and serial changes of Acanthamoeba keratitis: an in vivo confocal microscopy study." Eye 34(2), 327–334 (2020).

48

[21] L. Daas, M. Bischoff-Jung, A. Viestenz, and B. Seitz. "Confocal microscopy as an early relapse marker after keratoplasty due to Fusarium solani keratitis." Der Ophthalmologe: Zeitschrift der Deutschen Ophthalmologischen Gesellschaft 114(1), 66–69 (2017).

[22] W. J. Behrens-Baumann, W. Hofmüller, I. Tammer, and K. Tintelnot. "Keratomycosis due to Tintelnotia destructans refractory to common therapy treated successfully with systemic and local terbinafine in combination with polyhexamethylene biguanide." International Ophthalmology 39(6), 1379–1385 (2019).

[23] E. C. Ledbetter, N. L. Irby, and L. B. Teixeira. "In vivo confocal microscopy characteristics of equine epithelial and subepithelial nonulcerative keratomycosis." Veterinary Ophthalmology 22(2), 168–176 (2019).

[24] K. I. Kinard, A. G. Smith, J. R. Singleton, M. K. Lessard, B. J. Katz, J. E. Warner, A. V. Crum, M. D. Mifflin, K. C. Brennan, and K. B. Digre. "Chronic Migraine Is Associated With Reduced Corneal Nerve Fiber Density and Symptoms of Dry Eye." Headache: The Journal of Head and Face Pain 55(4), 543–549 (2015).

[25] R. Shetty, R. Deshmukh, R. Shroff, C. Dedhiya, and C. Jayadev. "Subbasal Nerve Plexus Changes in Chronic Migraine." Cornea 37(1) (2018).

[26] F. Shen, X. Dong, X. Zhou, L. Yan, and Q. Wan. "Corneal subbasal nerve plexus changes in patients with episodic migraine: an in vivo confocal microscopy study." Journal of pain research 12, 1489–1495 (2019).

[27] J.-I. Lee, T. Böcking, D. Holle-Lee, R. A. Malik, B. C. Kieseier, H.-P. Hartung, R. Guthoff, C. Kleinschnitz, and M. Stettner. "Corneal Confocal Microscopy Demonstrates Corneal Nerve Loss in Patients With Trigeminal Neuralgia." Frontiers in Neurology 11, 661 (2020).

[28] G. Bitirgen, Z. Akpinar, R. A. Malik, and A. Ozkagnici. "Use of Corneal Confocal Microscopy to Detect Corneal Nerve Loss and Increased Dendritic Cells in Patients With Multiple Sclerosis." JAMA Ophthalmology 135(7), 777–782 (2017).

References

[29] I. N. Petropoulos, S. Kamran, Y. Li, A. Khan, G. Ponirakis, N. Akhtar, D. Deleu, A. Shuaib, and R. A. Malik. "Corneal Confocal Microscopy: An Imaging Endpoint for Axonal Degeneration in Multiple Sclerosis." Investigative Ophthalmology & Visual Science 58(9), 3677–3681 (2017).

[30] V. Testa, N. De Santis, R. Scotto, C. E. Pastorino, M. Cellerino, S. Olivari, A. J. Morlacchi, M. Inglese, A. Uccelli, C. E. Traverso, and M. Iester. "Neuroaxonal Degeneration in Patients With Multiple Sclerosis: An Optical Coherence Tomography and in Vivo Corneal Confocal Microscopy Study." Cornea 39(10) (2020).

[31] V. Testa, N. De Santis, R. Scotto, P. Della Giustina, L. Ferro Desideri, M. Cellerino, C. Cordano, M. Inglese, A. Uccelli, A. Vagge, C. E. Traverso, and M. Iester. "Corneal epithelial dendritic cells in patients with multiple sclerosis: An in vivo confocal microscopy study." Journal of Clinical Neuroscience 81, 139–143 (2020).

[32] A. Rousseau, C. Cauquil, B. Dupas, A. Labbé, C. Baudouin, E. Barreau, M. Théaudin, C. Lacroix, A. Guiochon-Mantel, A. Benmalek, M. Labetoulle, and D. Adams. "Potential Role of In Vivo Confocal Microscopy for Imaging Corneal Nerves in Transthyretin Familial Amyloid Polyneuropathy." JAMA Ophthalmology 134(9), 983–989 (2016).

[33] Y. Zhang, Z. Liu, Y. Zhang, H. Wang, X. Liu, S. Zhang, X. Liu, and D. Fan. "Corneal sub-basal whorl-like nerve plexus: a landmark for early and follow-up evaluation in transthyretin familial amyloid polyneuropathy." European Journal of Neurology (2020).

[34] S. L. Misra, H. M. Kersten, R. H. Roxburgh, H. V. Danesh-Meyer, and C. N. J. McGhee. "Corneal nerve microstructure in Parkinson's disease." Journal of clinical neuroscience : official journal of the Neurosurgical Society of Australasia 39, 53–58 (2017).

[35] N.-N. Che and H.-Q. Yang. "Potential use of corneal confocal microscopy in the diagnosis of Parkinson's disease associated neuropathy." Translational Neurodegeneration 9(1), 28 (2020).

[36] S. H. Lim, M. Ferdousi, A. Kalteniece, L. Kass-Iliyya, I. N. Petropoulos, R. A. Malik, C. Kobylecki, and M. Silverdale. "Corneal confocal microscopy detects small fibre neurodegeneration in Parkinson's disease using automated analysis." Scientific Reports 10(1), 20147 (2020).

[37] S. H. Lim, M. Ferdousi, A. Kalteniece, Z. R. Mahfoud, I. N. Petropoulos, R. A. Malik, C. Kobylecki, and M. Silverdale. "Corneal Confocal Microscopy Identifies Parkinson's Disease with More Rapid Motor Progression." Movement Disorders (2021).

[38] E. E. B. De Clerck, J. S. A. G. Schouten, T. T. J. M. Berendschot, A. G. H. Kessels, R. M. M. A. Nuijts, H. J. M. Beckers, M. T. Schram, C. D. A. Stehouwer, and C. A. B. Webers. "New ophthalmologic imaging techniques for detection and monitoring of neurodegenerative changes in diabetes: a systematic review." The Lancet Diabetes & Endocrinology 3(8), 653–663 (2015).

[39] S. L. Misra, J. P. Craig, D. V. Patel, C. N. J. McGhee, M. Pradhan, K. Ellyett, D. Kilfoyle, and G. D. Braatvedt. "In Vivo Confocal Microscopy of Corneal Nerves: An Ocular Biomarker for Peripheral and Cardiac Autonomic Neuropathy in Type 1 Diabetes Mellitus." Investigative Ophthalmology & Visual Science 56(9), 5060–5065 (2015).

[40] E. A. Deák, E. Szalai, N. Tóth, R. A. Malik, A. Berta, and A. Csutak. "Longitudinal Changes in Corneal Cell and Nerve Fiber Morphology in Young Patients with Type 1 Diabetes with and without Diabetic Retinopathy: A 2-Year Follow-up Study." Investigative Ophthalmology & Visual Science 60(2), 830–837 (2019).

[41] Q. Li, Y. Zhong, T. Zhang, R. Zhang, Q. Zhang, H. Zheng, L. Ji, W. Sun, X. Zhu, S. Zhang, X. Liu, B. Lu, and Q. Xiong. "Quantitative analysis of corneal nerve fibers in type 2 diabetics with and without diabetic peripheral neuropathy: Comparison of manual and automated assessments." Diabetes Research and Clinical Practice 151, 33–38 (2019).

[42] I. N. Petropoulos, A. Al-Mohammedi, X. Chen, M. Ferdousi, G. Ponirakis, H. Kemp, R. Chopra, S. Hau, M. Schargus, J. Vollert, D. Sturm, T. Bharani, C. Kleinschnitz, M. Stettner, T. Peto, C. Maier, A. S. C. Rice, and R. A. Malik. "The Utility of Corneal Nerve Fractal Dimension Analysis in Peripheral

Neuropathies of Different Etiology." Translational Vision Science & Technology 9(9), 43–43 (2020).

[43] K. Alise, F. Maryam, A. Shazli, W. M. Mubita, A. Marshall, G. Lauria, C. G. Faber, S. Handrean, and R. A. Malik. "Corneal confocal microscopy detects small nerve fibre damage in patients with painful diabetic neuropathy." Scientific Reports (Nature Publisher Group) 10(1) (2020).

[44] A. M. Roszkowska, C. Licitra, G. Tumminello, E. I. Postorino, M. R. Colonna, and P. Aragona. "Corneal nerves in diabetes—The role of the in vivo corneal confocal microscopy of the subbasal nerve plexus in the assessment of peripheral small fiber neuropathy." Survey of Ophthalmology (2020).

[45] M. Fleischer, I. Lee, F. Erdlenbruch, L. Hinrichs, I. N. Petropoulos, R. A. Malik, H.-P. Hartung, B. C. Kieseier, C. Kleinschnitz, and M. Stettner. "Corneal confocal microscopy differentiates inflammatory from diabetic neuropathy." Journal of Neuroinflammation 18(1), 89 (2021).

[46] D. V. Patel and C. N. J. McGhee. "Mapping of the Normal Human Corneal Sub-Basal Nerve Plexus by In Vivo Laser Scanning Confocal Microscopy." Investigative Ophthalmology & Visual Science 46(12), 4485–4488 (2005).

[47] D. Vagenas, N. Pritchard, K. Edwards, A. M. Shahidi, G. P. Sampson, A. W. Russell, R. A. Malik, and N. Efron. "Optimal Image Sample Size for Corneal Nerve Morphometry." Optometry and Vision Science 89(5) (2012).

[48] A. Kheirkhah, R. Muller, J. Mikolajczak, A. Ren, E. M. Kadas, H. Zimmermann, H. Pruess, F. Paul, A. U. Brandt, and P. Hamrah. "Comparison of Standard Versus Wide-Field Composite Images of the Corneal Subbasal Layer by In Vivo Confocal Microscopy." Investigative Ophthalmology & Visual Science 56(10), 5801–5807 (2015).

[49] S. Allgeier, S. Maier, R. Mikut, S. Peschel, K.-M. Reichert, O. Stachs, and B. Köhler. "Mosaicking the Subbasal Nerve Plexus by Guided Eye Movements." Investigative Ophthalmology & Visual Science 55(9), 6082–6089 (2014).

[50] B. Köhler, G. Bretthauer, R. F. Guthoff, K.-M. Reichert, I. Sieber, O. Stachs, L. Toso, and S. Allgeier. "EyeGuidance – a computer controlled system to guide eye movements." Current Directions in Biomedical Engineering 2(1), 433–436 (2016).

[51] S. Allgeier, A. Zhivov, F. Eberle, B. Koehler, S. Maier, G. Bretthauer, R. F. Guthoff, and O. Stachs. "Image Reconstruction of the Subbasal Nerve Plexus with In Vivo Confocal Microscopy." Investigative Ophthalmology & Visual Science 52(9), 5022–5028 (2011).

[52] S. Allgeier, B. Köhler, F. Eberle, S. Maier, O. Stachs, A. Zhivov, and G. Bretthauer. "Elastische Registrierung von in-vivo-CLSM-Aufnahmen der Kornea." In: *Bildverarbeitung für die Medizin 2011: Algorithmen - Systeme - Anwendungen Proceedings des Workshops vom 20. - 22. März 2011 in Lübeck.* Ed. by H. Handels, J. Ehrhardt, T. M. Deserno, H.-P. Meinzer, and T. Tolxdorff. Berlin, Heidelberg: Springer Berlin Heidelberg, 2011, 149–153.

[53] V. I. Arnold. "Geometry of Conic Sections." In: *Real Algebraic Geometry.* Ed. by I. Itenberg, V. Kharlamov, and E. I. Shustin. Berlin, Heidelberg: Springer Berlin Heidelberg, 2013, 3–18.

[54] J. Fischer, T. Otto, F. Delori, L. Pace, and G. Staurenghi. "Scanning Laser Ophthalmoscopy (SLO)." In: *High Resolution Imaging in Microscopy and Ophthalmology: New Frontiers in Biomedical Optics.* Ed. by J. F. Bille. Cham: Springer International Publishing, 2019, 35–57.

[55] B. Amos, G. McConnell, and T. Wilson. "Confocal Microscopy." In: *Comprehensive Biophysics.* Ed. by E. H. Egelman. Elsevier B.V., 2019.

[56] M. Minsky. "Memoir on inventing the confocal scanning microscope." Scanning 10(4), 128–138 (1988).

[57] R. H. Webb, G. W. Hughes, and O. Pomerantzeff. "Flying spot TV ophthalmoscope." Applied Optics 19(17), 2991–2997 (1980).

[58] R. H. Webb, G. W. Hughes, and F. C. Delori. "Confocal scanning laser ophthalmoscope." Applied Optics 26(8), 1492–1499 (1987).

[59] H. D. Cavanagh, J. V. Jester, J. Essepian, W. Shields, and M. A. Lemp. "Confocal Microscopy of the Living Eye." Eye & Contact Lens 16(1) (1990).

[60] M. Petráň, M. Hadravský, M. D. Egger, and R. Galambos. "Tandem-Scanning Reflected-Light Microscope∗." Journal of the Optical Society of America 58(5), 661–664 (1968).

[61] B. R. Masters and A. A. Thaer. "Real-time scanning slit confocal microscopy of the invivohuman cornea." Applied Optics 33(4), 695–701 (1994).

[62] S. R. Goldstein, T. Hubin, S. Rosenthal, and C. Washburn. "A confocal video-rate laser-beam scanning reflected-light microscope with no moving parts." Journal of Microscopy 157(1), 29–38 (1990).

[63] *Heidelberg Retina Tomograph 2 Operating Instructions of Software Version 1.1*. Dossenheim Germany: Heidelberg Engineering GmbH, 2004.

[64] A. Zhivov, O. Stachs, J. Stave, and R. F. Guthoff. "In vivo three-dimensional confocal laser scanning microscopy of corneal surface and epithelium." British Journal of Ophthalmology 93(5), 667–672 (2009).

[65] T. Deguchi, P. Bianchini, G. Palazzolo, M. Oneto, A. Diaspro, and M. Duocastella. "Volumetric Lissajous confocal microscopy with tunable spatiotemporal resolution." Biomedical Optics Express 11(11), 6293–6310 (2020).

[66] A. Badon, S. Bensussen, H. J. Gritton, M. R. Awal, C. V. Gabel, X. Han, and J. Mertz. "Video-rate large-scale imaging with Multi-Z confocal microscopy." Optica 6(4), 389–395 (2019).

[67] C. Olsovsky, R. Shelton, O. Carrasco-Zevallos, B. E. Applegate, and K. C. Maitland. "Chromatic confocal microscopy for multi-depth imaging of epithelial tissue." Biomedical Optics Express 4(5), 732–740 (2013).

[68] X. Chen, T. Nakamura, Y. Shimizu, C. Chen, Y.-L. Chen, H. Matsukuma, and W. Gao. "A chromatic confocal probe with a mode-locked femtosecond laser source." Optics & Laser Technology 103, 359–366 (2018).

[69] C. Chen, R. Sato, Y. Shimizu, T. Nakamura, H. Matsukuma, and W. Gao. "A Method for Expansion of Z-Directional Measurement Range in a Mode-Locked Femtosecond Laser Chromatic Confocal Probe." Applied Sciences 9(3), 454 (2019).

[70] D. Jeong, S. J. Park, H. Jang, H. Kim, J. Kim, and C.-S. Kim. "Swept-Source-Based Chromatic Confocal Microscopy." Sensors 20(24), 7347 (2020).

[71] A. F. Fercher, C. K. Hitzenberger, W. Drexler, G. Kamp, and H. Sattmann. "In Vivo Optical Coherence Tomography." American Journal of Ophthalmology 116(1), 113–114 (1993).

[72] J. A. Izatt, M. R. Hee, E. A. Swanson, C. P. Lin, D. Huang, J. S. Schuman, C. A. Puliafito, and J. G. Fujimoto. "Micrometer-Scale Resolution Imaging of the Anterior Eye In Vivo With Optical Coherence Tomography." Archives of Ophthalmology 112(12), 1584–1589 (1994).

[73] J. Welzel, E. Lankenau, R. Birngruber, and R. Engelhardt. "Optical coherence tomography of the human skin." Journal of the American Academy of Dermatology 37(6), 958–963 (1997).

[74] S. Aumann, S. Donner, J. Fischer, and F. Müller. "Optical Coherence Tomography (OCT): Principle and Technical Realization." In: *High Resolution Imaging in Microscopy and Ophthalmology: New Frontiers in Biomedical Optics.* Ed. by J. F. Bille. Cham: Springer International Publishing, 2019, 59–85.

[75] D. Huang, E. A. Swanson, C. P. Lin, J. S. Schuman, W. G. Stinson, W. Chang, M. R. Hee, T. Flotte, K. Gregory, and C. A. Puliafito. "Optical coherence tomography." Science (New York, N.Y.) 254, 1178–1181 (1991).

[76] A. Fercher, C. Hitzenberger, G. Kamp, and S. El-Zaiat. "Measurement of intraocular distances by backscattering spectral interferometry." Optics Communications 117(1), 43–48 (1995).

[77] S. R. Chinn, E. A. Swanson, and J. G. Fujimoto. "Optical coherence tomography using a frequency-tunable optical source." Optics Letters 22(5), 340–342 (1997).

[78] J. P. Kolb, T. Pfeiffer, M. Eibl, H. Hakert, and R. Huber. "High-resolution retinal swept source optical coherence tomography with an ultra-wideband Fourier-domain mode-locked laser at MHz A-scan rates." Biomedical Optics Express 9(1), 120–130 (2018).

[79] B. Tan, Z. Hosseinaee, L. Han, O. Kralj, L. Sorbara, and K. Bizheva. "250 kHz, 1.5 µm resolution SD-OCT for in-vivo cellular imaging of the human cornea." Biomedical Optics Express 9(12), 6569–6583 (2018).

[80] X. Yao, K. Devarajan, R. M. Werkmeister, V. A. dos Santos, M. Ang, A. Kuo, D. W. K. Wong, J. Chua, B. Tan, V. A. Barathi, and L. Schmetterer. "In vivo corneal endothelium imaging using ultrahigh resolution OCT." Biomedical Optics Express 10(11), 5675–5686 (2019).

[81] Z. Hosseinaee, B. Tan, O. Kralj, L. Han, A. Wong, L. Sorbara, and K. Bizheva. "Fully automated corneal nerve segmentation algorithm for corneal nerves analysis from in-vivo UHR-OCT images." In: *Ophthalmic Technologies XXIX*. Ed. by F. Manns, P. G. Söderberg, and A. Ho. Vol. 10858. International Society for Optics and Photonics. SPIE, 2019, 105–110.

[82] C. Canavesi, A. Cogliati, A. Mietus, Y. Qi, J. Schallek, J. P. Rolland, and H. B. Hindman. "In vivo imaging of corneal nerves and cellular structures in mice with Gabor-domain optical coherence microscopy." Biomedical Optics Express 11(2), 711–724 (2020).

[83] V. Mazlin, P. Xiao, J. Scholler, K. Grieve, K. Irsch, J.-A. Sahel, M. Fink, and C. Boccara. "Ultra-High Resolution Full-Field OCT (FFOCT) for Cornea and Retina." In: *Imaging and Applied Optics 2018 (3D, AO, AIO, COSI, DH, IS, LACSEA, LS&C, MATH, pcAOP)*. Optical Society of America, 2018, IM3B.1.

[84] V. Mazlin, P. Xiao, J. Scholler, K. Irsch, K. Grieve, M. Fink, and A. C. Boccara. "Real-time non-contact cellular imaging and angiography of human cornea and limbus with common-path full-field/SD OCT." Nature Communications 11(1), 1868 (2020).

[85] E. Auksorius, D. Borycki, P. Stremplewski, K. Liżewski, S. Tomczewski, P. Niedźwiedziuk, B. L. Sikorski, and M. Wojtkowski. "In vivo imaging of the human cornea with high-speed and high-resolution Fourier-domain full-field optical coherence tomography." Biomedical Optics Express 11(5), 2849–2865 (2020).

[86] Y.-T. Chen, C.-Y. Tsai, Y.-K. Chiu, T.-W. Hsu, L. W. Chen, W.-L. Chen, and S.-L. Huang. "En Face and Cross-sectional Corneal Tomograms Using Sub-micron spatial resolution Optical Coherence Tomography." Scientific Reports 8(1), 14349 (2018).

[87] V. Mazlin, K. Irsch, M. Paques, J.-A. Sahel, M. Fink, and C. A. Boccara. "Curved-field optical coherence tomography: large-field imaging of human corneal cells and nerves." Optica 7(8), 872 (2020).

[88] A. Wartak, M. S. Schenk, V. Bühler, S. A. Kassumeh, R. Birngruber, and G. J. Tearney. "Micro-optical coherence tomography for high-resolution morphologic

imaging of cellular and nerval corneal micro-structures." Biomedical Optics Express 11(10), 5920–5933 (2020).

[89] A. Kobayashi, H. Yokogawa, and K. Sugiyama. "In Vivo Laser Confocal Microscopy of Bowman's Layer of the Cornea." Ophthalmology 113(12), 2203–2208 (2006).

[90] A. J. Bron. "Anterior corneal mosaic." The British journal of ophthalmology 52(9), 659–669 (1968).

[91] ImageJ. *Image Processing and Analysis in Java.* 2021. URL: https://imagej.nih.gov/ij/ (visited on 05/11/2021).

[92] A. Bartschat, L. Toso, J. Stegmaier, A. Kuijper, R. Mikut, B. Köhler, and S. Allgeier. "Automatic corneal tissue classification using bag-of visual-words approaches." In: *Forum Bildverarbeitung 2016.* Vol. 84. 7-8. KIT Scientific Publishing. 2016, 245.

Part II.

Publications

Cellular *in vivo* 3D imaging of the cornea by confocal laser scanning microscopy

Sebastian Bohn, Karsten Sperlich, Stephan Allgeier, Andreas Bartschat, Rubi Prakasam, Klaus-Martin Reichert, Heinrich Stolz, Rudolf F. Guthoff, Ralf Mikut, Bernd Köhler, and Oliver Stachs

Copyright notice

Cellular *in vivo* 3D imaging of the cornea by confocal laser scanning microscopy

SEBASTIAN BOHN,[1,*] KARSTEN SPERLICH,[1] STEPHAN ALLGEIER,[2] ANDREAS BARTSCHAT,[2] RUBY PRAKASAM,[1] KLAUS-MARTIN REICHERT,[2] HEINRICH STOLZ,[3] RUDOLF GUTHOFF,[1] RALF MIKUT,[2] BERND KÖHLER,[2] AND OLIVER STACHS[1]

[1]*Department of Ophthalmology, University Medical Center Rostock, 18057 Rostock, Germany*
[2]*Institute for Automation and Applied Informatics, Karlsruhe Institute of Technology, 76131 Karlsruhe, Germany*
[3]*Institute of Physics, University of Rostock, 18059 Rostock, Germany*
*sebastian.bohn@uni-rostock.de

Abstract: We present an *in vivo* confocal laser scanning microscopy based method for large 3D reconstruction of the cornea on a cellular level with cropped volume sizes up to 266 x 286 x 396 μm^3. The microscope objective used is equipped with a piezo actuator for automated, fast and precise closed-loop focal plane control. Furthermore, we present a novel concave surface contact cap, which significantly reduces eye movements by up to 87%, hence increasing the overlapping image area of the whole stack. This increases the cuboid volume of the generated 3D reconstruction significantly. The possibility to generate oblique sections using isotropic volume stacks opens the window to slit lamp microscopy on a cellular level.

References and links

1. J. Stave, G. Zinser, G. Grümmer, and R. F. Guthoff, "Modified Heidelberg Retinal Tomograph HRT. Initial results of in vivo presentation of corneal structures," Ophthalmologe **99**(4), 276–280 (2002).
2. M. D. Twa and M. J. Giese, "Assessment of Corneal Thickness and Keratocyte Density in a Rabbit Model of Laser In Situ Keratomileusis Using Scanning Laser Confocal Microscopy," Am. J. Ophthalmol. **152**(6), 941–953 (2011).
3. A. Labbé, H. Liang, C. Martin, F. Bringole-Baudouin, J.-M. Warnet, and C. Baudouin, "Comparative Anatomy of Laboratory Animal Corneas with a New-Generation High-Resolution In Vivo Confocal Microscope," Curr. Eye Res. **31**(6), 501–509 (2006).
4. C. Mazzotta, A. Balestrazzi, C. Traversi, S. Baiocchi, T. Caporossi, C. Tommasi, and A. Caporossi, "Treatment of Progressive Keratoconus by Riboflavin-UVA-Induced Cross-Linking of Corneal Collagen: Ultrastructural Analysis by Heidelberg Retinal Tomograph II In Vivo Confocal Microscopy in Humans," Cornea **26**(4), 390–397 (2007).
5. W. M. Petroll, M. Weaver, S. Vaidya, J. P. McCulley, and H. D. Cavanagh, "Quantitative 3-D Corneal Imaging In Vivo Using a Modified HRT- RCM Confocal Microscope," Cornea **32**(4), e36–e43 (2013).
6. R. Prakasam, K. Winter, M. Schwiede, S. Allgeier, A. Zhivov, B. Köhler, R. F. Guthoff, and O. Stachs, "Characteristic Quantities of Corneal Epithelial Structures in Confocal Laser Scanning Microscopic Volume Data Sets," Cornea **32**(5), 636–643 (2013).
7. S. Allgeier, A. Zhivov, F. Eberle, B. Köhler, S. Maier, G. Bretthauer, R. F. Guthoff, and O. Stachs, "Image Reconstruction of the Subbasal Nerve Plexus with In Vivo Confocal Microscopy," Invest. Ophthalmol. Vis. Sci. **52**(9), 5022–5028 (2011).
8. A. Zhivov, M. Blum, R. F. Guthoff, and O. Stachs, "Real-time mapping of the subepithelial nerve plexus by in vivo confocal laser scanning microscopy," Br. J. Ophthalmol. **94**(9), 1133–1135 (2010).
9. J. T. Turuwhenua, D. V. Patel, and C. N. J. McGhee, "Fully Automated Montaging of Laser Scanning In Vivo Confocal Microscopy Images of the Human Corneal Subbasal Nerve Plexus," Invest. Ophthalmol. Vis. Sci. **53**(4), 2235–2242 (2012).
10. K. Edwards, N. Pitchard, K. Gosschalk, G. P. Sampson, A. Russell, R. A. Malik, and N. Efron, "Wide-Field Assessment of the Human Corneal Subbasal Nerve Plexus in Diabetic Neuropathy Using a Novel Mapping Technique," Cornea **31**(9), 1078–1082 (2012).

11. E. Poletti, J. Wigdahl, P. Guimarães, and A. Ruggeri, "Automatic montaging of corneal sub-basal nerve images for the composition of a wide-range mosaic," in *Proceedings of the 2014 36th Annual International Conference of the IEEE Engineering in Medicine and Biology Society (IEEE, 2004), pp.* 5426–5439.
12. S. Allgeier, S. Maier, R. Mikut, S. Peschel, K.-M. Reichert, O. Stachs, and B. Köhler, "Mosaicking the Subbasal Nerve Plexus by Guided Eye Movements," Invest. Ophthalmol. Vis. Sci. **55**(9), 6082–6089 (2014).
13. B. Köhler, S. Allgeier, F. Eberle, S. Maier, S. Peschel, K.-M. Reichert, and O. Stachs, "Large-Scale Imaging of Corneal Nerve Fibres by Guided Eye Movements," Klin. Monatsbl. Augenheilkd. **231**(12), 1170–1173 (2014).
14. E. Beaurepaire, A. C. Boccara, M. Lebec, L. Blanchot, and H. Saint-Jalmes, "Full-field optical coherence microscopy," Opt. Lett. **23**(4), 244–246 (1998).
15. V. Mazlin, P. Xiao, E. Dalimier, K. Grieve, K. Irsch, J.-A. Sahel, M. Fink, and A. C. Boccara, "In vivo high resolution human corneal imaging using full-field optical coherence tomography," Biomed. Opt. Express **9**(2), 557–568 (2018).
16. H. F. Li, W. M. Petroll, T. Møller-Pedersen, J. K. Maurer, H. D. Cavanagh, and J. V. Jester, "Epithelial and corneal thickness measurements by in vivo confocal microscopy through focusing (CMTF)," Curr. Eye Res. **16**(3), 214–221 (1997).
17. O. Stachs, A. Zhivov, R. Kraak, J. Stave, and R. F. Guthoff, "In vivo three-dimensional confocal laser scanning microscopy of the epithelial nerve structure in the human cornea," Graefes Arch. Clin. Exp. Ophthalmol. **245**(4), 569–575 (2007).
18. A. Zhivov, O. Stachs, J. Stave, and R. F. Guthoff, "In vivo three-dimensional confocal laser scanning microscopy of corneal surface and epithelium," Br. J. Ophthalmol. **93**(5), 667–672 (2009).
19. A. J. Bron, "Anterior corneal mosaic," Br. J. Ophthalmol. **52**(9), 659–669 (1968).
20. A. J. Bron and R. C. Tripathi, "Anterior corneal mosaic. Further observations," Br. J. Ophthalmol. **53**(11), 760–764 (1969).
21. A. Kobayashi, H. Yokogawa, and K. Sugiyama, "In Vivo Laser Confocal Microscopy of Bowman's Layer of the Cornea," Ophthalmology **113**(12), 2203–2208 (2006).
22. H. Yokogawa, A. Kobayashi, and K. Sugiyama, "Mapping of Normal Corneal K-Structures by In Vivo Laser Confocal Microscopy," Cornea **27**(8), 879–883 (2008).
23. R. F. Guthoff, C. Baudouin, and J. Stave, *Atlas of Confocal Laser Scanning In-vivo Microscopy in Ophthalmology* (Springer-Verlag Berlin Heidelberg, 2006), Chap. 2.
24. A. Zhivov, O. Stachs, J. Stave, and R. F. Guthoff, "In vivo three-dimensional confocal laser scanning microscopy of corneal surface and epithelium," Br. J. Ophthalmol. **93**(5), 667–672 (2009).
25. W. M. Petroll, H. D. Cavanagh, and J. V. Jester, "Three-dimensional imaging of corneal cells using in vivo confocal microscopy," J. Microsc. **170**(3), 213–219 (1993).
26. N. S. Lagali, S. Allgeier, P. Guimarães, R. A. Badian, A. Ruggeri, B. Köhler, T. P. Utheim, B. Peebo, M. Peterson, L. B. Dahlin, and O. Rolandsson, "Wide-field corneal subbasal nerve plexus mosaics in age-controlled healthy and type 2 diabetes populations," Sci. Data (to be published).
27. K. Bizheva, B. Tan, B. MacLelan, O. Kralj, M. Hajialamdari, D. Hileeto, and L. Sorbara, "Sub-micrometer axial resolution OCT for in-vivo imaging of the cellular structure of healthy and keratoconic human corneas," Biomed. Opt. Express **8**(2), 800–812 (2017).
28. R. F. Guthoff, H. Wienss, C. Hahnel, and A. Wree, "Epithelial Innervation of Human Cornea: A Three-Dimensional Study Using Confocal Laser Scanning Fluorescence Microscopy," Cornea **24**(5), 608–613 (2005).
29. S. Allgeier, Institute for Automation and Applied Informatics, Karlsruhe Institute of Technology (KIT), Hermann-von-Helmholtz-Platz 1, D-76344 Eggenstein-Leopoldshafen, Germany, A. Bartschat, S. Bohn, K.-M. Reichert, K. Sperlich, M. Walckling, V. Hagenmeyer, R. Mikut, O. Stachs, and B. Köhler are preparing a manuscript to be called "3D confocal laser-scanning microscopy for large-area imaging of the corneal subbasal nerve plexus."
30. A. Bartschat, L. Toso, J. Stegmaier, A. Kuijper, R. Mikut, B. Köhler, and S. Allgeier, "Automatic corneal tissue classification using bag-of-visual-words approaches," in *Forum Bildverarbeitung 2016*, F. Puente León and M. Heitzmann, eds. (KIT Scientific Publishing, 2016), pp. 245–256.

1. Introduction

Presently, a well-established method for acquiring corneal images at cellular level is the combination of the Heidelberg Retina Tomograph (HRT) and the Rostock Cornea Module (RCM; both Heidelberg Engineering GmbH, Heidelberg, Germany), which is a confocal laser scanning microscope. Since its first presentation in 2002 [1], the HRT + RCM serves as a reliable instrument [2] and plays an important role in *ex vivo* and *in vivo* studies of human or animal corneas for a qualitative and quantitative analysis based on 2D imaging and/or 3D image reconstruction, e.g. the anatomical comparison of laboratory animal corneas [3], the assessment of stromal modifications of patients with progressive keratoconus after treatment by riboflavin-UVA-induced cross-linking of corneal collagen [4], quantitative full-thickness corneal 3D imaging [5], automated quantification of morphologic features of different epithelial cell layers [6], 2D reconstruction of the subbasal nerve plexus (SNP) from volume

scans in the presence of ridge-like tissue deformations [7] and large-scale image reconstruction of the SNP [8–13].

Besides confocal laser scanning microscopy based methods, the full-field optical coherence tomography (FF-OCT) [14] is a promising attempt to obtain *en face* corneal images. Recently, FF-OCT was demonstrated to offer *in vivo* human corneal images with 1.7 μm lateral resolution and 1.26 mm x 1.26 mm field of view in a non-contact measurement [15]. Nevertheless, confocal laser scanning microscopy still offers higher lateral resolution and better image quality.

Several corneal 3D reconstructions from confocal light and confocal laser scanning microscopy image stacks are published already. Image stacks through the entire cornea are presented in [16] and were acquired with a tandem scanning confocal light microscope and without image alignment, leading to lower image quality and lower resolution compared to confocal laser scanning based methods. In [7,17,18], volume imaging with a confocal laser scanning microscope (HRT + RCM) was described. The internal focus drive of the HRT was used, which allows the recording of corneal stacks with a maximum depth of only 60 μm. The full thickness corneal stacks presented in [5] were performed on a sedated rabbit to avoid eye movements. The RCM's manual drive for focal plane control was replaced with a computer-controlled motor drive. One of the biggest flaws of this method and the RCM in general is the axial movement of the contact cap (TomoCap) for focal plane control, which inevitably changes the contact pressure on the cornea. From our experience, two major issues arise therefrom. First, the movement of the TomoCap away from the cornea during through-focusing can ultimately lead to a loss of contact. Second, when the TomoCap moves towards the cornea, the increasing applanation pressure on the cornea induces compression artifacts that manifest as ridge-like deformations in the SNP and the adjacent tissue [19–22]. These deformations are particularly detrimental for imaging thin layers such as the SNP, which cannot be kept in focus over the entire field of view once the deformation height exceeds the depth of field of the RCM.

In this study, we demonstrate our in-house developed piezo-driven cornea module (RCM 2.0), which is an improved version of the original RCM. (Please note: This RCM version is not commercially available and Heidelberg Engineering was not involved in its development. The authors do not hold any intellectual property on the device or design and are currently not planning to make it commercially available.) The integrated piezo actuator is used to move the objective lens for an axial focal plane shift of up to 500 μm without moving the TomoCap. This enables precise closed-loop focal plane control. We applied our new method to demonstrate *in vivo* through-focusing measurements and 3D reconstruction of a human cornea.

Furthermore, we present a new TomoCap with a concave surface to reduce involuntary eye movements (so-called saccades). The functional principle is based on the fact that the eyeball's center of rotation differs from the cornea's center of curvature and on the usage of a viscous contact gel. Reduced lateral eye movements result in larger fields of view of the aligned image stack. The achieved improvements, arising from the new cap design, were assessed by analyzing comparative measurements using the standard planar and the new concave TomoCap design. Additionally, we compared three image registration methods (none, rigid, non-rigid) for the alignment of the image stacks. Orthogonal as well as oblique slices through a volume data set recorded with the concave TomoCap are presented to exemplify the capabilities of the modified RCM.

2. Materials and methods

2.1 Heidelberg Retina Tomograph and Rostock Cornea Module 2.0

The HRT is a confocal laser scanning microscope primarily designed to acquire *in vivo* retinal images. It offers an image resolution of 384 pixels x 384 pixels with 8 bit grayscale. The RCM is a detachable extension for the HRT incorporating an immersion objective to shift the

focal plane from the retina to the cornea while achieving cellular resolution [23]. Three exchangeable lenses exist to achieve a squared field of view with an edge length of 250 µm, 400 µm or 500 µm [23]. For hygienic reasons, a disposable contact element (TomoCap; Heidelberg Engineering) is used in contact with the cornea.
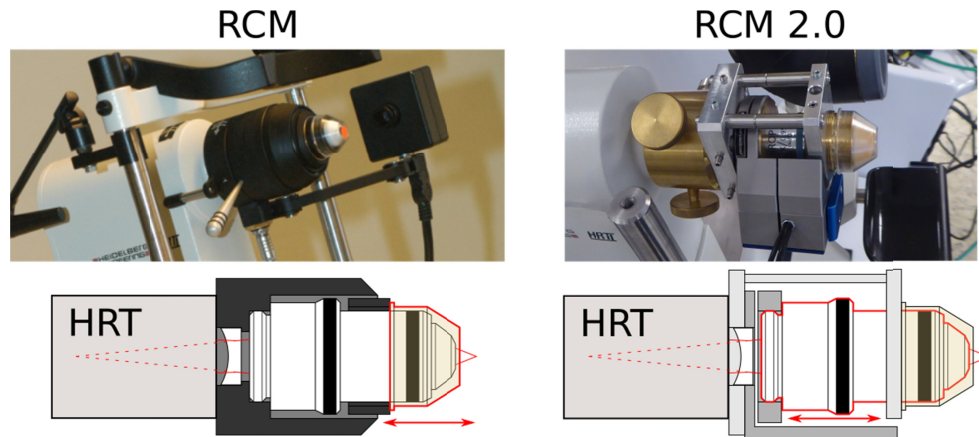

Fig. 1. Left: Original RCM – focal plane adjustment by TomoCap movement (outlined in red). Right: RCM 2.0 – focal plane adjustment by objective lens movement (outlined in red), while TomoCap position remains fixed. Please note: The different TomoCaps are compatible to both RCM versions and only the planar TomoCap is shown here. The concave TomoCap is presented in Fig. 2.

Figure 1 depicts the original and the new RCM 2.0 in the upper row and further demonstrates the modified function principle. Both modules are based on the same optical components. The plano-concave lens between HRT and objective lens is interchangeable to allow different fields of view. To realize the required high resolution, the RCM is equipped with a water immersion objective (Achroplan 63x/0.95 W; Zeiss, Jena, Germany) and hence immersion gel on either side of the TomoCap is necessary. It is also essential for the elimination of surface reflections from the cornea and the TomoCap. In order to change the focal plane within the cornea, the original RCM moves the TomoCap using a manual drive or in a modified version an electrical motor drive [5], whereas our new RCM 2.0 utilizes a closed-loop piezo system (MIPOS 600 SG OEM; piezosystem jena GmbH, Jena, Germany) with 500 µm travel range (600 µm open-loop) to move the objective lens inside the module while the TomoCap position remains fixed. Therefore, the contact pressure on the cornea is not changed by moving the focus drive. However, the contact pressure may still be influenced by the subject (eye or head movements, breathing, heartbeat, et cetera).

Due to slightly different positions of the optical components, the RCM 2.0 has a smaller field of view of about 350 x 350 µm^2 instead of 400 x 400 µm^2 compared to the original RCM with the equivalent plano-concave lens. Since the single laser beams are not parallel when entering the objective lens, axial objective lens movements change the magnification. However, as we will show in the results section, this effect is marginal and can be neglected.

2.2 TomoCap

The standard TomoCap with a planar contact surface has been previously investigated with different surfaces modifications, for e.g. the attachment of an additional thin PMMA plain washer to prevent applanation artifacts [24]. Here we present a modified TomoCap featuring a concave surface with a diameter of 12 mm and curvature radius of (7.8 ± 0.5) mm, according to the curvature of an average human cornea. This TomoCap is in-house manufactured by cutting the concave part from a contact lens (Three-mirror single-use contact lens; SMT, Maple Valley, WA), polishing the cutting surface, and gluing it onto a modified

TomoCap with the planar surface being removed. This way the new TomoCap can also be used with the standard RCM. Figure 2 shows the standard TomoCap with the planar surface and the new design with the concave surface. The goal of the new TomoCap is to avoid cornea deformation or compression artifacts and to reduce involuntary eye movements in order to obtain a larger lateral area with overlapping images throughout the whole stack. The image alignment procedures for 3D reconstruction may also potentially benefit from the reduced eye movements.
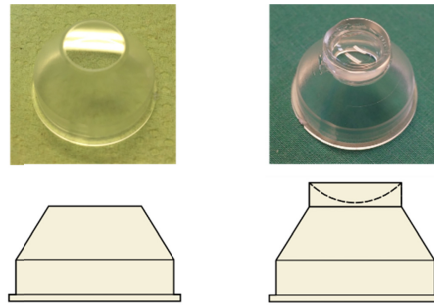
Fig. 2. TomoCap with planar (left) and concave (right) contact surface.

The functional principle is to approximately match the contact surface of the new TomoCap with the cornea surface offering a form closure. Since the center of rotation of the eye lies behind the center of the cornea curvature, a slight change in viewing direction mainly changes the lateral position of the cornea. In that case, lateral eye movements are confined by the form closure. The amount of possible movement depends on the thickness of the contact gel between cornea and TomoCap and the individual curvature of the examined cornea. Figure 3 shows the anterior section of an eye and a concave TomoCap both symmetrically aligned. Vertical lines mark the cornea apex and center of the concave surface. The thickness of the contact gel is 50 µm in the illustrated example. In that case, the eye's movement is confined to about 160 µm, neglecting a potential cornea deformation. It is also restrained by the viscous gel. It stabilizes in axial direction because work is necessary to press gel out of the volume between cornea and TomoCap or to suck in surrounding gel. This effect is known for gonioscopy lenses and in that context generally referred to as suction. The gel is also responsible for laterally restrained eye movements. The effect is basically the same, but now the gel is pressed out on the one side and sucked in on the opposite side. This is depicted in the right side of Fig. 3. The eye was rotated clockwise around the eyeball's center of rotation (cr), such that a lateral movement of the cornea of 150 µm is induced. The vertical lines on the cornea apex and center of the concave surface visualize the rotation and the induced lateral shift. The two inserts show magnified views of the limbal region with the amount of surrounding gel schematically depicted. The distance between cornea and TomoCap is now different on both sides. On the left side the distance is increased with less surrounding gel and on the right side it is decreased with more surrounding gel. Additionally, the increased contact surface leads to decreased shearing induced by the lateral forces of saccades.
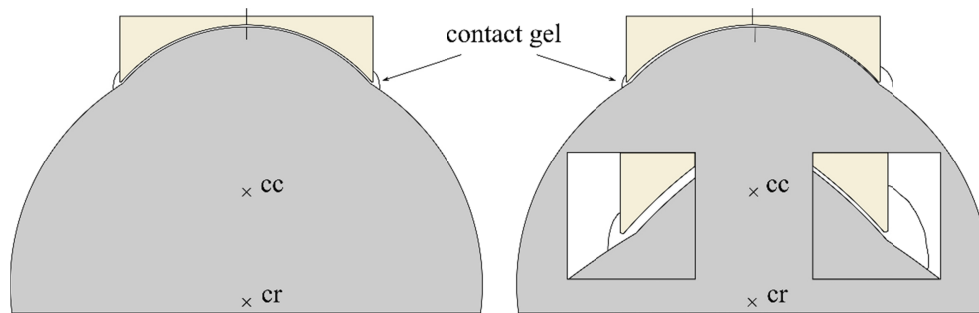
Fig. 3. True to scale sections of eyeball, cornea and concave TomoCap with a gel interface of 50 μm thickness. The cornea's center of curvature is denoted with cc and the eye's center of rotation with cr. Vertical lines on the cornea apex and center of the concave surface visualize the rotation of the eye. Left: no rotation; Right: Clockwise rotation around cr of 0.66 ° corresponding to a lateral corneal shift of 150 μm. Insets show the distance between cornea and TomoCap and schematically the amount of surrounding gel.

The idea of a concave contact surface for microscopy is not new. For instance, a concave applanating tip objective (7.5 mm radius of curvature) was published 25 years ago [25]. Unfortunately, the diameter of the contact surface is not specified, but it seems to be quite small. Therefore, we suppose this contact surface had no restraining effect on lateral eye movements.

2.3 Data acquisition, image alignment procedures, and stack quality parameters

To evaluate the RCM 2.0 and quantify the influences of the concave TomoCap, we acquired several cornea stacks (30 frames per second, automatic brightness control activated in HRT settings) for each TomoCap design from three healthy human volunteers. One of these data sets is visualized to demonstrate the possibility of thick corneal cuboid image stacks. All stacks were acquired with a constant scan velocity of 15 μm/s.

One image stack intended for isotropic volume reconstruction of the anterior cornea was acquired using the concave TomoCap and a focus drive velocity of 30 μm/s, resulting in an axial distance of 1 μm between two images. The axial image distance of 1 μm results in a voxel size of 0.91 x 0.91 x 1 μm^3. To obtain an isotropic reconstructed volume, all images were scaled accordingly to get a voxel size of 1 x 1 x 1 μm^3. However, the depth of focus of the RCM is reported to be about 8 μm [2,23]. Therefore, structures from one image are visible in the adjacent images. The reconstructed stack starts from the superficial cells of the epithelium and ends 187 μm deeper in the stroma.

Because of the differing specific reflectance, several images were under- or overexposed. Therefore in a post-processing step, the histogram of every image was scaled to the full 8 bit range excluding overexposed pixels.

Third-party software, ImageJ and Amira 3D, was used for 3D volume reconstruction of image stacks and for the imaging of sectional views. To align each image relative to the next one, we used both a rigid image registration method from Amira 3D and a specially adapted image registration algorithm developed by the Karlsruhe Institute of Technology (KIT) [7], which we term in the following as KIT-alignment. The registration method from Amira 3D uses rigid transformations (translations and rotations) to align consecutive images. In contrast, the KIT-alignment is tailored to the image generation process of the HRT and not restricted to rigid transformations. It is derived from the scanning pattern of the HRT, which scans the field of view in horizontal lines. Scanning a single horizontal scan line (i.e. image row) takes approximately 65 μs [7]. Any eye motion happening on that time scale is assumed to be negligible with regard to causing motion artifacts in the image data, hence image rows are defined as rigid units. The basic principle of the alignment algorithm is to establish the correct location for each image row of the acquired corneal confocal microscopy data set. This can be

achieved by finding corresponding regions in image pairs of the recorded data set, as further detailed in [26]. This alignment technique allows the correct reversal of the characteristic motion artifacts that are induced by spontaneous eye movements, head movements or external mechanical vibrations (e.g. traffic or footsteps nearby) transferred to the HRT and that manifest as specific, non-linear distortion effects in the image data.

The TomoCap position can still be adjusted relative to the objective lens by rotating the TomoCap holder. Hence this method is not limited to the anterior part of the cornea. The stack thickness is in principle only limited by the traveling range of the piezo stage, the thickness of the gel film on the TomoCap and the preset position of the TomoCap.

After aligning all stacks of the three subjects with both TomoCaps using the KIT-alignment, we calculated the two following parameters. The first one is the mean lateral image-to-image shift of two consecutive images (MS_p for planar and MS_c for concave TomoCap), by taking the center of gravity of a registered image as a reference point. This parameter indicates the magnitude of eye movements during image acquisition. Since not all stacks could be registered entirely, we used only shift values from multiple substacks with at least ten successfully aligned consecutive images to calculate this parameter. For all combinations of subject and TomoCap the same sample size (total number of shift values) of $n = 1000$ was used.

The first parameter is not sufficient to quantify the quality of a reconstructed stack. One can easily imagine an image sequence with small image-to-image shifts, but with a distinct shift direction. With increasing number of images n_{im}, the overlapping area of the total stack decreases. Therefore, the mean approximated overlapping area (MA_p for planar and MA_c for concave TomoCap) was calculated for all data sets as a second parameter. To calculate the approximated overlapping area A of a single stack (see Fig. 4), the coordinates of the centers of gravity for the shifted single images were calculated in both lateral directions. From these values, the maximum and minimum coordinates in both directions (x_{max}, x_{min}, y_{max} and y_{min}) related to the entire stack were determined. The distances between maximum and minimum coordinates were then subtracted from the respecting side length s of a single image to calculate the approximated area:

$$A = (s - (x_{max} - x_{min})) \cdot (s - (y_{max} - y_{min})). \tag{1}$$

For calculation purposes the single images are assumed to be undistorted squares, thus the area A is approximated. Figure 4 illustrates the calculation of A.
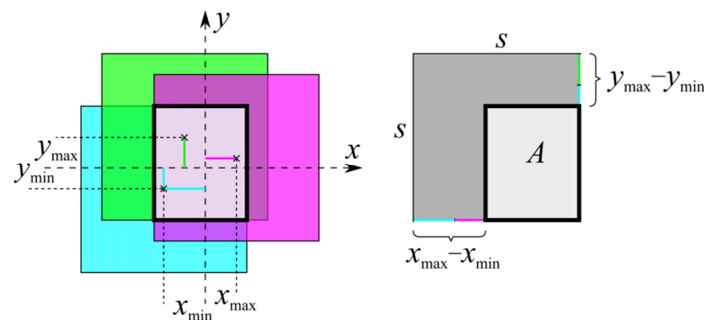

Fig. 4. Illustration for the calculation of the approximated overlapping area A (boldly outlined area). Colored lines represent the maximum and minimum coordinate of the stack. The $\times$ - symbols mark the center of gravity of the single images with a side length s. For the sake of simplicity, the calculation is demonstrated on a strongly reduced stack with only three images.

For the calculation of the mean approximated overlapping area of several stacks, the size of the individual stacks was reduced to have a common n_{im} per stack. Stacks with a multiple of n_{im} were divided into new stacks to get a larger number of stacks n_{st}. This way, n_{st} is guaranteed to be at least 40 to ensure statistical robustness.

To verify the different performance of the planar and the concave TomoCap, the error probability p for each parameter and subject was estimated using Welch's t-test. We also investigate the capability of the concave TomoCap regarding MA for stacks with large n_{im}.

3. Results

As mentioned in the method section, the magnification changes with objective lens position. Therefore, an object micrometer was imaged for various objective lens positions. The total field of view was ranging linearly from about 349 µm to 351 µm in the total closed-loop travel range of 500 µm. Hence this effect can usually be neglected.

Using the standard TomoCap, involuntary eye movements can cause the cornea to move more than the width of the field of view within the exposure time of a single frame [10]. In this case consecutive images do not overlap and therefore cannot be aligned. In general, larger eye movements lead to smaller overlapping areas, thus impeding image alignment. Qualitative visual inspection of the image streams reveals a significant reduction of lateral eye movements in the data sets recorded with the concave TomoCap. To demonstrate this issue, we included six supplementary videos showing aligned (KIT-alignment) image stacks in posterior scan direction of the three subjects with both TomoCaps (Visualization 1, Visualization 2, Visualization 3, Visualization 4, Visualization 5 and Visualization 6). Table 1 shows the determined parameters MS_p and MS_c including the standard error for the three subjects. The mean approximated overlapping area MA_p and MA_c are listed in Table 2 for $n_{st} = 40$ and the specified n_{im}. Furthermore, Table 3 gives MA_c for increasing n_{im}. For comparison, the area of a single image is 0.1219 mm².

Table 1. Comparison between TomoCaps regarding lateral image-to-image shifts.

Subject	MS_p / µm	MS_c / µm	p
1	18.8 ± 0.4	2.40 ± 0.14	< 0.0001
2	6.74 ± 0.19	1.34 ± 0.09	< 0.0001
3	15.0 ± 0.9	4.48 ± 0.14	< 0.0001

Table 2. Comparison between TomoCaps regarding overlapping area for $n_{st} = 40$.

Subject	MA_p / mm²	MA_c / mm²	p	n_{im}
1	0.0487 ± 0.0004	0.10723 ± 0.00020	< 0.0001	32
2	0.0700 ± 0.0007	0.11010 ± 0.00020	< 0.0001	45
3	0.0583 ± 0.0007	0.10553 ± 0.00015	< 0.0001	21

Table 3. Overlapping areas using the concave TomoCap with increasing stack sizes.

Subject	n_{st}	n_{im}	MA_c / mm²
1	40	51	0.10087 ± 0.00025
	20	98	0.10723 ± 0.00020
	10	175	0.0852 ± 0.0010
	5	294	0.0731 ± 0.0010
2	40	87	0.10569 ± 0.00024
	20	158	0.0995 ± 0.0007
	10	264	0.0943 ± 0.0014
	5	409	0.073 ± 0.004
3	40	71	0.09412 ± 0.00017
	20	139	0.0965 ± 0.0004
	10	248	0.0742 ± 0.0007
	5	497	0.0558 ± 0.0014

Comparing the parameters of both TomoCaps from Table 1, we find a reduction of 87%, 80% and 70% of the eye movements between consecutive images using the concave TomoCap for Subject 1, 2 and 3 respectively. Furthermore, Table 2 shows the mean approximated area of the stacks with the planar and the concave TomoCap. Without eye movements the stack's field of view would be the single image field of view. Eye movements induce a loss of overlapping area, which can be calculated by subtracting the mean approximated area from the single image area. Comparing the losses of overlapping area using the different TomoCaps we find the loss is reduced by 80%, 77% and 74% for Subject 1, 2 and 3 respectively using the concave TomoCap. Table 3 presents the mean approximated area for increasing stack size for the three subjects and the concave TomoCap. As expected, the mean approximated area decreases with the number of images in the stack. But compared to Table 2, we find that MA_c is reduced to MA_p only after a few hundred images instead of a few ten images with the planar cap. That means, stacks with a high thickness particularly benefit from the concave TomoCap. Furthermore, with the concave TomoCap we achieved generally multiple times thicker stacks after the alignment compared to the planar TomoCap. This is due to involuntarily and sporadically occurring saccadic eye movements with an amplitude in the order of the side length of the FOV. They effectively prevent successful image alignment when the planar TomoCap is used but are practically absent (or occur with greatly limited amplitude) from data sets acquired with the concave TomoCap.

To compare the different alignment methods, Fig. 5 shows false color composites derived from two consecutive stromal images of the acquired corneal stack without alignment (Fig. 5(A)), with rigid alignment (Fig. 5(B)) and with KIT-alignment (Fig. 5(C)). These false color images can be easily calculated by setting the grayscale intensity values of one image as red and blue channel, and the grayscale intensity of the next image as green channel of a colored image. Regions without any change or in other words with same intensity are displayed in grayscale, while regions with intensity only in the first or second image are colored in magenta or green, respectively. This way, changes from one image to the next one are obvious. Despite a proper image alignment, compare Fig. 5(C), we observed spots with non-gray values resulting from noise or regions with different brightness possibly due to a structural change in axial scanning direction. However, these false color composites emphasize the misaligned regions and seem to be an intuitive representation for the comparison between alignment methods.
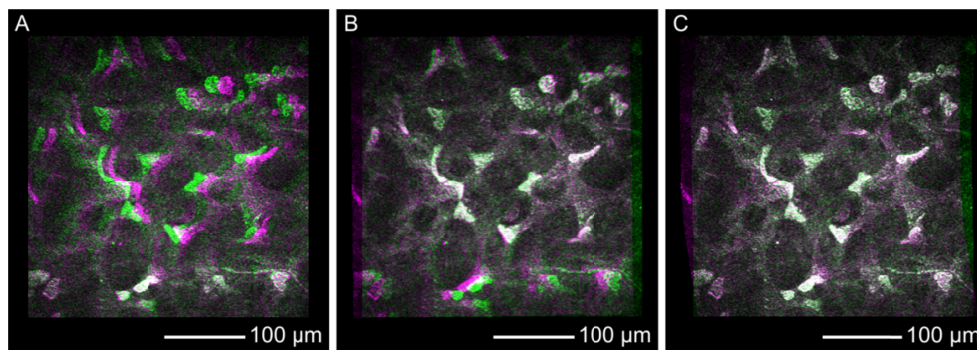

Fig. 5. False color composite images derived from two single consecutive stromal images recorded with the concave TomoCap and using no alignment (A), rigid alignment (B) and KIT-alignment (C). Regions with identical intensity distribution in the first and second image are rendered in grayscales while differences are colored either magenta or green (see text for detailed explanation).

The example without any image alignment, shown in Fig. 5(A), seems to match quite well in the lower part, while the upper and middle regions exhibit a certain amount of green and magenta regions indicating eye movement from the right to the left in the order of 20 µm. The

rigid alignment (Fig. 5(B)) shows good agreement in the upper and middle part of the images, but it reveals a worse alignment in the lower part due to non-linear motion distortions. We conclude that a translation and rotation of the whole image is insufficient to correct the motion induced distortions. The best alignment was achieved using the KIT-alignment (Fig. 5(C)), which corrects the motion induced distortions row-wise, leading to non-square images as seen in Fig. 5(C).

Applying the KIT-alignment to a whole stack allows a volume reconstruction and hence image slice in arbitrary directions with a high image quality as seen in an orthogonal slice in Fig. 6(A). Axial scanning artifacts are not visible in this slice, because of the stabilizing effect in axial direction. To move the eye towards the contact cap, e.g. in case of heartbeat, the contact gel has to be pressed out of the volume between cornea and TomoCap and in the opposite direction the surrounding gel has to be sucked back into this volume. The force required for these processes is counteracting to the movement force of the eye and depends on the viscosity of the contact gel.
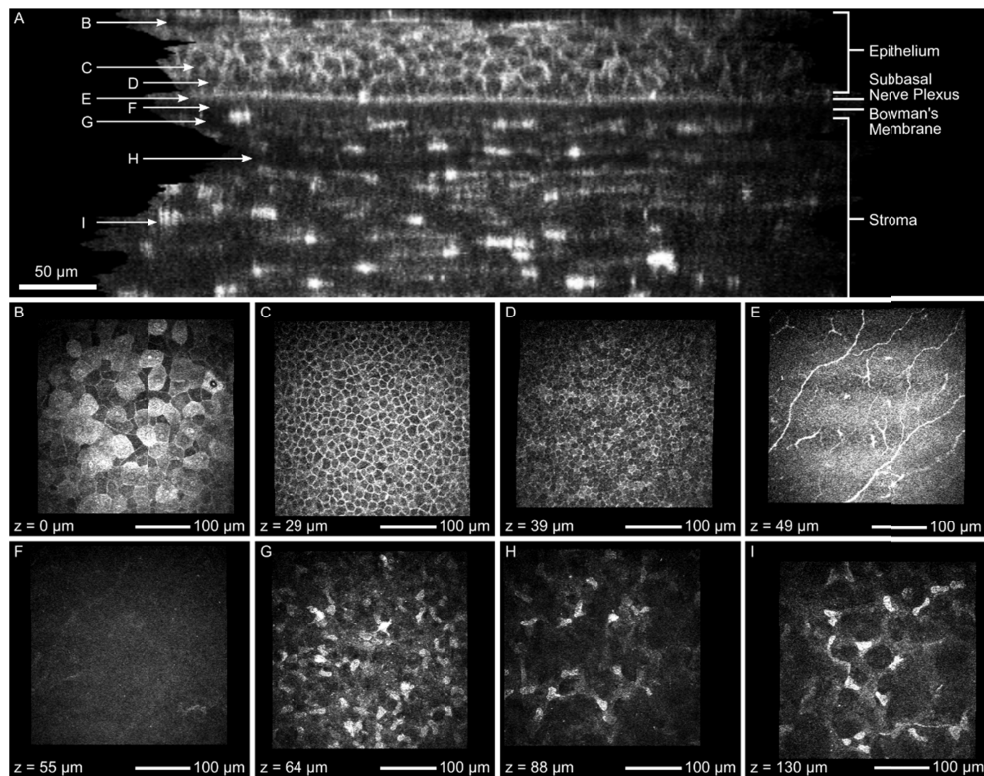
Fig. 6. Orthogonal slice (A) of the corneal image stack after KIT-alignment without image averaging over several slices and exemplary images from different layers: superficial cells (B), intermediate wing cells (C), basal epithelial cells (D), subbasal nerve plexus (E), Bowman's membrane (F) and stroma (G, H, I). This image stack was recorded using the concave TomoCap.

It is also possible to measure axial sizes of corneal structures. In [27] a sub-micrometer axial resolution OCT is used to measure the epithelial and Bowman's membrane thicknesses and in [16] they are determined by an intensity profile of an image stack along the axial direction. The latter can be applied here as well or their sizes can be measured from the orthogonal slice directly. Depending on the measurement position in Fig. 6(A), we found that the epithelial and Bowman's membrane thickness were not perfectly constant and were determined to be 47 to 54 µm and 15 to 17 µm respectively. The axial epithelial cell diameter

can be measured as well, if the cell borders are visible. For ten randomly selected cells we found axial diameters between 10 to 15 µm. Due to the depth of focus being in the order of 8 µm it is not possible to reliably measure the axial size of small structures such as keratocyte nuclei.

Additionally to Fig. 6(A), the specific *en-face* images of each layer ranging from the superficial cells to the stroma are presented in Fig. 6(B) to 6(I), respectively. The corresponding imaging depth is added in the bottom left corner.

The superficial cells (Fig. 6(B)) are flat, overlapping polygonal cells identified at the surface of the corneal epithelium at the depth of 0 µm. The cell borders appear clear with dark nucleus. The cytoplasm of the cells is readily visible where few cells demonstrate highly reflective cytoplasm with bright nucleus and its dark perinuclear space indicates process of cell desquamation. The superficial cells appear significantly larger than the intermediate and basal cells. Figure 6(C) demonstrates the intermediate wing cell layer at the depth of 29 µm. These cells appear more uniform and compact with bright and well-defined cell borders and dark cytoplasm. However, the cell nucleus is hardly visible. Basal epithelial cells (Fig. 6(D)) are visible as tightly packed smallest cells immediately above Bowman's membrane. These cells have bright and clear cell borders with inhomogeneous reflectivity of cytoplasm between cells and are more uniform in shape and size similar to wing cells with uncertain cell nucleus. The SNP (Fig. 6(E)) is clearly imaged a few microns above the Bowman's membrane. We were able to detect typical Y-shaped, thick and highly reflective nerve fibers running parallel to each other. We could also identify small highly reflective Langerhans cells with fine dendritic processes. An acellular Bowman's layer (Fig. 6(F)), also called the anterior limiting membrane, situated between the stroma and the cellular epithelium, could be distinguished at the level of 55 µm. Anterior stroma (Fig. 6(G)) is imaged at around 64 µm close to Bowman's membrane. This layer reveals multiple, small and highly reflective keratocyte nuclei. The lamellar collagen fibers in-between cells are not visible. The density of these nuclei seems to be significantly higher close to Bowman's membrane and gradually decreasing towards central stroma (Fig. 6(H), 6(I)).

In Fig. 5, the alignment quality of the single confocal images was compared. Following, the impact of the different alignment methods on generating orthogonal slices will be analyzed (see Fig. 7).
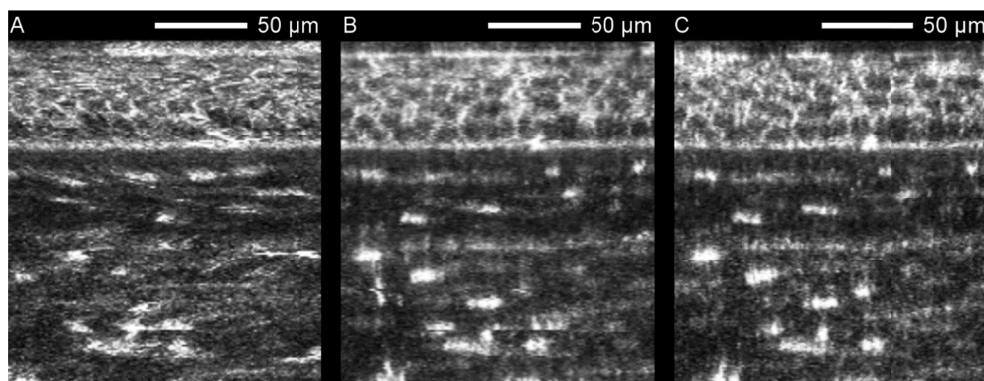

Fig. 7. Orthogonal slices of a corneal image stack captured with the concave TomoCap using no alignment (A), rigid alignment (B) and the KIT-alignment (C). Without alignment, epithelial cells cannot be resolved. Notice the increasing image quality from Fig. 7A to 7C. Image averaging was not performed.

The image distortions in the *en face* images induced by ocular movements are clearly demonstrated in orthogonal slices as in Fig. 7(A) where the cell layers appear wavy. Hence, it is difficult or impossible to distinguish single cells. In contrast, Fig. 7(B) and 7(C) show clear appearances of epithelial cell bodies and stroma keratocyte nuclei. Nevertheless Fig. 7(B) still

exhibits some artifacts, e.g. horizontally shifted single lines in the lower region that cannot be compensated by the rigid alignment. Furthermore, Fig. 7(B) appears to be more blurry than Fig. 7(C). This is due to the type of interpolation required for the rotation of the rigid alignment. All three *en face* image stacks used for Fig. 7 are attached as supplementary video (Visualization 7, Visualization 8 and Visualization 9) emphasizing the lateral movements.

In Fig. 8, a comparison between a schematic drawing according to Guthoff et al. [28] (Fig. 8(A)) and three analogous variants of the reconstructed corneal image stack in isometric view is shown. These three variants were reconstructed by using no alignment (Fig. 8(B)), rigid alignment (Fig. 8(C)) and KIT-alignment (Fig. 8(D)) again. After aligning the corneal image stack, it was cropped in order to achieve a cuboid volume. Hence the field of view is decreased from 350 µm x 350 µm (0.123 mm^2) to 273 µm x 302 µm (0.083 mm^2) and 271 µm x 292 µm (0.079 mm^2) for rigid alignment and KIT-alignment respectively. Compared to Table 3, the field of view reduction depends on the stack depth, but also on the subject itself. For visualization purposes, the different layers are presented in stacked boxes with increasing lateral size from top to bottom and orange highlighted edges. The topmost box shows a section of the anterior epithelium with its superficial cells on top, the middle box shows the remaining epithelium starting at the intermediate wing cells, and the last one contains the subbasal nerve plexus on top and stroma containing the keratocyte nuclei on the side. While the structures on the sides of the stack in Fig. 8(B) are distorted, the sides in Fig. 8(C) and 8(D) reveal cellular structures, especially in the epithelial layer. In this kind of presentation, the differences between the rigid alignment and KIT-alignment are less noticeable compared to Fig. 7.
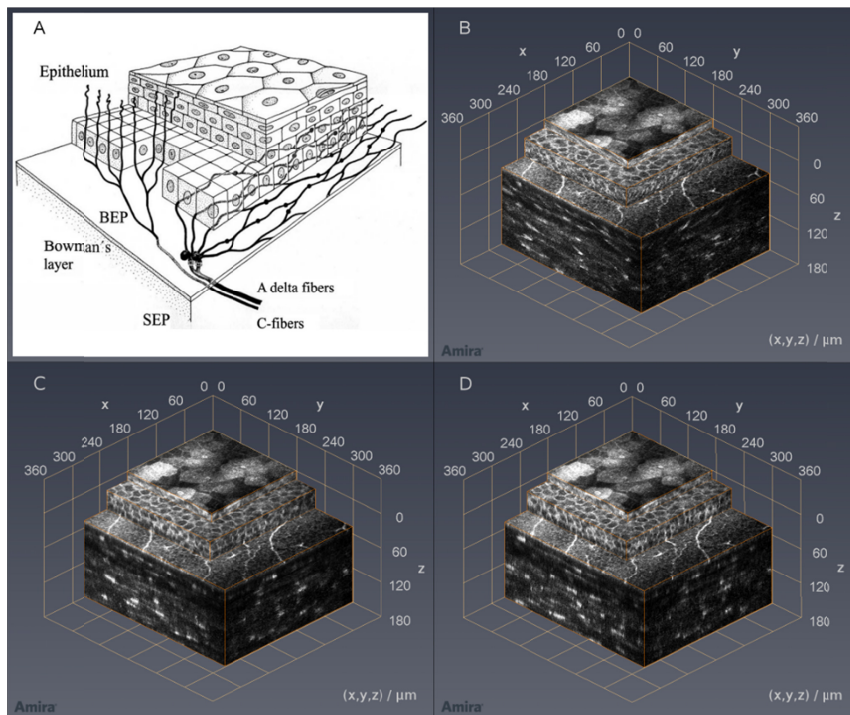

Fig. 8. Cornea sketch according to Guthoff et al. [28] (A); corneal image stack recorded with the concave TomoCap in isometric view using no alignment (B), rigid alignment (C) and KIT-alignment (D). Please note: The top surfaces in these images are, based on the imaging method, almost identical. However, the side views of (C) and (D) reveal epithelial cells whereas the stroma shows the keratocyte nuclei. Due to the different alignment methods, structures may be imaged at slightly changed positions thus leading to altered cross-sections. Image averaging was not performed.

With proper alignment, it is also possible to create oblique slices through the corneal image stack, as shown in Fig. 9. Due to no alignment in Fig. 9(A), there are distortions and artifacts that are significantly reduced by rigid alignment (Fig. 9(B)) and KIT-alignment (Fig. 9(C)).
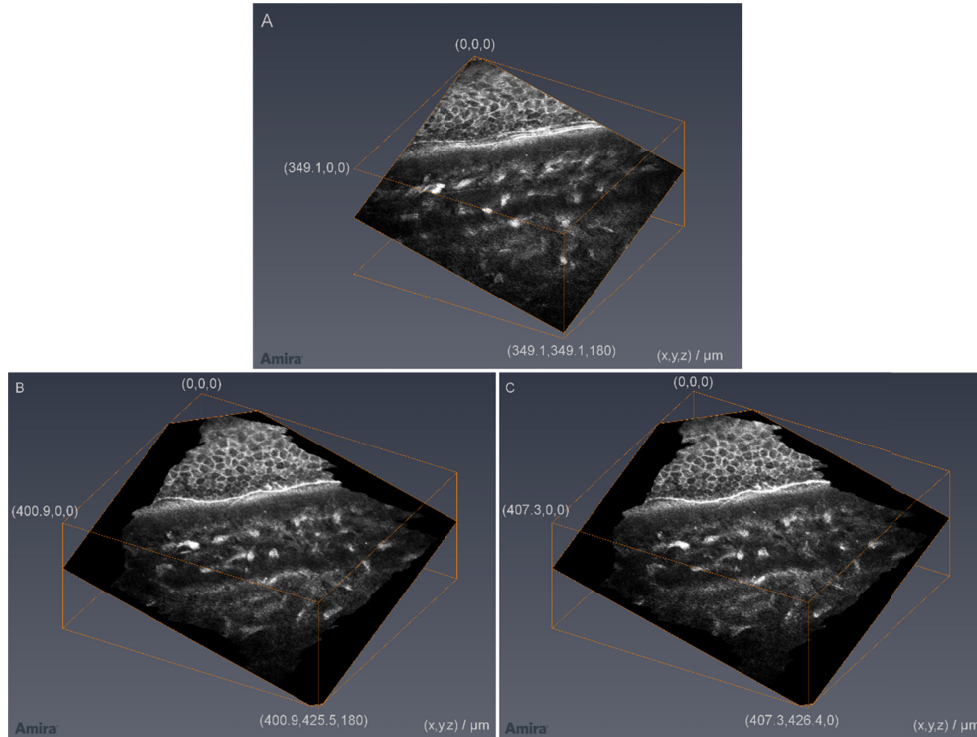

Fig. 9. Oblique slices of a corneal image stack captured with the concave TomoCap using no alignment (A), rigid alignment (B) and KIT-alignment (C). Notice: In order to keep all information of the slice, the imaging area in B and C is increasing. Image averaging was not performed.

An example for a KIT-aligned thick corneal image stack is presented in Fig. 10. The cropped field of view of the complete stack is 266 x 286 μm^2 and the thickness is 396 μm. Generally, corneal image stacks with up to 500 μm are possible using this setup. The axial scan velocity was 15 $\mu m/s$ resulting in an acquisition time of 26.4 s. Compared to the stack in Fig. 8, the image quality was not increased by a half scan speed. So a reasonable acquisition time for a thick image stack is in the order of 13 s using the presented setup.
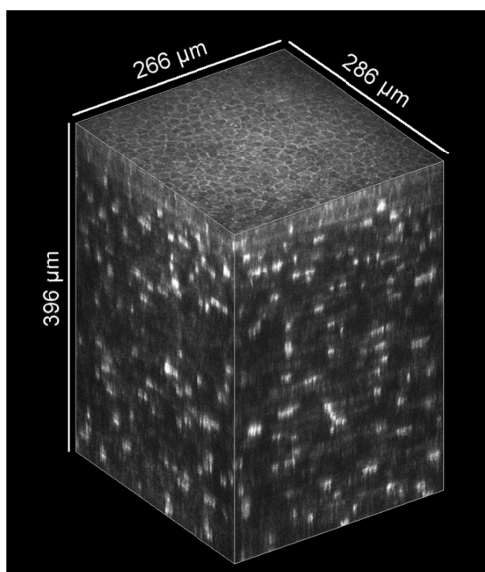
Fig. 10. Exemplary thick KIT-aligned 3D corneal image stack, originally used for the analysis of the eye movements with the concave TomoCap. It starts close to the subbasal nerve plexus and has a depth of 396 μm. (HRT automatic brightness control is deactivated and no image processing was performed)

4. Discussion and conclusions

The in-house developed RCM 2.0 in combination with the concave TomoCap performed well for *in vivo* corneal 3D imaging. An important, general advantage of the RCM 2.0 is the static TomoCap, reducing compression artifacts and the risk of contact loss between eye and TomoCap in e.g. through-focusing scenarios. Furthermore, in our measurements we experienced that the risk of contact loss is even smaller using the concave TomoCap compared to the planar one, which we believe is due to increased adhesion forces or the capillary effect caused by matched contact surfaces. In comparison to the planar TomoCap and depending on the investigated subject, a reduction of 70-87% in eye movements between consecutive images was achieved. Additionally, depending on the stack depth, the overlapping area loss was reduced by 74-80%, hence resulting in a larger cuboid volume. The listed data in Tables 1-3 prove the better eye fixation of the concave TomoCap. This is caused by the fact that the cornea's center of curvature differs from the eyeball's center of rotation and therefore the eye movements are limited. The reduction of eye movements is also due to the suction effects of the viscous contact gel as explained in detail in section 2.2.

In any case, cropping an aligned stack reduces its field of view. The reduction depends on the stack thickness and the subject. An increased field of view can be achieved by another lens inside the RCM. However, cells would appear smaller with a worse resolution. For a larger field of view with the same or even better resolution, another device with a higher sampling frequency of the detector and thus a higher image resolution than the HRT should be chosen.

Image alignment is an important step in the 3D reconstruction of axial image stacks and slices. Unaligned stacks have a number of distortions preventing analyzable orthogonal slices. The concave TomoCap with its better fixation of the cornea reduced the movement distortions in every single image. This simplified the image alignment procedures and moreover the image quality after rigid alignment is enhanced being closer to the KIT-alignment as shown in the orthogonal and oblique slices (Fig. 7 and 9) and especially in volume presentations as in Fig. 8. Even without sophisticated software routines, like the KIT-

alignment, analyzable volume reconstructions can be achieved using the concave TomoCap and the new RCM 2.0. Despite that, Fig. 5 and Fig. 7 prove that the best image quality is realized with the KIT-alignment, which is tailored to the HRT.

Compared to the planar TomoCap, the image data acquired with the concave TomoCap have the same high image quality throughout all our measurements while simultaneously reducing eye movements significantly. Although expanded *in vivo* human corneal image stacks and arbitrary slices were presented before [16–18], the image quality of the slices is now increased by the interplay of the piezo drive, the concave TomoCap and the KIT-algorithm.

With the wide range of scanning parameters like velocity and travel distance as well as various scanning functions, the RCM 2.0 is suitable for numerous tasks. Furthermore, the maximum focus shift is increased to 500 μm and the position control is more precise while at the same time offering higher resolution and acceleration compared to the motorized RCM described in [5]. This enables a fast focal plane change with more than 800 μm/s while offering a position feedback with 12 nm accuracy. Additionally, the piezo system in combination with the fixed TomoCap provides new opportunities, for example a fast oscillating focal plane for large-scale image reconstruction of the SNP [29]. This is an elegant way to get rid of gaps and foreign tissue in large area imaging of the SNP [29,30], caused by unwanted axial shifts of this layer during examination. Without the fast oscillating focal plane shift, the focus has to be adjusted manually during image recording.

Despite the advantages of the concave TomoCap presented in this work, the usage of this cap is only recommended for investigations where the eye is supposed to remain fixed. For other tasks, e.g. mapping structures by the use of guided eye movements [13], the planar TomoCap is still the best choice. It is also not recommended to investigate the limbal region with such a concave TomoCap. Another drawback of the new TomoCap is its size. Often a camera is used to observe the reflection of the laser spot on the cornea for prealignment before contacting the cornea. This is only possible for large distances between cornea and the concave TomoCap, because otherwise the line of sight is blocked. However, a part of the scanning laser light is visible on the iris. This light can be exploited for a rough alignment. A multimodal imaging method combining confocal laser scanning microscopy and optical coherence tomography can also help in the alignment process. Sometimes the size of the TomoCap increases the setup effort. While examining subjects with a drooping eyelid, care has to be taken, that the eyelid is not between cornea and TomoCap.

Generally, the presented concave TomoCap and the RCM 2.0 enable fast and reliable recordings of expanded *in vivo* human corneal image stacks. Because of the reduced eye movements the cuboid volume of the 3D reconstruction is increased. Furthermore, whether a planar or concave TomoCap is used, the RCM 2.0 is preferable to the original RCM because of the computer controlled focus drive with a piezo actuator and the fixed TomoCap explained and demonstrated throughout this paper. The capability of the proposed method to create high-quality orthogonal or oblique slices through the corneal tissue presents the opportunity for *in vivo* slit lamp microscopy on a cellular level.

Funding

Acknowledgments

Disclosures

The authors declare that there are no conflicts of interest related to this article.

3D confocal laser-scanning microscopy for large-area imaging of the corneal subbasal nerve plexus

Stephan Allgeier, Andreas Bartschat, **Sebastian Bohn**, Klaus-Martin Reichert, Karsten Sperlich, Marcus Walckling, Ralf Mikut, Veit Hagenmeyer, Oliver Stachs, and Bernd Köhler

Copyright notice

SCIENTIFIC REPORTS

OPEN

3D confocal laser-scanning microscopy for large-area imaging of the corneal subbasal nerve plexus

Stephan Allgeier[1], Andreas Bartschat[1], Sebastian Bohn[2], Sabine Peschel[3], Klaus-Martin Reichert[1], Karsten Sperlich[2], Marcus Walckling[2], Veit Hagenmeyer[1], Ralf Mikut [1], Oliver Stachs[2] & Bernd Köhler[1]

The capability of corneal confocal microscopy (CCM) to acquire high-resolution *in vivo* images of the densely innervated human cornea has gained considerable interest in using this non-invasive technique as an objective diagnostic tool for staging peripheral neuropathies. Morphological alterations of the corneal subbasal nerve plexus (SNP) assessed by CCM have been shown to correlate well with the progression of neuropathic diseases and even predict future-incident neuropathy. Since the field of view of single CCM images is insufficient for reliable characterisation of nerve morphology, several image mosaicking techniques have been developed to facilitate the assessment of the SNP in large-area visualisations. Due to the limited depth of field of confocal microscopy, these approaches are highly sensitive to small deviations of the focus plane from the SNP layer. Our contribution proposes a new automated solution, combining guided eye movements for rapid expansion of the acquired SNP area and axial focus plane oscillations to guarantee complete imaging of the SNP. We present results of a feasibility study using the proposed setup to evaluate different oscillation settings. By comparing different image selection approaches, we show that automatic tissue classification algorithms are essential to create high-quality mosaic images from the acquired 3D datasets.

Diagnosis of peripheral neuropathies currently relies on assessments of nerve function that commonly detect pathologic alterations only after the manifestation of clinical symptoms. In this context, novel objective diagnostic methods with increased sensitivity are urgently needed to facilitate early diagnosis and to evaluate novel therapeutic approaches. Confocal laser scanning microscopy of the cornea is a promising novel approach which allows non-invasive *in vivo* imaging of the corneal subbasal nerve plexus (SNP) and therefore enables direct assessment of its morphology[1–3]. In recent years, corneal confocal microscopy (CCM) has been used to reveal significant morphological changes of the SNP in diverse diseases such as diabetic peripheral neuropathy (DPN), chronic migraine[4], multiple sclerosis[5,6] and familial amyloid neuropathy[7]. DPN in particular has been the main focus of various studies[8]. Since characteristic morphological alterations of the SNP already occur at an early stage of DPN[9,10], CCM has the potential to provide reliable biomarkers for the early assessment of DPN. A major limitation of this imaging technology arises from the inhomogeneous distribution of nerve fibres across the area of the cornea[11]. The field of view of a single CCM image (typically 0.16 mm²) is therefore insufficient for the reliable morphometric characterisation of the SNP. Recommendations in the literature to analyse samples of multiple non-overlapping CCM images to effectively expand the examined corneal area range from three[12] to eight[13] images, which have to be manually selected from a larger set of acquired images according to predefined quality criteria.

An alternative approach to increase the examined area is to compose a mosaic image from several overlapping CCM images. Various algorithms for the creation of mosaic images have been proposed[14–20]: Some rely on the operator to acquire appropriate image sequences manually, while others incorporate more automated methods for

[1]Institute for Automation and Applied Informatics, Karlsruhe Institute of Technology (KIT), Karlsruhe, Germany. [2]Department of Ophthalmology, Rostock University Medical Center, Rostock, Germany. [3]Augenarztpraxis Spremberg, Carl-Thiem-Klinikum-Poliklinik GmbH (MVZ), Cottbus, Germany. Correspondence and requests for materials should be addressed to S.A. (email: stephan.allgeier@kit.edu)
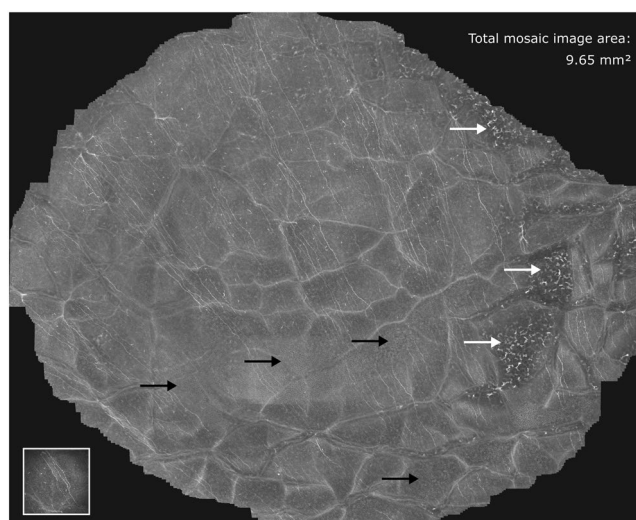
Figure 1. SNP mosaic image created using the EyeGuidance system without focus adjustments, as described by Allgeier *et al.*[21]. Several image areas show epithelium (black arrows) or stroma tissue (white arrows). The bottom left inset represents the size of a single CCM image ($0.4 \times 0.4\,mm^2$) from the recorded dataset.

capturing an extended area in the recorded image sequence. The so-called EyeGuidance system that we described in preceding articles[21,22] implements a fully automated image acquisition process. A computer-controlled fixation target, presented to the contralateral eye and moving in an outward-spiralling pattern, guides the eye movements of the patient during the entire image acquisition process. Using this approach, an average expansion rate of the acquired mosaic image area of $0.16\,mm^2/s$ can be achieved. Based on the examination of the progression of morphological SNP parameters in continuously expanding mosaic images, we recommended a minimum size of the mosaic images of $1.5\,mm^2$ for a reliable morphological characterisation of the SNP[23], which requires a mean examination time of less than 10 seconds[21] with the EyeGuidance system.

Due to the limited depth of field, which is characteristic to confocal microscopy, it cannot be guaranteed that all the recorded CCM images are well focused on the SNP layer. Even slight displacements perpendicular to the focus plane during the image acquisition process or small deviations from the surface-parallel arrangement of the SNP lead to images that partially or entirely contain extraneous tissue (epithelium or stroma)[21]. Consequently, the mosaic image generated from such an image sequence does not show SNP in the complete field of view (see Fig. 1), which ultimately leads to incorrect morphological SNP parameter measurements. This issue is also common to almost all of the previously proposed mosaicking methods[14–18,21] as they are inherently 2D processes without the ability of (controlled) focus adjustments. Only Lagali *et al.*[19,20] describe a mosaicking process with manual focus variation during the image acquisition process; images that do not show SNP are sorted out manually afterwards.

In order to overcome the issue described above and to realise a reliable, highly automated SNP mosaicking process, we propose a novel approach for automatic online SNP focus tracking in the present article. To this end, the confocal microscope is equipped with a computer-controlled piezo drive unit that performs an oscillating movement of the focus plane during the image acquisition process. We present results from a feasibility test of the proposed setup in conjunction with the EyeGuidance system[22]. The aim of the present study is to examine the potential benefit in mosaic image quality and to evaluate the main process parameter of the focus oscillation, i.e. the oscillation velocity, and to compare three different approaches to create mosaic images from the recorded image sequences.

Methods

CCM imaging was performed using a Heidelberg Retina Tomograph II (HRT II, Heidelberg Engineering GmbH, Heidelberg, Germany) in conjunction with a modified Rostock Cornea Module (RCM) and the EyeGuidance system[21,22] to guide the eye movements of the examined person. The study received appropriate ethics committee approval from the institutional review board (Rostock University Medical Centre Ethics committee) in accordance with the Declaration of Helsinki. All examined volunteers gave their informed consent and – in accordance with the ethics committee approval – did not have any known neuropathic or ocular diseases.

Modified rostock cornea module. Compared to the original RCM[1] (Heidelberg Engineering GmbH, Heidelberg, Germany), the modified RCM is additionally equipped with a piezo driven actuator (MIPOS 600 SG DIG, Piezosystem Jena GmbH, Jena, Germany) to move the internal objective lens. Due to the changed local arrangement of the lenses of the RCM objective, the square field of view decreases from $0.160\,mm^2$ to $0.123\,mm^2$.

The piezo drive has a setting range of $500\,\mu m$ in closed loop control and can be controlled by a computer via an RS232 interface. An in-house developed adapter device integrates the piezo actuator into the RCM (see Fig. 2); due to the compact design, the piezo drive unit does not interfere with the CCM examinations.
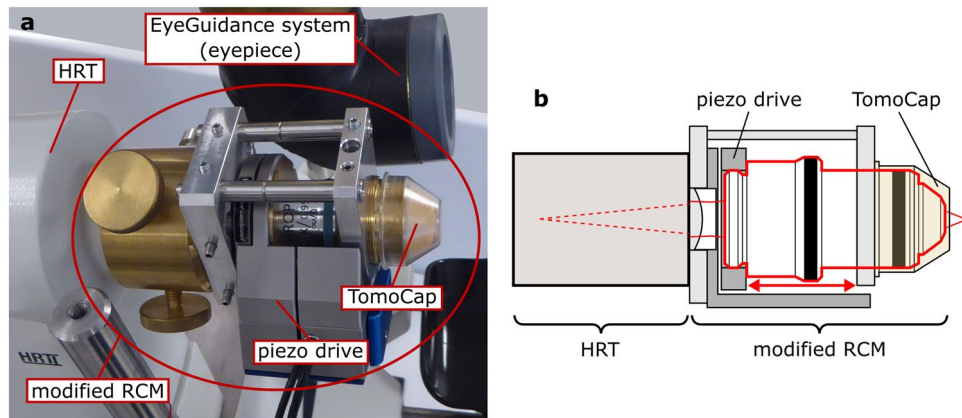
2

Figure 2. The modified Rostock Cornea Module (RCM). (**a**) Photograph of the modified RCM attached to the HRT II and next to the eyepiece of the EyeGuidance system. (**b**) Schematic drawing of the modified RCM; the piezo drive translates the objective (highlighted by red border) to effect focus changes; the contact TomoCap remains fixed in the process.
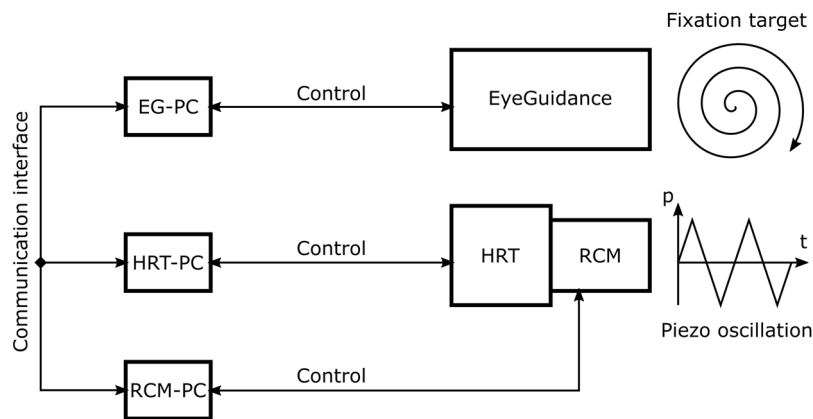

Figure 3. Schematic illustration of the CCM setup with focus plane control and guided eye movements.

EyeGuidance. To control the movements of the examined eye during the CCM image acquisition process, the EyeGuidance system presents a computer controlled fixation target to the contralateral eye. A smartphone (Motorola Moto G, Motorola Mobility Germany GmbH, Idstein, Germany) with an Android operating system is used to display the fixation target. The 4.5″ display has a pixel resolution of 1280 × 720. A special optical setup composed of four convex lenses and a tilted mirror realises a compact design suitable for CCM. Three linear axes allow the precise alignment of the eyepiece of the EyeGuidance system. A more detailed technical description of the EyeGuidance hardware setup has been published[22].

The EyeGuidance smartphone is connected to the controlling PC via USB. The parameters for the fixation target (e.g. path layout, size, colour, speed, acceleration) are defined in an XML file. During the CCM image acquisition process, the EyeGuidance software continuously calculates the position of the fixation target and sends it to the EyeGuidance App running on the smartphone. The update frequency depends on the PC performance; for the setup used in the present study, we measured an update frequency of the fixation target position of approximately 923 Hz, which reliably guarantees a smooth motion of the fixation target even at high velocities.

CCM setup with modified RCM and EyeGuidance. The schematic illustration of the CCM setup is shown in Fig. 3. Three dedicated PCs, connected via a TCP/IP network, are used to control the HRT II, the EyeGuidance system, and the modified RCM. The complete CCM image acquisition process is controlled via the HRT computer (HRT-PC, see Fig. 3) as described below.

CCM image acquisition process. As a preparation step the cornea of the examined eye was locally anaesthetised by instilling Proparakain 0.5% eye drops (Ursapharm, Saarbrücken, Germany) and the Vidisic gel (Bausch & Lomb/Dr. Mann Pharma, Berlin, Germany) is used as a coupling medium between objective and TomoCap as well as between TomoCap and cornea. After positioning the head of the patient in the forehead support, the operator aligns the EyeGuidance system in front of the not examined eye. The operator adjusts the HRT in the conventional way to achieve frontal SNP images of the central cornea. A joystick connected to the piezo drive offers a fine tuning of the focus.
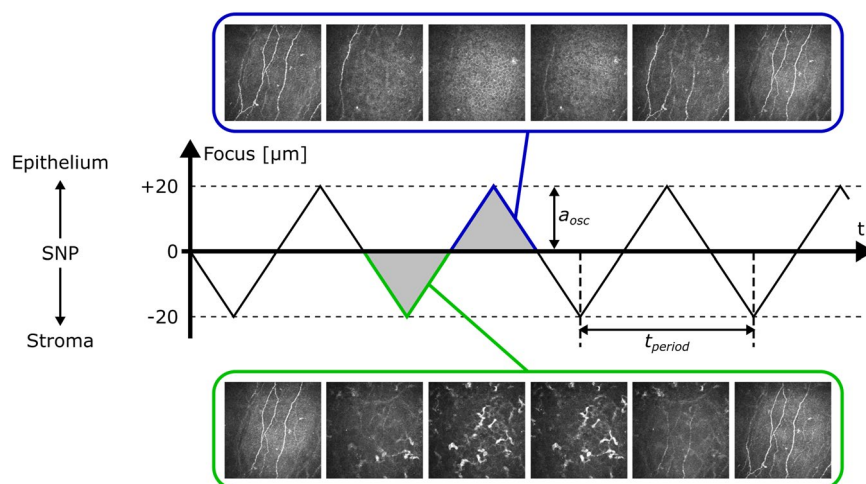
Figure 4. Oscillation of the focus plane during image acquisition. The focus starts in the SNP layer, and then describes a periodic triangular function.

	E1	E2	E3	E4
Focus oscillation velocity v_{osc} [µm/s]	60.6	121.2	181.8	242.4
Focus oscillation amplitude a_{osc} [µm]	20	20	20	20
Focus oscillation period t_{period} [s]	1.32	0.66	0.44	0.33
Fixation target velocity v_{targ} [pixel/s]	25.5	51	76.5	102

Table 1. Process parameters for examinations E1 through E4.

Following these manual initialisation steps, the operator starts the fully automated image acquisition process with the start button, which triggers a signal to EG-PC and RCM-PC. The movement of the EyeGuidance fixation target and the piezo oscillation start simultaneously. The fixation target moves with the predefined speed along an outward spiralling pattern with constantly spaced spiral windings. The piezo drive constantly oscillates with an amplitude $a_{osc} = 20$ µm and a constant speed v_{osc} along the slopes, describing a periodic triangular function (see Fig. 4). The period length is then given as $t_{period} = 4a_{osc}/v_{osc}$. The operator terminates the image acquisition process using the stop button after $t_{exam} = 40$ seconds, or earlier, if visual assessment of the live image quality is deemed unsatisfying. In that case, the examination is repeated.

In order to assess the influence of the focus oscillation parameters on the acquired image data and the resulting mosaic images, we performed repeated examinations with different settings for v_{osc} and the velocity of the fixation target v_{targ}. Table 1 lists the absolute values used for the examinations E1 (slow focus oscillation and fixation target movement) through E4 (fast focus oscillation and fixation target movement).

Mosaicking process.   In a post-processing step, mosaic images are calculated from the acquired image sequences. We use in-house developed algorithms to align the single images and to correct motion artefacts[24–26]. In order to create mosaic images from datasets with guided eye movements we developed a special image alignment process suitable for datasets recorded with a fixation target movement on an outward spiralling pattern[21].

As a first step, all images of a sequence were used for image alignment and correction of motion artefacts. Then, three different approaches for the montage of the mosaic image were implemented and applied to each dataset. The first approach (M1) considers all images of a dataset for the mosaic montage. A second mosaic image (M2) was created using only images from the oscillating focus sequence that had been recorded at a reference focus level. By definition of the process protocol, the imaging process starts in the SNP layer, thus this level was used as reference. Only one image was included from each slope of the oscillation process. In effect, this approach selects a 2D plane from the 3D image data, emulating the EyeGuidance process without focus oscillation[21] and therefore facilitating a direct comparison of both approaches in terms of mosaic image quality. The third image selection approach (M3) used an automated tissue classification algorithm that had been trained to classify CCM images as SNP or other corneal tissue[27]. Only images classified as SNP were incorporated into the M3 mosaic images.

Data Availability.   The datasets generated during the current study are available from the corresponding author on reasonable request.

Results
Data Acquisition.   The present study included nine volunteers that were recruited from the clinic staff. All volunteers underwent the four examinations described in the Methods section. The imaging duration was

		E1	E2	E3	E4
M1	Average mosaic image size [mm²]	1.34	2.44	3.39	4.62
	Average expansion rate [mm²/s]	0.033	0.062	0.089	0.117
	Average number of images used	1245.8	1187.3	1119.9	1178.7
M2	Average mosaic image size [mm²]	1.12	2.18	3.12	4.31
	Average expansion rate [mm²/s]	0.028	0.055	0.082	0.109
	Average number of images used	72.0	127.1	175.2	240.1
M3	Average mosaic image size [mm²]	1.25	2.30	3.09	4.38
	Average expansion rate [mm²/s]	0.031	0.059	0.081	0.111
	Average number of images used	482.4	469.2	406.3	468.7

Table 2. Mosaic image sizes and area expansion rates for examinations E1 through E4.

40 seconds for all examinations. Because of a very limited time slot of one volunteer, we decided to reduce the imaging duration to 30 seconds for all examinations for that person. According to our examination protocol, an examination was immediately repeated if the quality of the acquired image dataset was deemed insufficient based on the visual assessment of the live image during image acquisition. This was not the case for E1, E2 or E3, but for two volunteers in E4. In one of these two cases, we used the second of the two acquired datasets. In the other case, we stopped examination E4 after three unsuccessful attempts. Of the remaining eight successfully acquired datasets from E4 examinations, we had to exclude an additional one since it proved to be unsuitable for automated mosaic image generation due to insufficient image quality that originated from inhomogeneity in the contact gel, which was not recognised during image acquisition. The following results are therefore based on nine datasets for examinations E1 through E3 and the seven datasets from examination E4 that are suitable for mosaic image generation.

Mosaic Images. Three mosaic images M1, M2 and M3 were created from each of the datasets. Including all images, process M1 of course generates the maximum mosaic image size for all examinations (see Table 2). The number of images used for M2 is defined by the number of oscillation periods, t_{exam}/t_{period}, and therefore increases from 72.0 (5.7% of the recorded images) for E1 nearly proportionally to 240.1 (20.3% of the recorded images) for E4. Compared to M1, the average size of the M2 mosaic images is reduced about 16.6%, 11.0%, 8.1% and 6.4% for examinations E1, E2, E3 and E4, respectively. For M3, the percentage of images used is similar for all examinations (between 36.3% and 39.7%) and the ratio of the average image size between M3 and M1 lies in the range of 91% to 95%.

Figure 5 depicts representative examples for the mosaic images created from a single dataset with the processes M1, M2 and M3 (high-resolution versions of these images as well three additional examples from other datasets are available as Supplementary Figures S1 through S4). The mosaic images were evaluated qualitatively with regard to the visibility of the nerve structures of the SNP. Due to the oscillating movement of the focus plane, mosaic images created from all images in a dataset (M1, see Fig. 5a) always show a superimposition of epithelial tissue, nerve structures in the SNP layer, structures from Bowman's layer (so-called K-structures) and the keratocyte nuclei of the stroma. Most nerve structures are visible but provide only low contrast because of the superimposition of several tissues at most image locations. Where SNP nerves are visible in mosaic images created from the subset of images acquired on the reference focus level defined by the start of the imaging process (M2, see Fig. 5b and red circles in Fig. 6), they commonly possess very good contrast. However, the proportion of the mosaic image area that is optimally focused on the SNP layer varies widely. Some M2 mosaic images are focused well over almost the entire image field; others contain large regions of non-basal epithelial or stroma tissue that encompass more image area than SNP regions. The mosaic images created from the subset of images classified as SNP (M3, see Fig. 5c and solid circles in Fig. 6) show at least the nerves structures that are discernible in the M1 mosaic image. In contrast to the M1 montaging process, the majority of images containing non-SNP tissue is excluded prior to montaging the M3 mosaic images; according to the numbers of images used for the respective mosaicking processes (see Table 2), the proportion of excluded images ranges between 60.3% and 63.7% of all images. Consequently, the nerve structures manifest in M3 with good contrast against the surrounding tissue. The exclusion of images leads to the above-mentioned reduction of the field of view of the M2 and M3 mosaics.

Discussion

Although the majority of CCM studies of the SNP published in literature are based on the examination of sets of single CCM image frames, the number of publications on wide-field CCM image creation by different research groups has increased in recent years. Both the CCM-frame approach and the wide-field approach have their unique properties[12,19]. The most important advantages of the CCM-frame approach are the relatively straightforward and well-established image acquisition process and the good support for morphometric analysis of the standard-sized and -shaped CCM frames[12] by established software. Its major disadvantage is the necessity for manual selection of non-overlapping CCM frames from a larger pool of up to several hundreds of CCM images[12,28] that are recorded during the image acquisition phase; see Fig. 7 for a sample of eight SNP images manually selected from the same dataset used for Fig. 5. This step is time-consuming, requires expert knowledge and is prone to subjective bias effects[12,19]. By contrast, the wide-field approach is commonly more complex in terms of the software[12,14–21] and hardware[17,21] setup. Semi-automatic morphometric analysis of large mosaic images has been described as more laborious compared to standard CCM frames[12], although further developments towards
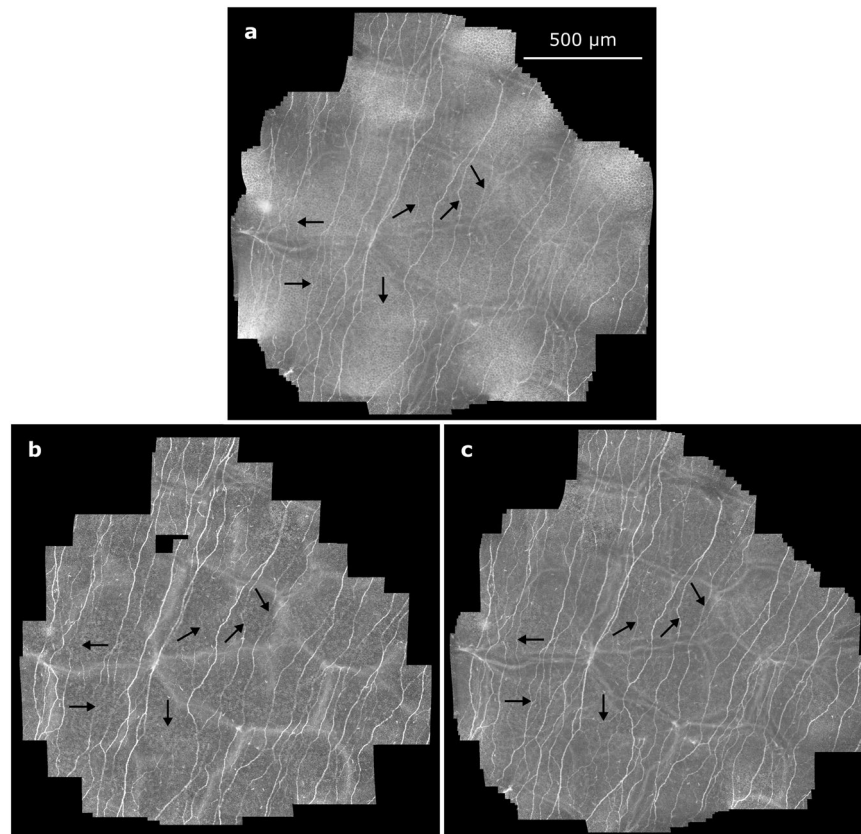
Figure 5. Mosaic images generated from a dataset (subject 8, examination E2); (**a**) mosaic image M1 using all 1245 images; (**b**) mosaic image M2 using the subset of 130 images acquired on the initial focus level; (**c**) mosaic image M3 using the subset of 610 images classified as SNP tissue. The arrows denote nerves that are visible in mosaic image M3 but not in M2.
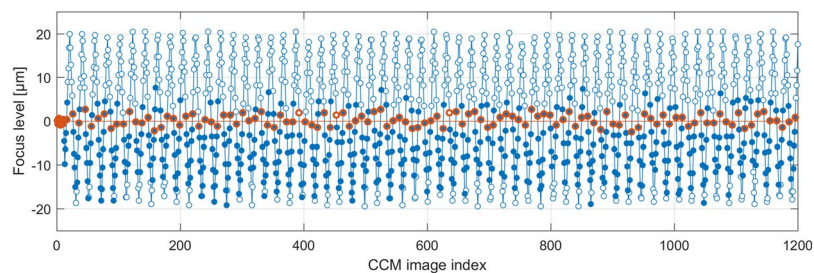

Figure 6. Plot of the focus levels of the CCM images (circles) of the dataset shown in Fig. 5. Red circles mark images acquired on the initial focus level. Solid circles mark CCM images classified as containing SNP tissue. These tend to lie below the initial focus level, and consequentially the M2 mosaic image in Fig. 5b tends towards showing epithelium tissue.

fully-automatic software tools can provide a solution[19,20]. A major advantage of the wide-field approach, on the other hand, is its capability to provide image data within a larger field of view, potentially allowing the clinician to repeatedly assess identical tissue regions[19]. Regarding the diagnostic value of both general approaches, Kheirkhah *et al.* find no significant differences[12], whereas Lagali *et al.* point out potential benefits in morphometric analysis of wide-field mosaic images[19].

Our aim is to develop a reliable, easy-to-use and fast tool for imaging and visualising an expanded area of the SNP. The 2D-only EyeGuidance process (2D-EG) without focus adjustment, originally published in 2014[21], achieved an average area expansion rate of approximately 0.16 mm²/s. Those examinations also established that a high velocity of the fixation target movement does not negatively influence the resulting mosaic image quality but has positive effects regarding the patient compliance, by decreasing the required examination time and because fast target movement is perceived as more comfortable than slow movement. Although already yielding promising results, the primary limitation of the 2D-EG process is its inability to compensate deviations of the
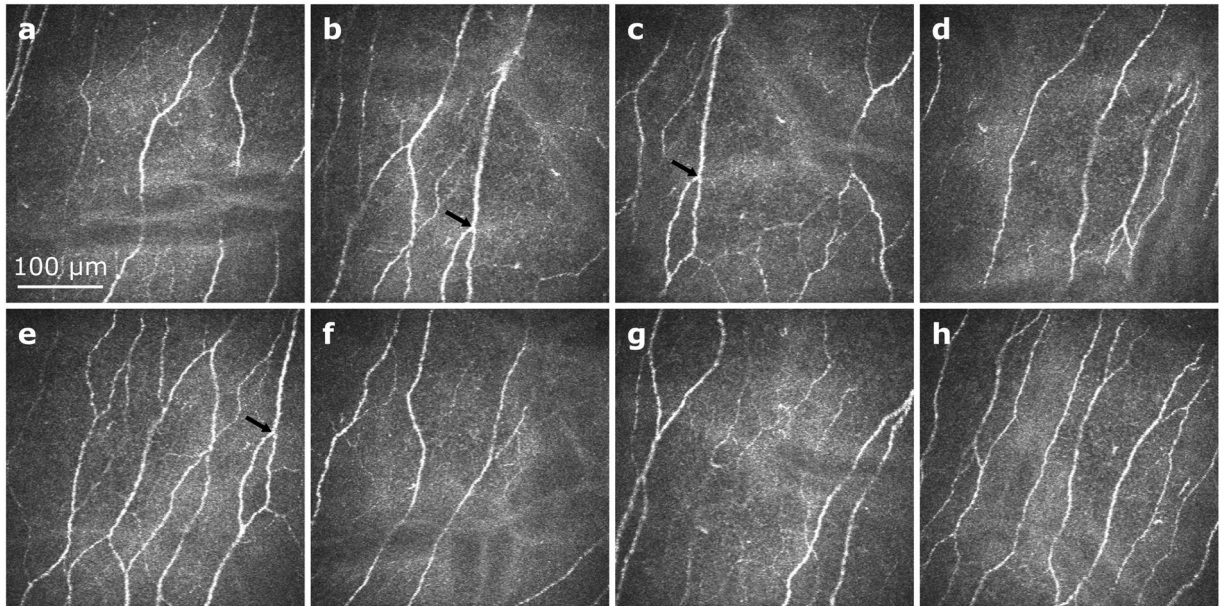
Figure 7. Exemplary sample of eight CCM images of the SNP manually selected from the dataset used for Fig. 5 (subject 8, examination E2, 1246 images total). Repeated presence of the same SNP region in multiple images (as for example in subfigures (**b,c,e**) see black arrows) can potentially introduce bias effects to morphometric parameter measurements and should therefore be avoided; identification of such repeatedly represented SNP regions in a manual image selection procedure is not trivial.

focus plane from the SNP layer, which are encountered in practice for multiple reasons and are difficult or even impossible to avoid[21].

The focus of the present study lies on the evaluation of an automated oscillation of the focus plane during image acquisition, effectively extending the process into the third dimension (3D-EG). The main process parameter that changes between the examinations E1 through E4 is the focus oscillation velocity v_{osc}. The fixation target velocity was adjusted such that the fixation target translation throughout an oscillation period always remained constant, i.e. the ratio between v_{osc} and fixation target velocity was identical for all examinations (see Table 1). The relation between the two velocities was chosen such that after one focus oscillation period (corresponding to two passes through the SNP layer) the resulting lateral displacement between the CCM images was approximately 200 μm.

The first objective was to analyse the examination duration, as this is essential for patient comfort and compliance. As expected, the measured average area expansion rates (see Table 2) are directly proportional to the speed of the fixation target respectively the oscillation velocity v_{osc} (see Table 1). An average area expansion rate of 0.11 to 0.12 mm²/s (depending on the mosaicking approach used) was measured for the fastest oscillation velocity, which is a decrease of only 26–31% compared to the 0.16 mm²/s of the 2D-EG process[21]. This is an interesting and unexpected finding, considering that the field of view of the modified RCM is reduced about 23% and the new 3D-EG process essentially covers a volume of tissue extending 40 μm in depth, instead of just a single plane. Regarding the question, whether v_{osc} can be increased further in order to accelerate the imaging process, it is important to look at the translation of the focus plane between two adjacent images. In examination E4, the focus plane moves about 8 μm during the recording of a single image. This distance is already in the order of the depth of field of the microscope[29]. Increasing the v_{osc} beyond the value used for E4, although technically possible, is not practicable because it would no longer be guaranteed that at least a single image of the SNP layer is acquired along each slope of the focus oscillation process. Further acceleration of the imaging process can therefore only be achieved by decreasing the oscillation amplitude.

Regarding the reliability of the imaging process, we did not find any qualitative difference between examinations E1 through E3. All of those examinations were successfully completed at the first attempt. In contrast, examination E4 had to be repeated for two volunteers due to unsatisfactory quality of the dataset, and we finally only obtained seven mosaic images from the nine volunteers, as described in the Results section. For one of the two missing datasets, the exclusion could be attributed to inhomogeneity in the contact gel, which happens during preparation of the device. This exclusion is therefore unrelated to the process parameters of the oscillation process. The noticeable increase in the number of repetitions in E4 might be related to the process parameters, i.e. the higher oscillation and fixation target velocities. However, as the order of the examinations was not randomised and the other three examinations always preceded E4, it may also be an effect of diminishing participant compliance over time. Finally, considering the relatively low number of participants, no correlation can be established between v_{osc} and the reliability of the imaging process based on the analysed data.

Based on the proportional relationship between oscillation velocity and average area expansion rate stated above, we conclude that faster oscillation velocities possess the advantage of reducing the required examination

time and allow faster fixation target movement, which is perceived as more comfortable by the examined volunteers. Further investigation is required to find whether a very high v_{osc} in the order of the velocity used for E4 reduces the reliability of the imaging process. However and in any case, even the process parameters of examination E3 allow an average expansion rate of covered SNP area of more than 0.08 mm²/s and facilitate an examination duration of less than 20 seconds for a target area of 1.5 mm².

The second objective of the present study was to assess the mosaic image quality. No systematic differences were found between examinations E1 through E4. The differences in mosaic image quality between the mosaicking approaches M1 through M3, however, are obvious (see Fig. 5 and Supplementary Figures S1 through S4). The comparative qualitative evaluation of the three presented mosaic montaging processes has to be guided by the question of how the characteristics of the resulting mosaic images affect the reliable quantitative morphometric characterisation of the SNP. Two potential detrimental factors play a major role in this regard:

- incorrect nerve fibre segmentation, encompassing both unsegmented nerve structures (false negatives) and segmented structures that are not nerve fibres (false positives) and
- incorrect tissue regions, i.e. mosaic image regions showing tissue from above or below the SNP layer.

The second point is of particular interest as, even assuming a perfect segmentation procedure, such incorrect tissue regions lead to an underestimation bias of the morphometric parameter measurements, which are commonly normalised to the assessed area (cf. corneal nerve fibre length, corneal nerve fibre density, corneal nerve branch density[13,24,30,31]). Incorrect tissue regions represent image area without adding any nerve fibres or branches.

These two points clearly reveal the deficits of the mosaicking approaches M1 and M2. The M1 mosaics contain practically no regions with no SNP tissue visible, which of course is the intent of the focus oscillation during the imaging process. However, the low contrast of the nerve structures in the mosaics is counterproductive for correct nerve fibre segmentation and therefore carries the risk for increased deviations of the measured SNP parameters compared to the M2 and M3 mosaics. In some cases, the contrast can even be reduced to a level where the nerve fibres almost disappear, although nerves have been imaged at the respective location, as evidenced by the corresponding M3 mosaic (see Fig. 5).

As the M2 mosaics are composed from images from a specific, constant focus depth, they manifest a very similar characteristic as the ones that result from the originally proposed 2D-EG process[21]. Their good contrast supports the correct segmentation of nerve structures. Contrary to the other two mosaicking approaches, however, they can potentially contain ill-focused image regions and consequentially carry the risk of reducing the accuracy of the measured SNP parameters.

The M3 mosaics combine the advantages of both of the other approaches while at the same time avoiding the disadvantages: They provide satisfactory contrast of the nerve fibres in order to support reliable nerve segmentation and they do not contain ill-focused tissue regions. Such regions can only be avoided by continually controlling the focus, which cannot be adjusted manually while at the same time minimising the duration of examination[21]. The advantageous effects of small focus variations on the wide-field visualisation of the SNP are in general accordance with the conclusions drawn by Lagali *et al.*[19].

The primary purpose of the present article is to provide a detailed description of the highly automated 3D-EG process and to evaluate its technical parameters. The results demonstrate the feasibility of the process and the qualitative advantages with regard to SNP visualisation, as compared to 2D-only mosaicking approaches. Further evaluation of the diagnostic utility of the 3D-EG process was not within the scope of the presented feasibility study, therefore no morphometric parameters were calculated in the mosaic images. However, two previously published results from larger studies have to be taken into account: the reported absence of significant quantitative differences between SNP morphometry measurements in sets of single CCM frames and in wide-field images[12], and the reported benefits of systematic focus variations on the resulting wide-field images of the SNP[19]. Given these previous results, the diagnostic utility of the presented 3D-EG process can be assumed to be at least equal to other published CCM techniques.

A further limitation of the presented system is the complex setup with three connected PCs (see Fig. 3), which is not suitable in clinical practice. This setup originates from the distributed development of the software modules. For a potential future system intended to be used for wide-field CCM in a clinical environment, it is necessary to integrate all software modules into a single, dedicated PC system.

In the current implementation of the described process, the mosaicking step can only start after the entire image dataset has been recorded. The quality of the imaging process has to be estimated based on the rapidly changing live image (see Supplementary Videos S5 through S8), which requires a lot of expert knowledge and is prone to misjudgement. With a potential real-time mosaic image visualisation, the operator could directly assess the quality of the growing mosaic image. This could allow earlier termination and repetition of the examination and reduce overall examination time for the patient. Future development work will therefore be dedicated towards realising an online mosaicking process with tissue classification[27,32] and a real-time control of the focus oscillation parameters. The purpose of this control scheme is to reduce the oscillation amplitude and continuously adjust the zero-position of the oscillation in order to reduce the examination duration further while at the same time reliably keeping the SNP layer inside the oscillation range (see Supplementary Video S9 for a simulated animation of online mosaicking with tissue classification).

As the presented process captures image data extending into the third dimension, reconstructing a volume representation of the acquired tissue region could provide valuable additional information, not only for imaging the SNP but also potentially for other tissues. This will also be an interesting topic for future research work.

In conclusion: We proposed a novel concept for automated wide-field CCM imaging of the SNP and provided results of the first feasibility study. Using an externally mounted, piezo-driven focus control unit, we realised a fast 3D imaging process that facilitates the reliable acquisition of the SNP and adjacent tissue layers. A tissue classification algorithm filters the CCM datasets, keeping only images of the SNP layer. The direct comparison of mosaic images composed of these SNP-filtered 3D datasets against mosaic images montaged from a 2D plane clearly reveals the advantages of the proposed concept over 2D-only mosaicking approaches.

References

1. Guthoff, R. F., Baudouin, C. & Stave, J. *Atlas of Confocal Laser Scanning In-vivo Microscopy in Ophthalmology. Principles and Applications in Diagnostic and Therapeutic Ophthalmology* (Springer, 2006).
2. Kim, J. & Markoulli, M. Automatic analysis of corneal nerves imaged using *in vivo* confocal microscopy. *Clin. Exp. Optom.* **101**, 147–161 (2018).
3. Cruzat, A., Qazi, Y. & Hamrah, P. *In Vivo* Confocal Microscopy of Corneal Nerves in Health and Disease. *Ocul. Surf.* **15**, 15–47 (2017).
4. Kinard, K. I. *et al*. Chronic migraine is associated with reduced corneal nerve fiber density and symptoms of dry eye. *Headache* **55**, 543–549 (2015).
5. Bitirgen, G., Akpinar, Z., Malik, R. A. & Ozkagnici, A. Use of Corneal Confocal Microscopy to Detect Corneal Nerve Loss and Increased Dendritic Cells in Patients With Multiple Sclerosis. *JAMA Ophthalmol.* **135**, 777–782 (2017).
6. Petropoulos, I. N. *et al*. Corneal Confocal Microscopy. An Imaging Endpoint for Axonal Degeneration in Multiple Sclerosis. *Invest. Ophthalmol. Vis. Sci.* **58**, 3677–3681 (2017).
7. Rousseau, A. *et al*. Potential Role of *In Vivo* Confocal Microscopy for Imaging Corneal Nerves in Transthyretin Familial Amyloid Polyneuropathy. *JAMA Ophthalmol.* **134**, 983–989 (2016).
8. De Clerck, E. E. B. *et al*. New ophthalmologic imaging techniques for detection and monitoring of neurodegenerative changes in diabetes: a systematic review. *Lancet Diabetes Endocrinol.* **3**, 653–663 (2015).
9. Tavakoli, M. *et al*. Corneal confocal microscopy: a novel noninvasive test to diagnose and stratify the severity of human diabetic neuropathy. *Diabetes Care* **33**, 1792–1797 (2010).
10. Lovblom, L. E. *et al*. *In vivo* corneal confocal microscopy and prediction of future-incident neuropathy in type 1 diabetes. A preliminary longitudinal analysis. *Can. J. Diabetes* **39**, 390–397 (2015).
11. Patel, D. V. & McGhee, C. N. J. Mapping of the normal human corneal sub-basal nerve plexus by *in vivo* laser scanning confocal microscopy. *Invest. Ophthalmol. Vis. Sci.* **46**, 4485–4488 (2005).
12. Kheirkhah, A. *et al*. Comparison of standard versus wide-field composite images of the corneal subbasal layer by *in vivo* confocal microscopy. *Invest. Ophthalmol. Vis. Sci.* **56**, 5801–5807 (2015).
13. Vagenas, D. *et al*. Optimal image sample size for corneal nerve morphometry. *Optom. Vis. Sci.* **89**, 812–817 (2012).
14. Zhivov, A., Blum, M., Guthoff, R. F. & Stachs, O. Real-time mapping of the subepithelial nerve plexus by *in vivo* confocal laser scanning microscopy. *Br. J. Ophthalmol.* **94**, 1133–1135 (2010).
15. Poletti, E., Wigdahl, J., Guimarães, P. & Ruggeri, A. Automatic montaging of corneal sub-basal nerve images for the composition of a wide-range mosaic in *Proceedings of the 2014 36th Annual International Conference of the IEEE Engineering in Medicine and Biology Society (EMBC)*, 5426–5429 (IEEE, 2014).
16. Turuwhenua, J. T., Patel, D. V. & McGhee, C. N. J. Fully automated montaging of laser scanning *in vivo* confocal microscopy images of the human corneal subbasal nerve plexus. *Invest. Ophthalmol. Vis. Sci.* **53**, 2235–2242 (2012).
17. Edwards, K. *et al*. Wide-field assessment of the human corneal subbasal nerve plexus in diabetic neuropathy using a novel mapping technique. *Cornea* **31**, 1078–1082 (2012).
18. Vaishnav, Y. J., Rucker, S. A., Saharia, K. & McNamara, N. A. Rapid, automated mosaicking of the human corneal subbasal nerve plexus. *Biomed. Tech. (Berl.)* **62**, 609–613 (2017).
19. Lagali, N. S. *et al*. Reduced Corneal Nerve Fiber Density in Type 2 Diabetes by Wide-Area Mosaic Analysis. *Invest. Ophthalmol. Vis. Sci.* **58**, 6318–6327 (2017).
20. Lagali, N. S. *et al*. Wide-field corneal subbasal nerve plexus mosaics in age-controlled healthy and type 2 diabetes populations. *Sci. Data* (accepted, 2018).
21. Allgeier, S. *et al*. Mosaicking the subbasal nerve plexus by guided eye movements. *Invest. Ophthalmol. Vis. Sci.* **55**, 6082–6089 (2014).
22. Köhler, B. *et al*. EyeGuidance – a computer controlled system to guide eye movements. *Curr. Dir. Biomed. Eng.* **2**, 433–436 (2016).
23. Allgeier, S. *et al*. A novel approach to analyze the progression of measured corneal sub-basal nerve fiber length in continuously expanding mosaic images. *Curr. Eye. Res.* **42**, 549–556 (2017).
24. Ziegler, D. *et al*. Early detection of nerve fiber loss by corneal confocal microscopy and skin biopsy in recently diagnosed type 2 diabetes. *Diabetes* **63**, 2454–2463 (2014).
25. Allgeier, S. *et al*. Image reconstruction of the subbasal nerve plexus with *in vivo* confocal microscopy. *Invest. Ophthalmol. Vis. Sci.* **52**, 5022–5028 (2011).
26. Allgeier, S. *et al*. Elastische Registrierung von *in-vivo*-CLSM-Aufnahmen der Kornea in *Bildverarbeitung für die Medizin 2011. Algorithmen - Systeme - Anwendungen* (eds Handels, H., Ehrhardt, J., Deserno, T. M., Meinzer, H.-P. & Tolxdorff, T.), 149–153 (Springer, 2011).
27. Bartschat, A. *et al*. Automatic corneal tissue classification using bag-of-visual-words approaches in *Forum Bildverarbeitung 2016* (eds Puente León, F. & Heizmann, M.), 245–256 (KIT Scientific Publishing, 2016).
28. Petropoulos, I. N. *et al*. Rapid automated diagnosis of diabetic peripheral neuropathy with *in vivo* corneal confocal microscopy. *Invest. Ophthalmol. Vis. Sci.* **55**, 2071–2078 (2014).
29. Zhivov, A., Stachs, O., Stave, J. & Guthoff, R. F. *In vivo* three-dimensional confocal laser scanning microscopy of corneal surface and epithelium. *Br. J. Ophthalmol.* **93**, 667–672 (2009).
30. Messmer, E. M., Schmid-Tannwald, C., Zapp, D. & Kampik, A. *In vivo* confocal microscopy of corneal small fiber damage in diabetes mellitus. *Graefes Arch. Clin. Exp. Ophthalmol.* **248**, 1307–1312 (2010).
31. Pritchard, N. *et al*. Longitudinal assessment of neuropathy in type 1 diabetes using novel ophthalmic markers (LANDMark). Study design and baseline characteristics. *Diabetes Res. Clin. Pract.* **104**, 248–256 (2014).
32. Bartschat, A. *et al*. Augmentations of the bag of visual words approach for real-time fuzzy and partial image classification in *Proceedings. 27. Workshop Computational Intelligence. Dortmund, 23. - 24. November 2017* (eds Hoffmann, F., Hüllermeier, E. & Mikut, R.), 227–242 (KIT Scientific Publishing, 2017).

Acknowledgements

Author Contributions

S.A., R.M., O.S. and B.K. designed the experiment. S.B., S.P., K.M.R., K.S., M.W., O.S. and B.K. conducted the experiment. S.B., K.S., O.S. and B.K. developed and operated the modified RCM module. S.A., K.M.R. and B.K. developed and applied the mosaicking algorithm. A.B. and R.M. developed and applied the tissue classification algorithm. S.A. and B.K. analysed and interpreted the results. S.A. and B.K. wrote the manuscript. S.A., A.B., S.B., S.P., K.M.R., K.S., M.W., V.H., R.M., O.S. and B.K. critically reviewed the manuscript.

Additional Information

Supplementary information accompanies this paper at https://doi.org/10.1038/s41598-018-25915-6.

Competing Interests: The authors declare no competing interests.

Publisher's note: Springer Nature remains neutral with regard to jurisdictional claims in published maps and institutional affiliations.

In vivo corneal confocal microscopy aided by optical coherence tomography

Sebastian Bohn, Karsten Sperlich, Heinrich Stolz, Rudolf F. Guthoff, and Oliver Stachs

Copyright notice

In vivo corneal confocal microscopy aided by optical coherence tomography

SEBASTIAN BOHN,[1,2,4,5] KARSTEN SPERLICH,[1,2,4,6] HEINRICH STOLZ,[3] RUDOLF F. GUTHOFF,[1,2] AND OLIVER STACHS[1,2]

[1]*Department of Ophthalmology, Rostock University Medical Center, 18057 Rostock, Germany*
[2]*Department Life, Light & Matter, University Rostock, 18051 Rostock, Germany*
[3]*Institute of Physics, University Rostock, 18059 Rostock, Germany*
[4]*Co-first authors with equal contribution*
[5]*sebastian.bohn@uni-rostock.de*
[6]*karsten.sperlich@uni-rostock.de*

Abstract: *In vivo* corneal confocal microscopy and its operability in scientific as well as in clinical applications is often impaired by the lack of information on imaging plane position and orientation inside the cornea during patient's examination. To overcome this hurdle, we have developed a novel corneal imaging system based on a commercial scanning device and a modified Rostock Cornea Module. The presented preliminary system produces *en face* images by confocal laser scanning microscopy and sagittal cross-section images by optical coherence tomography simultaneously. This enables imaging guidance during examinations, improved features for diagnostics along with thickness measurements of the cornea as well as corneal substructures from oblique sections.

1. Introduction

Laser-based imaging modalities like scanning laser ophthalmoscopy (SLO) and optical coherence tomography (OCT) became indispensable for noninvasive *in vivo* diagnostics of the eye, especially the retina. The multimodal combination of these techniques offers several possibilities, which have been thoroughly published over the past decades [1,2].

Simultaneously, corneal confocal microscopy (CCM) and OCT became valuable tools for imaging the anterior segment of the living eye. Different modalities of CCM enabled cellular examination and characterization of the central and peripheral cornea, tarsal and palpebral conjunctiva or lid tissues [3]. Despite its advantageous value, CCM suffers from a small field of view, limited depth resolution and the lack of precise knowledge of image position and orientation inside the cornea. To overcome some of these limitations, especially the latter one, we applied the multimodal retinal imaging approach to corneal imaging. In order to achieve this, we adapted a dedicated lens module to a commercially available multimodal imaging platform for the posterior segment of the eye combining SLO and OCT. The lens module shifts the *en face* imaging plane from the retina to the cornea in the same way as it was previously described for single modal imaging systems [4,5].

OCT-guided CCM can potentially improve the diagnostic value and simplify the alignment procedure during contact measurements of the cornea due to the real-time information about CCM image position and orientation gained by OCT. As a matter of course, the axial resolution of OCT has been dramatically increased in the past years and thickness measurements of single corneal layers are available by ultrahigh-resolution OCT [6,7], but it does not provide cellular *en face* information of the cornea. While the OCT provides corneal thickness and depth data directly, its combination with CCM provides cellular *en face* information of distinct corneal layers, which are not available using the OCT technology. Addressing this lack of information, the OCT-guided corneal imaging concept,

presented in this paper, offers the possibility of thickness measurements and simultaneous cellular *en face* imaging of the same region with a single device.

2. Materials and methods

The imaging system consists of a customized, modular lens adapter in conjunction with a modified SPECTRALIS OCT2 platform (Heidelberg Engineering GmbH, Heidelberg, Germany) with a high magnification objective (HMO, Heidelberg Engineering GmbH, Heidelberg, Germany) attached. This platform combines SLO and OCT. The lens adapter is a completely redesigned version of the so-called Rostock Cornea Module (RCM, Heidelberg Engineering GmbH, Heidelberg, Germany) and was presented recently as RCM 2.0 [5,8]. It utilizes a piezo actuator for closed-loop focal plane control, including through focusing, of up to 500 μm. Equipped with a water immersion objective lens (Achroplan 63x/0.95 W; Zeiss, Jena, Germany), the RCM 2.0 creates a flat imaging plane into the cornea. A sterile cap (TomoCap) is used to contact the cornea. Immersion gel is applied between the objective lens and TomoCap as well as in between TomoCap and cornea in order to reduce surface reflections. The TomoCap remains in a fixed position during focal plane changes but can be displaced beforehand in order to adjust the initial focus. This is especially useful for imaging of the topmost cell layers, where a certain distance between the TomoCap and corneal surface is necessary. Otherwise, if the focal plane is almost at the TomoCap surface, strong reflections arise from the refractive index difference and impede imaging. Thus, imaging of superficial cells requires a specific immersion gel layer between TomoCap and cornea.

CCM and OCT modalities share a common beam path through the SPECTRALIS. Therefore, the optical path length changes with the addition of the RCM 2.0 optics. In order to have an interference signal, the OCT reference arm has to be adjusted accordingly, see Fig. 1. That was realized by a modification to the axial scanner inside the SPECTRALIS OCT2.
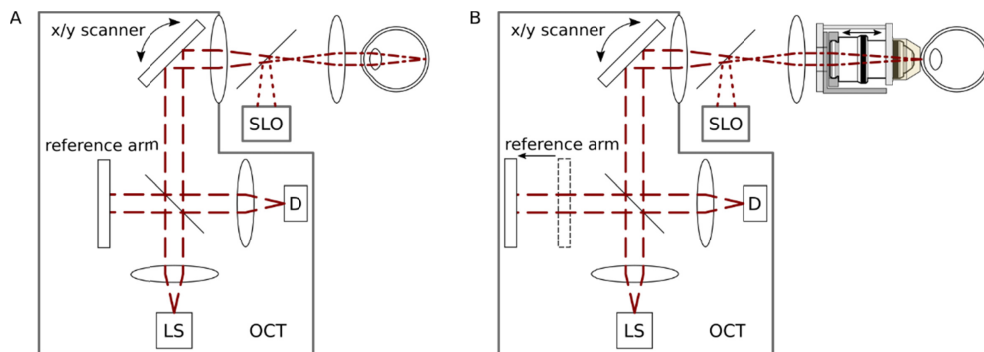

Fig. 1. Simplified schematic of an SLO-OCT-combination and reference arm readjustment. The original position of the mirror in the reference arm (A) is moved (B) to account for the change in optical path length induced by the additional optics of the RCM 2.0. Red lines show different beam paths (dashed – OCT, dotted – SLO). Both beam paths are overlapped (dotdashed line) in such a way that they have the same focus. D – detector. LS – light source.

Since the SPECTRALIS OCT2 is designed for the retina, it uses a refractive index of $n_{retina} = 1.36$ for the axial OCT scale. This needs to be rescaled according to the average refractive index of the cornea $n_{cornea} = 1.376$ [9]. OCT-guided CCM was performed simultaneously with an 805x805 μm² field of view at a wavelength of 815 nm for CCM (*en face,* xy-image) and 760x1898 μm² at a central wavelength of 880 nm with a bandwidth of 80 nm for the OCT B-scan (sagittal image, xz-section). Regarding the CCM image, this is an increase of almost a factor of five compared to the current HRT/RCM 2.0 combination with its 350x350 μm² [5]. This increased field of view is due to different optics and an increased scanning angle of 30°. The SPECTRALIS system offers high speed (HS) and high resolution (HR) modes, which affect the framerates and pixel resolutions of both modalities (HS: CCM

with 768x768 pixels at 8.9 fps and OCT with 768x496 pixels at 90 fps; HR: CCM with 1536x1536 pixels at 4.8 fps and OCT with 1536x496 pixels at 50 fps). The OCT images are cropped in the axial direction, as the corneal thickness is only a fraction of the OCT imaging depth. Please note the anisotropic scale in the OCT image and also the slightly different x-scales between OCT and CCM image. Both may be corrected by a rescaling done in a post-process. However, it is better to address the latter by a scanning angle calibration.

Due to a sufficient refractive index change at the cornea's anterior and posterior surface, the total corneal thicknesses can directly be measured in the OCT image. Inside the cornea, the refractive index change is very small. Structures like the Bowman's membrane can be identified using the SPECTRALIS OCT2 combined with the Anterior Segment Module. However, due to small depth of focus induced by the RCM 2.0, the intensity decreases rapidly for out-of-focus structures. Therefore, particular corneal layer interfaces can only be visualized in the OCT channel, if CCM imaging plane is near the interface. Although this enables direct measurements of the epithelial thickness, this does not apply to thin layers as for instance the Bowman's membrane. Hence, direct thickness measurements of corneal substructures are challenging. Anyhow, they are feasible by various techniques. In case of epithelial thickness, these are namely high-frequency ultrasound [10], high-resolution OCT [11–13] or confocal microscopy through focusing [14]. But while the first two methods do not offer a corresponding high-resolution *en face* image at the thickness measurement position, the latter one does. Nevertheless, due to post-processing and 3D stack reconstruction, this method is very time consuming and complex [5,15]. Another solution to overcome this problem is to exploit oblique CCM sections in conjunction with their corresponding OCT scans. The OCT image contains the angle α between corneal surface and CCM imaging plane. With this additional information, the layer thickness can be calculated. Figure 2 demonstrates the calculation of the layer thickness t by trigonometric relations and the approximation of a plane corneal surface for a small arc length. The OCT imaging plane lies in the paper plane and the CCM imaging plane goes into it. The projected distance d and the angle α are measured in the CCM and OCT image, respectively. The thickness t is then simply the product of the distance d and the sine of α.
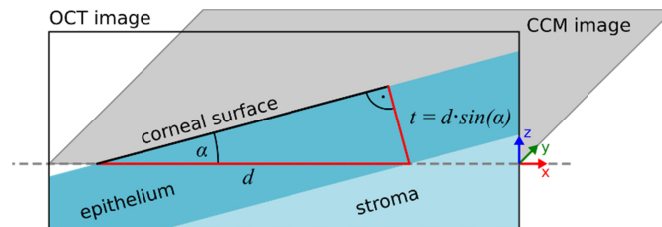

Fig. 2. Exemplary determination of the epithelial thickness t by an oblique cornea section. The OCT imaging plane lies in the paper plane while the CCM imaging plane (gray) goes into the paper. The angle α is measured in the OCT image and the distance d in the CCM image.

The following results are measurements performed on a 51-year-old healthy male subject. The study was conducted in accordance with the Declaration of Helsinki and it was explained in detail to the subject. Informed consent was obtained before any investigative procedures were conducted. In this feasibility study, no further subjects were examined.

3. Results

Figure 3 to 5 combine simultaneously taken CCM and OCT images of a cornea. Since both modalities share the same optical path in the RCM 2.0, they also have approximately the same focal point. Due to the tight focus of the RCM 2.0 objective lens, the most intense backscattered OCT signal originates from the OCT focus, which is essentially the place of the CCM image plane. This is the reason, why the CCM image plane is visible in the OCT image and why its movement in the OCT image can be easily traced while changing the focus or in

through focusing experiments during image stack acquisition (Fig. 3(A)). In the presented case of Fig. 3, the OCT image displays the cornea's anterior (here in contact with the TomoCap) and posterior interface. This allows corneal thickness measurements in the OCT image. In Fig. 3 the total cornea thickness is 593 μm and the CCM imaging plane is 476 μm below the corneal surface. Compared to the published values of the central corneal thickness [16], the measured value seems to be too large. Corneal thickness measurements by Scheimpflug photography (Pentacam, Oculus, Germany) provided 548 μm centrally and 600 μm in 3 mm distance from the apex. Presumably, the Fig. 3 was taken paracentral. The OCT image also reveals a so-called mirror artifact arising from the Fourier transformation [17]. This artifact is identified by the opposite direction of curvature. Furthermore, the TomoCap surface and the CCM image plane do not appear to be flat. This is most likely due to an improper optical path length calibration. Hence, the cornea shows a wrong curvature in the OCT images. This problem can be addressed by image post-processing or by software calibration of the imaging system's optical path length. Beyond that, a locally dependent intensity scaling may help to increase the visibility of the surfaces in OCT images.
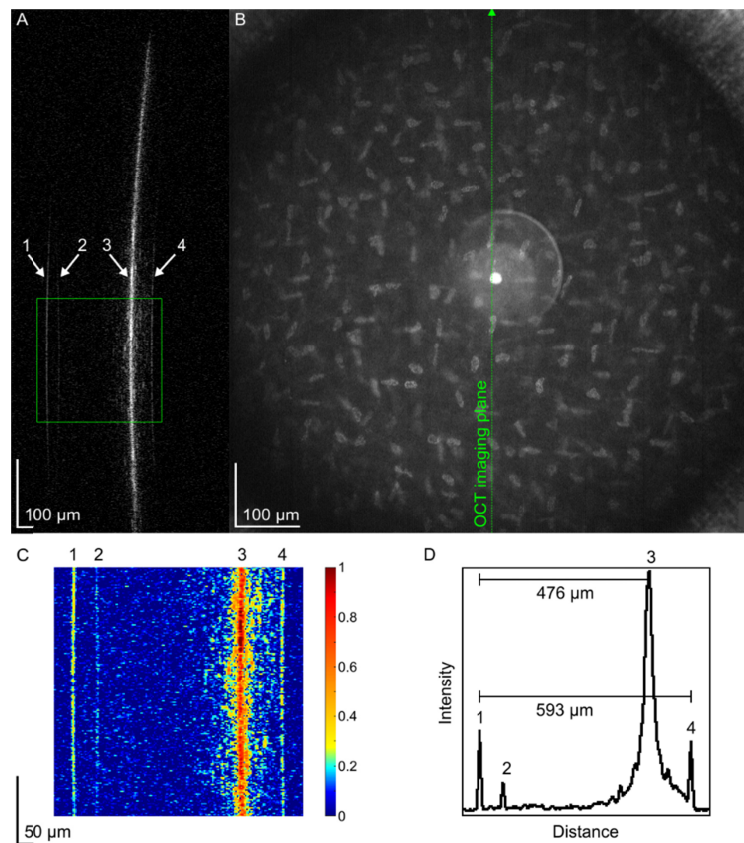

Fig. 3. Sagittal OCT (A) and *en face* CCM (B) image of the posterior stroma. The OCT image shows the anterior corneal surface in contact with the TomoCap (1), a mirror artifact (2), the CCM imaging plane (3) and the posterior corneal surface (4). The area in the green rectangle is magnified and depicted in a pseudocolor image (C) for visual purpose. The same area was used for the averaged intensity profile (D). Direct measurements provide a corneal thickness of 593 μm and a CCM imaging plane depth of 476 μm. Please note the anisotropic scale in the OCT images (A) and (C).

Figure 3(B) reveals central surface reflections caused by suboptimal coatings of the RCM 2.0 objective lens. Also, the image corners are obscured. An improved optical system may help to overcome these problems.

Figure 4 shows the corneal surface in the OCT image even in regions where it is invisible in the CCM image, while also showing the CCM imaging plane outside the cornea in the OCT image due to immersion gel. This feature can be exploited for easier alignment in the first stage of a subject examination. By considering two perpendicular OCT scans the operator is able to align the CCM imaging plane to the cornea's apex before the TomoCap touches the cornea. Please note that Fig. 4 was captured in HR mode with the lower framerate. Hence, movement distortions (Fig. 4(B): arrows denoted with 6) are more likely to occur as seen in the CCM image. In order to reduce eye movements, a dedicated curved contact cap was proposed in [5].
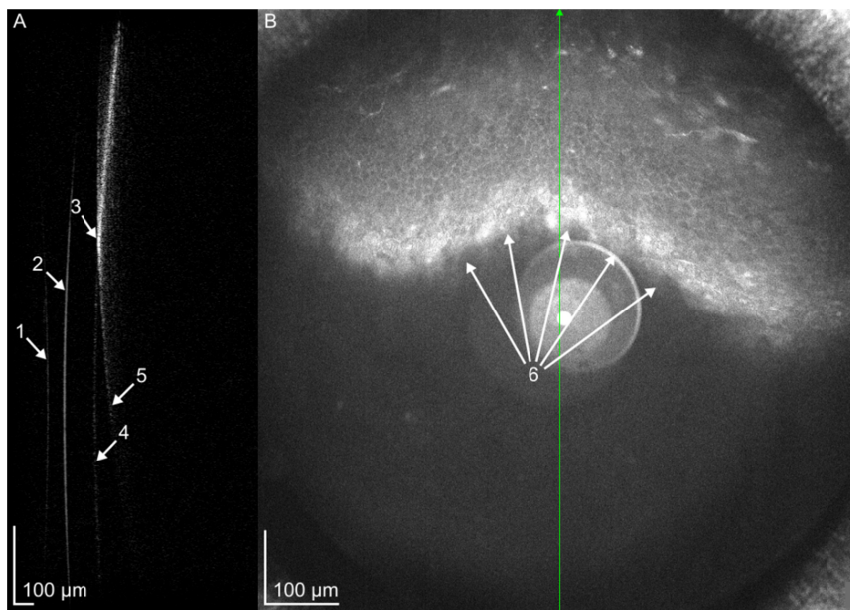

Fig. 4. OCT (A) and CCM (B) image showing the cornea before contact with the TomoCap. The OCT image exhibits a mirror artifact (1), the contact surface of the TomoCap (2), the intersection of the CCM imaging plane with the corneal surface (3), the CCM imaging plane also visible outside the cornea due to the immersion gel (4), and the corneal surface (5). The CCM image shows an oblique section starting from outside the cornea (middle), crossing the epithelium and showing some structures of the Bowman's membrane (top). Due to the low frame rate of the HR mode, the CCM image shows wavy movement distortions (6).

An oblique CCM image and the corresponding OCT image are shown in Fig. 5. The epithelial and Bowman's membrane thicknesses were exemplary determined in the same way as proposed in section 2. Therefore, the OCT image (Fig. 5(A)) was rectified to correct the wrong curvatures and stretched to obtain an isotropic resolution (Fig. 5(C)). To rectify this image region, its rows are shifted horizontally until their maximum intensity values have the same horizontal position. After this post-process, the CCM imaging plane appears as a straight vertical line in the OCT image. The angle between the corneal surface and CCM imaging plane was approximated to $(10.5 \pm 0.5)°$. The projected image distances in the CCM image (Fig. 5(B)), anterior to posterior epithelium surface and anterior to posterior Bowman's membrane surface, are $d_E = (250 \pm 1)$ µm and $d_B = (84 \pm 1)$ µm, respectively. This results in an epithelial thickness of (46 ± 5) µm. The uncertainty was analytically calculated from trigonometric relations with the approximated single values uncertainties and assuming an undetermined corneal radius of curvature between 7.5 mm and infinity, which corresponds to

completely applanated. In the same way, the Bowman's membrane thickness is calculated to 15.3 μm with an uncertainty of at least ± 1.5 μm. For improvements the before mentioned software calibration and edge detection and automated line fits are necessary, making a post-process obsolete. Nevertheless, compared to other values of the epithelial thickness ranging from 42 μm to 55 μm [18–20], the determined value lies almost in the middle of this range. Also, the determined value of the Bowman's membrane thickness is in good agreement with values obtained by other methods, e.g. confocal microscopy through focusing [14] or using a sub-micrometer axial resolution OCT [7].
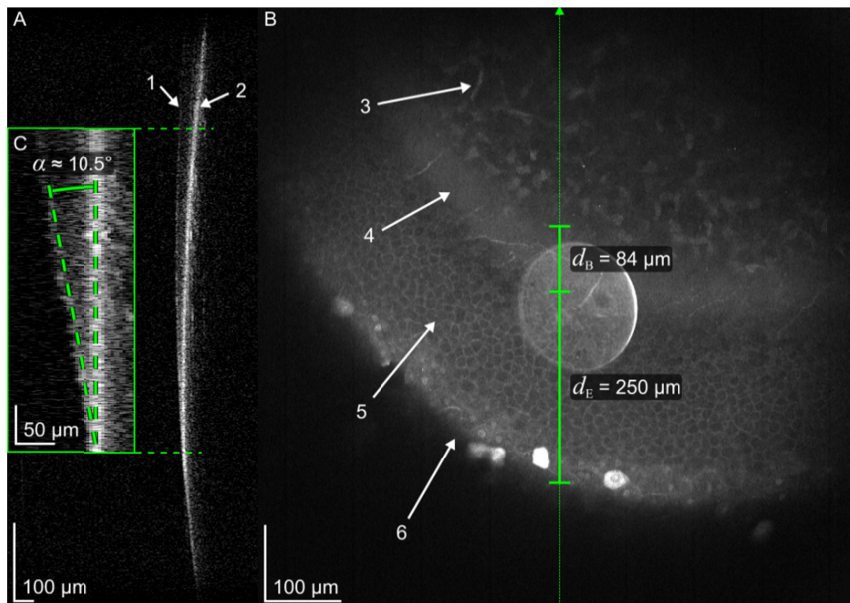

Fig. 5. Sagittal OCT (A) and CCM (B) image of an oblique section. A part of the OCT image was rectified (see text) and stretched to isotropic scaling (C) in order to measure the angle between the corneal surface (1) and CCM imaging plane (2). The CCM image shows the anterior stroma (3), the Bowman's membrane with the subbasal nerve plexus (4), the epithelium (5) and the superficial cells of the epithelium (6). The oblique imaging angle α and the projected layer distances d_E and d_B result in an epithelial thickness of 46 μm and a Bowman's membrane thickness of 15.3 μm.

4. Discussion and conclusions

The presented preliminary results demonstrate how CCM benefits from simultaneous OCT imaging. A variety of publications dealing with bimodal retinal imaging by means of SLO and OCT have been reported in the literature. The SLO is usually used to support the OCT imaging, e.g. for image stabilization purposes. To the best of our knowledge, this combination has not been reported in case of corneal imaging. In contrast to retinal imaging, the approach presented here utilizes OCT information to support CCM imaging instead. Thus, it is possible to assign any CCM image with its correct imaging depth and orientation. Furthermore, the possibility of detecting the corneal surface in the OCT image, even before the TomoCap touches the cornea and before it is visible in the actual CCM image, greatly simplifies the alignment procedure in the initial step of a subject examination. In this context, an additional perpendicular OCT scan line would allow to pre-align the CCM to a desired position, e.g. cornea's apex, and improve location-based diagnosis.

As a further substantial benefit, this system achieves an almost five times larger field of view while maintaining or even increasing the in-plane resolution depending on the

acquisition mode (HS or HR) used, but currently at the cost of a decreased framerate compared to the HRT/RCM 2.0 system.

The presented imaging method using CCM and OCT simultaneously is just an initial step, but it may be helpful in experimental as well as clinical usage upon further improvement and optimization. This includes e.g. (1) OCT reference arm adjustment, (2) elimination of parasitic lens reflections, (3) utilization of the full 2D scanning range in order to get rid of the obscured corners in the CCM images, (4) the calibration of optical path length to get flat imaging planes and (5) locally dependent intensity scaling. Furthermore, a verification of the thickness measurements by comparing to other techniques is necessary and phantom studies are recommended for that purpose. Additionally, the inhomogeneity of the cornea and its refractive index [21] must be taken into consideration in order to further increase the precision of corneal measurements. Finally, thorough evaluations in human studies will answer the question for usability and advantage compared to established systems. In conclusion, even though there are many challenges that have to be addressed in the future, our initial results can be pathbreaking for the development of an improved novel corneal diagnostic.

Funding

Acknowledgments

Disclosures

The authors declare that there are no conflicts of interest related to this article.

References

1. A. G. Podoleanu and D. A. Jackson, "Combined optical coherence tomograph and scanning laser ophthalmoscope," Electron. Lett. **34**(11), 1088–1090 (1998).
2. A. G. Podoleanu, G. M. Dobre, R. G. Cucu, R. Rosen, P. Garcia, J. Nieto, D. Will, R. Gentile, T. Muldoon, J. Walsh, L. A. Yannuzzi, Y. Fisher, D. Orlock, R. Weitz, J. A. Rogers, S. Dunne, and A. Boxer, "Combined multiplanar optical coherence tomography and confocal scanning ophthalmoscopy," J. Biomed. Opt. **9**(1), 86–93 (2004).
3. R. F. Guthoff, A. Zhivov, and O. Stachs, "In vivo confocal microscopy, an inner vision of the cornea - a major review," Clin. Exp. Ophthalmol. **37**(1), 100–117 (2009).
4. J. Stave, G. Zinser, G. Grümmer, and R. Guthoff, "Modified Heidelberg Retinal Tomograph HRT. Initial results of in vivo presentation of corneal structures," Ophthalmologe **99**(4), 276–280 (2002).
5. S. Bohn, K. Sperlich, S. Allgeier, A. Bartschat, R. Prakasam, K.-M. Reichert, H. Stolz, R. Guthoff, R. Mikut, B. Köhler, and O. Stachs, "Cellular in vivo 3D imaging of the cornea by confocal laser scanning microscopy," Biomed. Opt. Express **9**(6), 2511–2525 (2018).
6. R. M. Werkmeister, S. Sapeta, D. Schmidl, G. Garhöfer, G. Schmidinger, V. Aranha Dos Santos, G. C. Aschinger, I. Baumgartner, N. Pircher, F. Schwarzhans, A. Pantalon, H. Dua, and L. Schmetterer, "Ultrahigh-resolution OCT imaging of the human cornea," Biomed. Opt. Express **8**(2), 1221–1239 (2017).
7. K. Bizheva, B. Tan, B. MacLelan, O. Kralj, M. Hajialamdari, D. Hileeto, and L. Sorbara, "Sub-micrometer axial resolution OCT for in-vivo imaging of the cellular structure of healthy and keratoconic human corneas," Biomed. Opt. Express **8**(2), 800–812 (2017).
8. O. Stachs, K. Sperlich, S. Bohn, H. Stolz, and R. Guthoff, "Rostock Cornea Module 2.0 – a versatile extension for anterior segment imaging," Acta Ophthalmol. **95**, 2381 (2017).
9. A. Gullstrand, "Die Dioptrik des Auges," in Handbuch der Physiologischen Optik, 3rd ed., H. von Helmholtz, ed. (Verlag von Leopold Voss, 1909).
10. D. Z. Reinstein, T. J. Archer, M. Gobbe, R. H. Silverman, and D. J. Coleman, "Epithelial Thickness in the Normal Cornea: Three-dimensional Display With Artemis Very High-frequency Digital Ultrasound," J. Refract. Surg. **24**(6), 571–581 (2008).
11. J. Wang, J. Thomas, I. Cox, and A. Rollins, "Noncontact measurements of central corneal epithelial and flap thickness after laser in situ keratomileusis," Invest. Ophthalmol. Vis. Sci. **45**(6), 1812–1816 (2004).

12. C. Wirbelauer and D. T. Pham, "Monitoring corneal structures with slitlamp-adapted optical coherence tomography in laser in situ keratomileusis," J. Cataract Refract. Surg. **30**(9), 1851–1860 (2004).
13. S. Haque, D. Fonn, T. Simpson, and L. Jones, "Corneal and epithelial thickness changes after 4 weeks of overnight corneal refractive therapy lens wear, measured with optical coherence tomography," Eye Contact Lens **30**(4), 189–206 (2004).
14. H. F. Li, W. M. Petroll, T. Møller-Pedersen, J. K. Maurer, H. D. Cavanagh, and J. V. Jester, "Epithelial and corneal thickness measurements by in vivo confocal microscopy through focusing (CMTF)," Curr. Eye Res. **16**(3), 214–221 (1997).
15. W. M. Petroll, M. Weaver, S. Vaidya, J. P. McCulley, and H. D. Cavanagh, "Quantitative 3-Dimensional Corneal Imaging in Vivo Using a Modified HRT-RCM Confocal Microscope," Cornea **32**(4), e36–e43 (2013).
16. M. J. Doughty and M. L. Zaman, "Human Corneal Thickness and Its Impact on Intraocular Pressure Measures: A Review and Meta-analysis Approach," Surv. Ophthalmol. **44**(5), 367–408 (2000).
17. J. Ho, D. P. E. Castro, L. C. Castro, Y. Chen, J. Liu, C. Mattox, C. Krishnan, J. G. Fujimoto, J. S. Schuman, and J. S. Duker, "Clinical Assessment of Mirror Artifacts in Spectral-Domain Optical Coherence Tomography," Invest. Ophthalmol. Vis. Sci. **51**(7), 3714–3720 (2010).
18. K. M. Rocha, C. E. Perez-Straziota, R. D. Stulting, and J. B. Randleman, "SD-OCT Analysis of Regional Epithelial Thickness Profiles in Keratoconus, Postoperative Corneal Ectasia, and Normal Eyes," J. Refract. Surg. **29**(3), 173–179 (2013).
19. S. Sin and T. L. Simpson, "The repeatability of corneal and corneal epithelial thickness measurements using optical coherence tomography," Optom. Vis. Sci. **83**(6), 360–365 (2006).
20. J. G. Pérez, J. M. G. Méijome, I. Jalbert, D. F. Sweeney, and P. Erickson, "Corneal Epithelial Thinning Profile Induced by Long-Term Wear of Hydrogel Lenses," Cornea **22**(4), 304–307 (2003).
21. S. Patel, J. Marshall, and F. W. Fitzke 3rd, "Refractive index of the human corneal epithelium and stroma," J. Refract. Surg. **11**(2), 100–105 (1995).

Multiwavelength confocal laser scanning microscopy of the cornea

Sebastian Bohn, Karsten Sperlich, Thomas Stahnke, Melanie Schünemann, Heinrich Stolz, Rudolf F. Guthoff, and Oliver Stachs

Copyright notice

Multiwavelength confocal laser scanning microscopy of the cornea

SEBASTIAN BOHN,[1,2,3,4,5] **KARSTEN SPERLICH,**[1,3,4,6] **THOMAS STAHNKE,**[1,3] **MELANIE SCHÜNEMANN,**[1,3] **HEINRICH STOLZ,**[2] **RUDOLF F. GUTHOFF,**[1,3] **AND OLIVER STACHS**[1,3]

[1]*Department of Ophthalmology, Rostock University Medical Center, 18057 Rostock, Germany*
[2]*Institute of Physics, University Rostock, 18059 Rostock, Germany*
[3]*Department of Life, Light & Matter, University Rostock, 18051 Rostock, Germany*
[4]*Co-first authors with equal contribution*
[5]*sebastian.bohn@uni-rostock.de*
[6]*karsten.sperlich@uni-rostock.de*

Abstract: Confocal reflectance microscopy has demonstrated the ability to produce *in vivo* images of corneal tissue with sufficient cellular resolution to diagnose a broad range of corneal conditions. To investigate the spectral behavior of corneal reflectance imaging, a modified laser ophthalmoscope was used. Imaging was performed *in vivo* on a human cornea as well as *ex vivo* on porcine and lamb corneae. Various corneal layers were imaged at the wavelengths 488 nm, 518 nm, and 815 nm and compared regarding image quality and differences in the depicted structures. Besides the wavelength- and depth-dependent scattering background, which impairs the image quality, a varying spectral reflectance of certain structures could be observed. Based on the obtained results, this paper emphasizes the importance of choosing the appropriate light source for corneal imaging. For the examination of the epithelial layers and the endothelium, shorter wavelengths should be preferred. In the remaining layers, longer wavelength light has the advantage of less scattering loss and a potentially higher subject compliance.

1. Introduction

To date, clinical and scientific investigations regarding corneal confocal laser scanning microscopy are performed mainly with the combination of the Heidelberg Retina Tomograph (HRT), which is a confocal scanning laser ophthalmoscope (SLO), and the Rostock Cornea Module (RCM; both Heidelberg Engineering GmbH, Heidelberg, Germany) [1,2]. Hence, most images were captured using a red laser with a wavelength of 670 nm. Besides the HRT/RCM system, there is also the Confoscan (NIDEK, Gamagori, Japan), which is a slit-scanning confocal microscope using a white halogen lamp. Although the HRT/RCM system generally generates better corneal images due to the two-dimensional confocality, the Confoscan provides better endothelial images [3,4] even though it is only confocal in one direction. This fact already indicates the influence of different light sources on imaging and underlines the need for a wavelength-dependent study.

Currently, research is conducted on new corneal imaging devices that achieve cellular resolution. These devices may use other modalities, light sources, and thus different wavelengths than 670 nm. For example, asymmetric fundus retroillumination [5] and various optical coherence tomography (OCT) methods including spectral domain OCT [6], ultrahigh resolution OCT [7], Gabor-domain OCT [8], full-field OCT [9–12] and curved-field OCT [13] were investigated. These methods usually operate in the near-infrared spectrum [6–11,13], but also the visible spectrum [12]. In order to ensure comparability between the existing and new technologies, the spectral reflection dependence on different cellular corneal structures must be determined.

Although the absorption characteristic through the full cornea is well investigated [14], the spectrally dependent reflectance of different cellular structures is yet unknown. Due to

wavelength-dependent scattering, more light is scattered in all directions at shorter wavelengths [15], thus reducing the amount of detected light from the focused structure. This effect integrates with the depth. Consequently, the detector gain must be increased to obtain a sufficiently strong signal from structures at deeper layers. This, in turn, leads to a decreased signal-to-noise ratio and an amplification of unwanted, disruptive backscattering of optical surfaces and corneal layers outside the focus. Although the latter effect is quite small due to confocality, all of these effects could add up to a diffuse background that scales with the imaging depth. However, the optical resolution is inversely proportional to the wavelength, too [16]. As a result, longer wavelengths, which provide deeper penetration and less scattering, come at the expense of optical resolution. Besides these effects, reflectance images captured at different wavelengths may potentially reveal different cellular structures.

It is known, e.g. from dermatology, that the backscatter from the inter- and intracellular structures can vary with wavelength, size, geometry, and refractive index of the scattering structure [17,18]. Thus, by acquiring reflectance images from multiple wavelengths, it could be possible to extract wavelength-dependent information. Therefore, the aim of this work is to investigate the influence of different wavelengths on corneal imaging.

2.   Materials and methods

To acquire images of the cornea at different wavelengths, the SPECTRALIS platform (Heidelberg Engineering GmbH, Heidelberg, Germany), a confocal scanning laser ophthalmoscope with three distinct laser wavelengths (blue – 488 nm, green – 518 nm, near-infrared – 815 nm), was used in conjunction with a custom-built objective module. The objective module is a redesigned version of the RCM and was previously presented as RCM 2.0 in combination with the HRT [19] as well as with the SPECTRALIS [20]. The RCM 2.0 was adapted to the SLO to shift the focal plane from the retina to the cornea and to increase the in-plane resolution. Furthermore, a piezo actuator was implemented to control the focal plane within the cornea. For measurements, a sterile cap was used to contact the cornea. To reduce surface reflections, a carbomer gel (Vidisic; Bausch & Lomb / Dr. Mann Pharma, Berlin, Germany) was applied as an immersion medium between the objective lens and contact cap as well as between the cap and the cornea. Since this gel is a tear substitute, it provides the same refractive index change between *ex vivo* and *in vivo* measurements. The new design of the RCM 2.0 enabled a fixed position of the contact cap during focal plane changes. Nevertheless, it was still possible to adjust the position of the contact cap before tissue imaging. This is important in order to capture the largest possible cornea stack.

The combination of SPECTRALIS and RCM 2.0 is shown in Fig. 1(A). Additionally, Fig. 1(B) shows a simplified schematic of a confocal SLO with three laser diodes of different wavelengths. These are directed on the same optical path with dichroic mirrors and their back reflected signals can be detected sequentially with a detector.

The obtained magnification and thus the field of view (FOV) depends on the scan angle of the SLO, the distance between the optics of RCM 2.0 and SLO, as well as slightly on the selected wavelength. Exemplifying this, Fig. 2 compares images taken with the HRT and SPECTRALIS, each in conjunction with the RCM 2.0. While the HRT captured images demonstrate a FOV of 350×350 µm^2, the images taken with the SPECTRALIS have a FOV of 710×710 µm^2 at the near-infrared wavelength of 850 nm. This difference in FOV is mainly caused by the larger scan angle of the SPECTRALIS with 30° compared to the HRT with 15°. The magnification of every optical setup and wavelength used was measured. Consequently, all images were scaled accordingly. Since the objective lens (Achroplan 63x/0.95 W; Zeiss, Jena, Germany) is not optimized for the wavelengths of the SPECTRALIS platform, its images show a central back reflection. While the size of the back reflection depends on the distance between RCM 2.0 and SPECTRALIS as well as the selected wavelength, the intensity of the back reflection furthermore depends on the illuminance and detector gain. In the example of Fig. 3, the intensity of the back
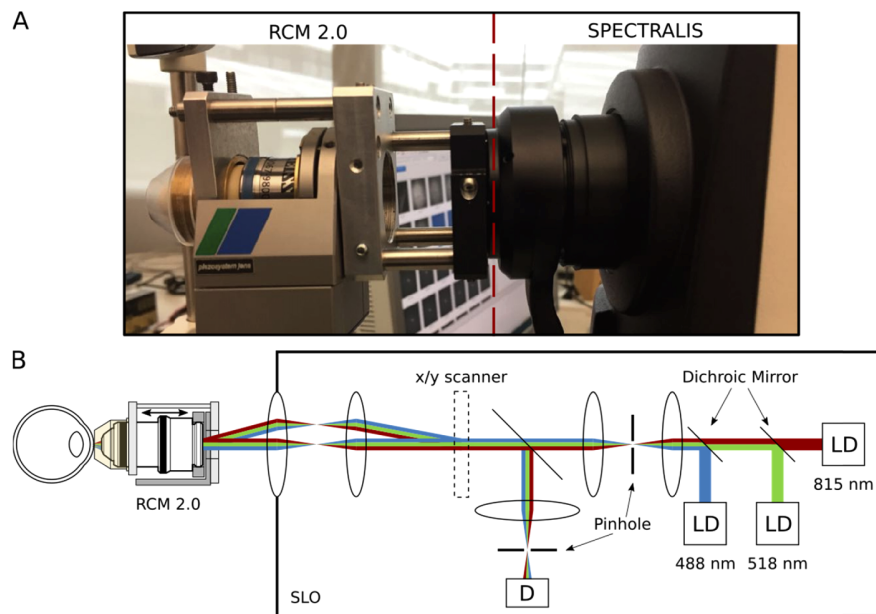
Fig. 1. A: The RCM 2.0 in conjunction with the SPECTRALIS platform (dashed line separates both components). B: Simplified schematic of a confocal SLO with three laser diodes operating at different wavelengths (LD – laser diode, D – detector).

reflection is clearly visible for 488 nm as well as 518 nm and is vanishingly low at 815 nm. With the RCM 2.0, a radiant power of 62.8 μw, 43.3 μW, and 15.2 μW at 488 nm, 518 nm, and 815 nm respectively was measured at maximum laser power. This results in a corneal irradiance of less than 0.014 W/cm^2 and a retinal irradiance of less than 0.003 W/cm^2 . These values are below the limits of Group 1 ophthalmic instruments of the safety standard DIN EN ISO 15004-2. The actual radiant power used in the *in vivo* measurements was 26.6 μW, 22.2 μW, and 15.2 μW at 488 nm, 518 nm, and 815 nm, respectively.

In vivo measurements were performed on four subjects. Since one subject already underwent numerous eye examinations of different kinds in the past, confirming a healthy eye, the images presented in this paper are from this 51-year-old male subject. However, the other three subjects claimed to have no eye problems and are assumed to have healthy eyes as well. The study was conducted in accordance with the Declaration of Helsinki and it was explained in detail to the subjects. Informed consent was obtained before any investigative procedures were conducted. In addition, the endothelium of the human subject was imaged with a specular microscope (EM-4000; Tomey GmbH, Nürnberg, Germany) and compared to the confocal images. Finally, *ex vivo* measurements were performed on several porcine and lamb eyes. In the case of the human cornea, images of the epithelium, subbasal nerve plexus (SNP), stroma, and endothelium were recorded and compared at all three wavelengths. Due to eye movements, the images at the three different wavelengths could not be captured at the same lateral position in the cornea. Images of the porcine and lamb eyes were taken from the epithelium, stroma, and endothelium at the blue and near-infrared wavelengths less than 12 h after enucleation and compared to the *in vivo* images of the human cornea.

For a direct comparison between images captured at different wavelengths, it is important to adjust the histogram to the full intensity scale. Otherwise misleading conclusions may be drawn. In the case of the *in vivo* measurements, subimages showing the relevant structures were selected,
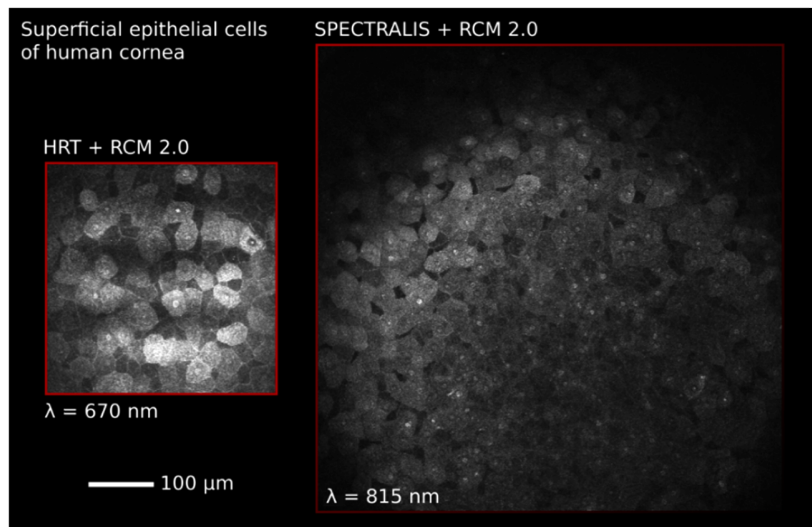
Fig. 2. Comparison of the HRT + RCM 2.0 and SPECTRALIS + RCM 2.0 combinations showing superficial cells of a human cornea.
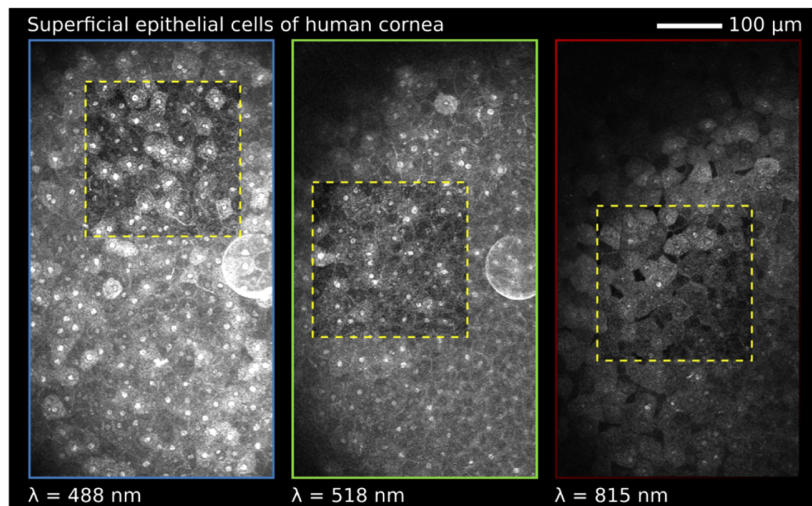

Fig. 3. Comparison of *in vivo* human cornea images of superficial epithelial cells acquired at three distinct wavelengths as indicated. The histograms of the subimages in the yellow dashed squares were adjusted to the full intensity range for a consistent comparison of the image quality.

the histograms were stretched so that the entire intensity range was used for the cell structures and finally presented as an inset in the original image. In the case of the *ex vivo* figures, only the histogram stretched subimages are presented.

No auto-brightness functionality was used for all image acquisition and the detector gain was changed manually if necessary. Since the incorporated scanning laser ophthalmoscope is a commercial device, some wavelength-dependent parameters such as the spectral transmittance of the optics or the quantum efficiency of the detector are unknown and hence, comparisons of

signal strengths between wavelengths are difficult to obtain. Therefore, the focus of the study was a dedicated view on the visibility of different corneal structures at the respective wavelengths. Then it was compared whether these corneal structures look similar or different at the specific wavelengths.

3. Results

3.1. In vivo measurements of a human cornea

In general, imaging could be performed at all investigated wavelengths and species. Depending on the wavelength, there are not only differences in the image quality but also in the reflectance of certain structures.

Figure 3 shows the cell borders, cytoplasm, and nuclei of the human superficial epithelial cells, which appear more prominent using the blue or green compared to the near-infrared wavelength. Particularly the blue and green wavelengths reveal certain superficial cells in which the cytoplasm reflects much more than others. Most cell nuclei are visible at the blue wavelength. Especially in the area around the central back reflection, many nuclei are revealed that are invisible at the other two wavelengths. At 815 nm, the cytoplasm and cell borders of the superficial cells have a rather uniform, homogeneous reflectance. This makes it more difficult to distinguish adjacent cells. However, slightly deeper in the epithelium, the wing cells in Fig. 4 show no discernible differences between the three wavelengths. Cell borders are brighter than the cytoplasm. None of the wavelengths reveals cell nuclei.
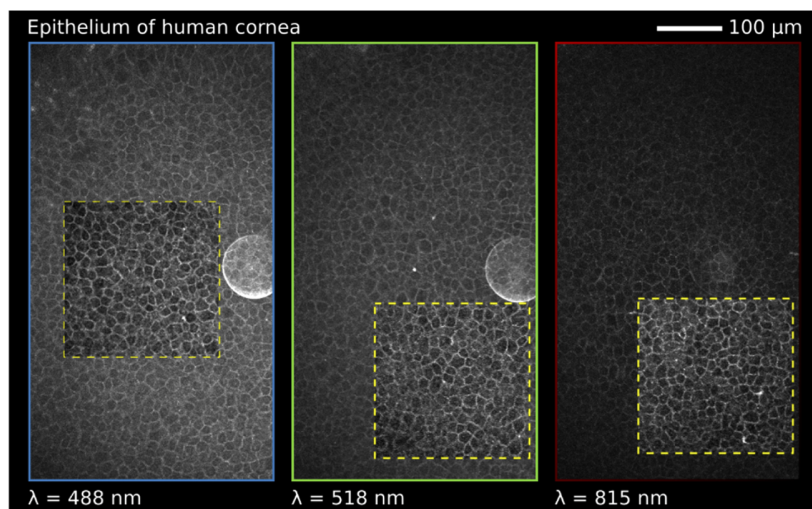

Fig. 4. Comparison of *in vivo* human cornea images of epithelium acquired at three distinct wavelengths as indicated. The histograms of the subimages in the yellow dashed squares were adjusted to the full intensity range for a consistent comparison of the image quality.

As Fig. 5 and Fig. 6 demonstrate, the influence of scattering at lower wavelengths increases at deeper layers, such as the SNP and the anterior stroma. In both cases, the images at 488 nm and 518 nm have a stronger diffuse background than at 815 nm. Nevertheless, at all wavelengths, nerve fibers and keratocyte nuclei are imaged clearly and sharply.

No diffuse background is visible in the endothelium in Fig. 7, because the relatively highly reflective cell structures are more widespread. Still, an intensity loss due to the scattering was present, so that the detector gain had to be increased. Also, the wavelength-dependent endothelial reflectance is very different compared to the previous corneal layers. The hexagonal cell structure
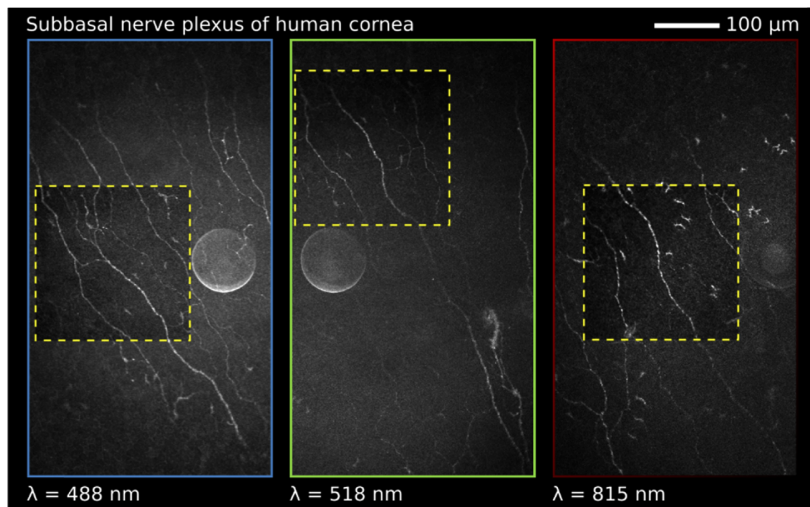
Fig. 5. Comparison of *in vivo* human cornea images of the subbasal nerve plexus acquired with three distinct wavelengths as indicated. The histograms of the subimages in the yellow dashed squares were adjusted to the full intensity range for a consistent comparison of the image quality.
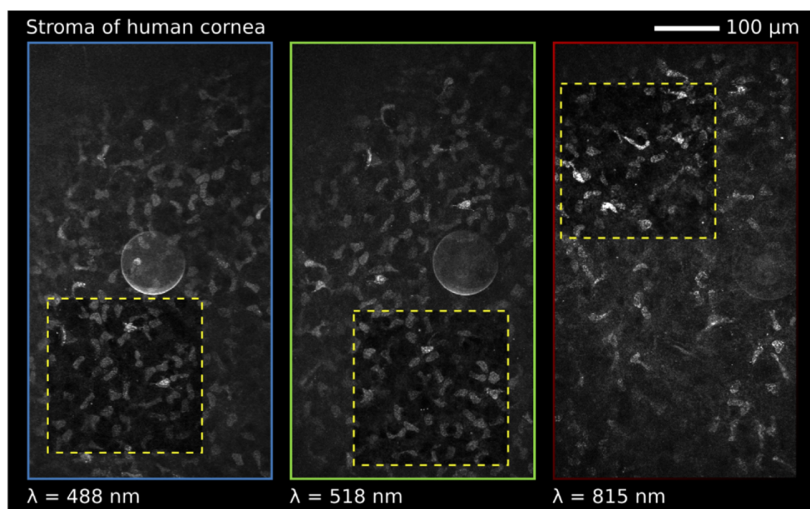

Fig. 6. Comparison of *in vivo* human cornea images of anterior stroma acquired at three distinct wavelengths as indicated. The histograms of the subimages in the yellow dashed squares were adjusted to the full intensity range for a consistent comparison of the image quality.

can be resolved at the blue and green wavelengths, but not using the near-infrared light. Contrary to the epithelial cells, the cell borders of the endothelium appear to be darker than the cytoplasm. While at 488 nm and 518 nm the endothelial structure is equally well visible, at 815 nm cells can only be seen sporadically. In addition, some endothelial cell nuclei appear as bright spots at the blue and green wavelengths.
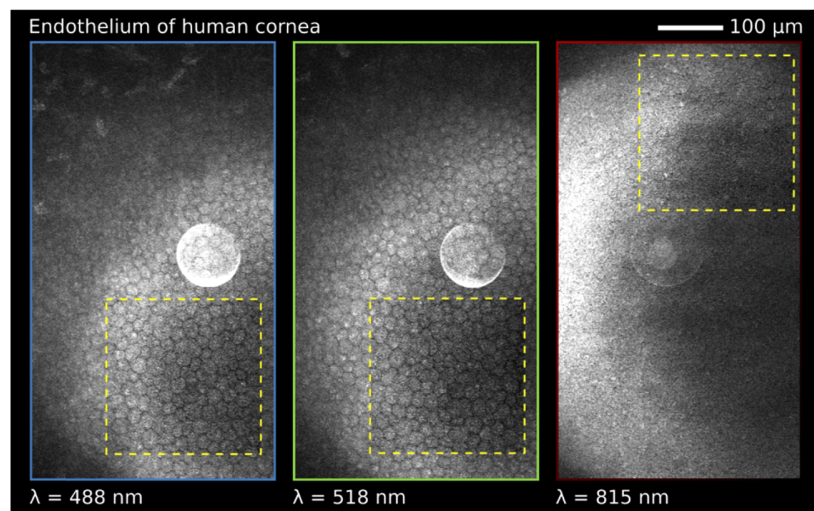
Fig. 7. Comparison of *in vivo* human cornea images of endothelium acquired at three distinct wavelengths as indicated. The histograms of the subimages in the yellow dashed squares were adjusted to the full intensity range for a consistent comparison of the image quality.

Figure 8 compares specular and confocal microscopy of the endothelium. The latter shows sharper cell structures at the blue and green wavelengths.
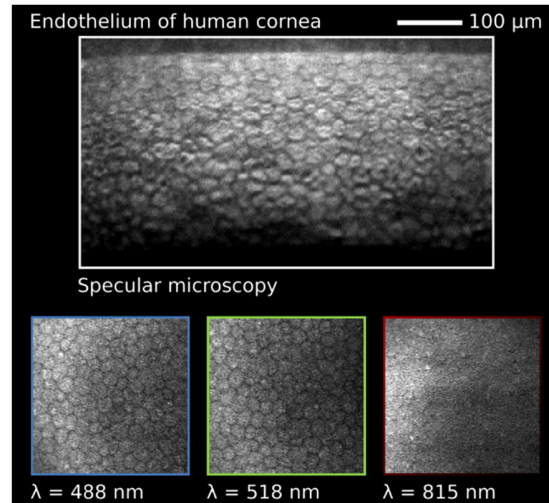

Fig. 8. Comparison of *in vivo* human cornea images of endothelium captured with specular and confocal microscopy at three different wavelengths. The histogram of each image is stretched for better comparison.

3.2. Ex vivo measurements of porcine and lamb corneae

Since the previous results at the blue and green wavelengths revealed no substantial difference, *in vivo* images of the human cornea are compared in the following with *ex vivo* images of porcine

and lamb corneae only at 488 nm and 815 nm. Interestingly, the superficial cells of animal corneae in Fig. 9 show different behavior than in the human images. In the case of the porcine cornea, cell nuclei reflect similarly at both wavelengths. In the case of the lamb cornea, the nuclei reflect somewhat more strongly at 815 nm and thus show the opposite behavior compared to the human cornea. Furthermore, the cytoplasm of the porcine and lamb cornea reflects at the near-infrared wavelength with a different structure, in the latter also considerably stronger. However, the cell borders of all three species are best visible at 488 nm. Please note, differences in backscattering characteristics may also be induced by the post mortem time in case of the animal corneae.
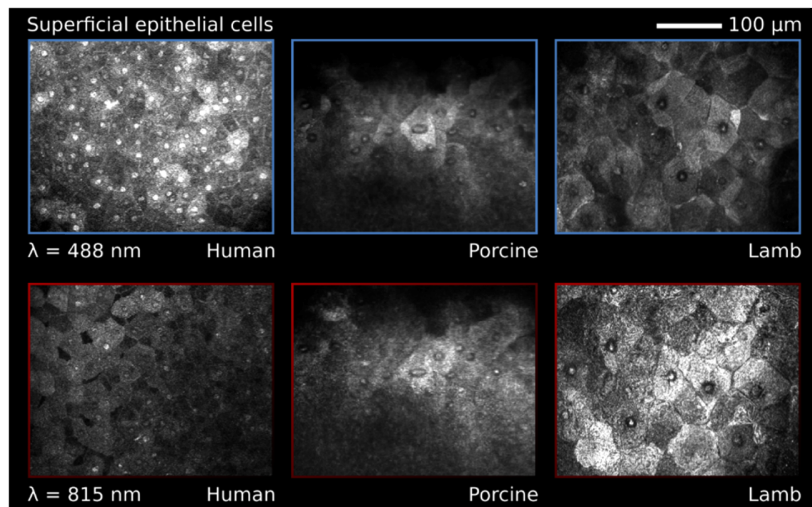

Fig. 9. *In vivo* (human) and *ex vivo* (porcine, lamb) images of superficial epithelial cells acquired at blue and near-infrared wavelengths.
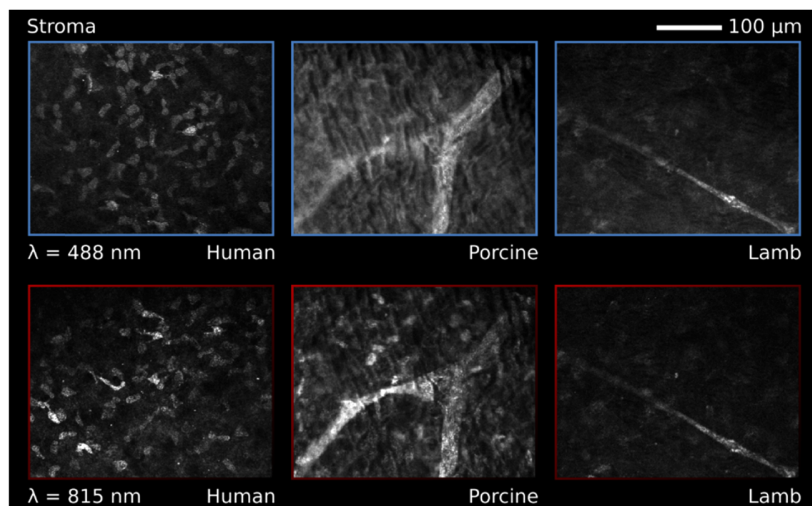

Fig. 10. *In vivo* (human) and *ex vivo* (porcine, lamb) images of t stroma acquired at blue and near-infrared wavelengths.

Figure 10 illustrates that the scattering in the stroma is noticeable for all species at the blue wavelength. In the animal corneae, especially in the porcine, the cell density of keratocytes seems to be lower than in the human cornea. This might be related to the advanced age of the animals [21,22]. While at 815 nm keratocyte nuclei and stromal nerve of the porcine cornea are more visible, keratocyte nuclei of the lamb cornea are only weakly visible at both wavelengths and the visibility of the stromal nerve is rather similar.

The endothelium in Fig. 11 also shows substantial differences between 488 nm and 815 nm in the porcine and lamb cornea. In the human and porcine cornea, some endothelial cell nuclei appear as bright spots at 488 nm. In the lamb cornea these nuclei are not visible. While at 815 nm the entire endothelial structure including nuclei is almost invisible in the human cornea, it is visible in case of the porcine and lamb cornea and the nuclei appear darkened.
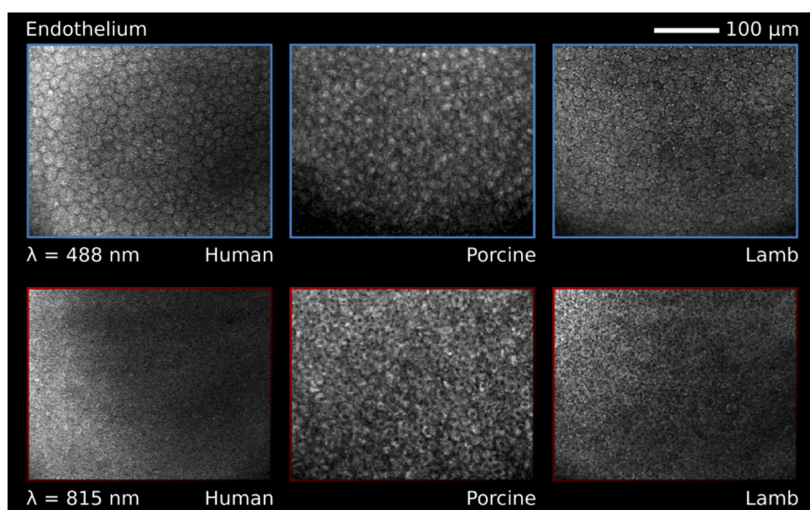

Fig. 11. *In vivo* (human) and *ex vivo* (porcine, lamb) images of endothelium acquired at blue and near-infrared wavelengths.

4.   Discussion and conclusions

This work presents for the first time an investigation of the wavelength-dependent reflectance of corneal tissues. The presented images show that most differences in image quality can be attributed to a depth- and wavelength-dependent scattering background. Tissue and cell characteristic backscattering patterns (intra- and extracellular) are little to not wavelength specific. From the subbasal nerve plexus onwards, the negative effects in the form of a diffuse background become apparent at shorter wavelengths. This effect increases for shorter wavelengths the deeper the imaging is performed in the cornea. However, this diffuse background is most pronounced in the stroma among all species. In the endothelium, this effect is only noticeable in images of the porcine cornea. It is assumed that this is due to the advanced time after the eye was enucleated and therefore it is generally more opaque. Furthermore, in the case of the human and lamb cornea, the visible structures in the endothelium are more prominent at the shorter wavelengths than at the near-infrared.

No effect of scattering is observed in the epithelium. This is due to the fact that scattering background is depth-dependent and the epithelium is the top layer of the cornea. The images of the wing cells presented in this manuscript do not reveal differences in imaging quality or structure at the three selected wavelengths. Superficial cells, however, show structural differences

depending on the wavelength and on the investigated species. In the human cornea, the nuclei and cytoplasm are most reflective at the short wavelengths. The mature superficial cells, which are about to desquamate into the tear film, exhibit a stronger reflection because they have more microvilli than the younger cells [23]. In the lamb cornea, on the other hand, the opposite behavior was observed. This leads to the assumption that not every mammal eye is suitable for comparison to the human one. It is supposed that the desquamating cells change their protein pattern variously depending on the species, which leads to differences in reflectance [24,25]. Nevertheless, further investigations are needed to confirm this statement. Despite the aforementioned differences, in all three species, it is shown that the superficial epithelial cell borders are best defined at shorter wavelengths and thus individual cells are best distinguished.

In comparison to other imaging techniques, it is apparent that, for example, OCT methods using a NIR light source [6–11,13] are capable to capture images of the SNP and stroma with almost similar quality as the results presented here. However, the epithelial images do not show cell structures as clearly as the results obtained by corneal confocal microscopy in this paper. Since the previously referenced methods are non-contact methods, images of superficial epithelial cells are currently impossible due to the strong surface reflection. Interestingly, although the endothelial cells are clearly visible in the NIR with OCT methods we were barely able to image the human endothelium using 815 nm light. When using OCT in the visible spectrum [12], clear cell structures are visible in all corneal layers of the rat eye. Since a water immersion objective was used, superficial cells were imaged, too [12]. The presented corneal confocal microscopy at shorter wavelengths, provides endothelial images with clear cell structures, offering an alternative to the specular microscopy, which is still the current gold standard for endothelial imaging. In addition to the wavelength, the scattering geometry also has an influence on imaging, as shown by the asymmetric fundus retroillumination [5]. While backward scattering occurs in the confocal microscopy applied in this paper, retroillumination utilizes the spatially dependent transmittance revealing the cell structures. Nerve fibers in the SNP and stroma as well as the endothelium are visible at a large FOV. Additionally, the surface layers of the epithelium can be imaged despite the non-contact method. Nevertheless, the epithelial and endothelial images of retroillumination do not show the same level of detail as the images obtained with corneal confocal microscopy.

This paper demonstrates the importance of choosing the right wavelength or wavelength spectrum for confocal laser scanning microscopy of certain corneal structures. In doing so, not only the depth-dependent and wavelength-dependent scattering background should be considered, but also the behavior in the respective layer. Especially when developing new devices that use either a broadband light source or several wavelengths simultaneously, this should be decided depending on the area of application. If the main focus is on e.g. ocular surface diseases, shorter wavelengths in the visible spectrum should be preferred. For imaging the entire cornea, the wavelength should be shifted so far into the red that the scattering no longer has a negative influence on image quality. In case only the endothelium is going to be considered, also shorter wavelengths are more suitable. The optimal solution would be a multimodal instrument, which provides several wavelengths to choose from, depending on the examined corneal layer.

A second rationale for wavelength-dependent imaging is as follows. Backscattering from inter- and intracellular structures can vary with wavelength. In the translation, by acquiring reflectance images from multiple wavelengths it could be possible to extract wavelength-dependent information that could correlate to tissue and cell properties. For example, Wang et al. were able to characterize lymphocytes in skin [26] at 785, 810, and 850 nm. Surprisingly, our corneal imaging over the large wavelength range of nearly 350 nm shows only minor variations in the tissue-dependent backscattering patterns. Primarily, this implies that the choice of wavelength is of secondary importance, with the exception of the endothelium and epithelium. Whether multiwavelength imaging offers further diagnostic values, especially on the diseased corneae, is subject to future research.

One effect that has not yet been discussed is the effect of wavelength on the subject's compliance. Taken into consideration that light from the visible spectrum could distract or glare the subject, an impairment of the *in vivo* examination is conceivable. Following this aspect, near-infrared light has the advantage that it is invisible to the human eye and should avoid glare induced eye movements.

The presented results were generated with only three distinct wavelengths. Thus, no continuous wavelength dependence of the image quality or depicted corneal structures is provided. Despite this, they do demonstrate the importance of choosing the right light source to obtain the best image quality in the different layers of the cornea. In order to further expand this research, additional wavelengths, broadband light sources, or tunable lasers could be included in such a study. In addition, more subjects with a known eye health status should be examined in order to confirm the reproducibility of the results shown here and to exclude any subject dependent differences. However, it should be noted that the *ex vivo* measurements were performed on several porcine and lamb eyes, and no differences were found within one species.

Disclosures

The authors declare that there are no conflicts of interest related to this article.

References

1. R. F. Guthoff, A. Zhivov, and O. Stachs, "In vivo confocal microscopy, an inner vision of the cornea - a major review," Clin. Exp. Ophthalmol. **37**(1), 100–117 (2009)..
2. O. Stachs, R. F. Guthoff, and S. Aumann, "In Vivo Confocal Scanning Laser Microscopy," in *High Resolution Imaging in Microscopy and Ophthalmology*, J. F. Bille, ed. (Springer International Publishing, 2019).
3. N. Bailly, Z. A. Sherif, U. Pleyer, and P. Rieck, "Confocal Microscopy in Corneal Dystrophies: A Comparison between Confocal Slit Scanning (ConfoScan P2) and Laser Scanning Microscopy (Rostock Cornea Modul-HRT II)," Klin. Monatsbl. Augenheilkd. **223**(9), 735–742 (2006)..
4. J. P. Szaflik, "Comparison of in vivo confocal microscopy of human cornea by white light scanning slit and laser scanning systems," Cornea **26**(4), 438–445 (2007)..
5. T. D. Weber and J. Mertz, "In vivo corneal and lenticular microscopy with asymmetric fundus retroillumination," Biomed. Opt. Express **11**(6), 3263–3273 (2020)..
6. B. Tan, Z. Hosseinaee, L. Han, O. Kralj, L. Sorbara, and K. Bizheva, "250 kHz, 1.5 µm resolution SD-OCT for in-vivo cellular imaging of the human cornea," Biomed. Opt. Express **9**(12), 6569–6583 (2018)..
7. X. Yao, K. Devarajan, R. M. Werkmeister, V. A. dos Santos, M. Ang, A. Kuo, D. W. K. Wong, J. Chua, B. Tan, V. A. Barathi, and L. Schmetterer, "In vivo corneal endothelium imaging using ultrahigh resolution OCT," Biomed. Opt. Express **10**(11), 5675–5686 (2019)..
8. C. Canavesi, A. Cogliati, A. Mietus, Y. Qi, J. Schallek, J. P. Rolland, and H. B. Hindman, "In vivo imaging of corneal nerves and cellular structures in mice with Gabor-domain optical coherence microscopy," Biomed. Opt. Express **11**(2), 711–724 (2020)..
9. V. Mazlin, P. Xiao, J. Scholler, K. Grieve, K. Irsch, J.-A. Sahel, M. Fink, and C. Boccare, "Ultra-High Resolution Full-Field OCT (FFOCT) for Cornea and Retina," in *Imaging and Applied Optics 2018 (3D, AO, AIO, COSI, DH, IS, LACSEA, LS&C, MATH, pcAOP)*, OSA Technical Digest (Optical Society of America, 2018), paper IM3B.1.
10. V. Mazlin, P. Xiao, J. Scholler, K. Irsch, K. Grieve, M. Fink, and C. Boccare, "Real-time, non-contact, cellular imaging and angiography of human cornea and limbus with common-path Full-field/SDOCT," Nat. Commun. **11**(1), 1868 (2020)..
11. E. Auksorius, D. Borycki, P. Stremplewski, K. Liżewski, S. Tomczewski, P. Niedźwiedziuk, B. L. Sikorski, and M. Wojtkowski, "In vivo imaging of the human cornea with high-speed and high-resolution Fourier-domain full-field optical coherence tomography," Biomed. Opt. Express **11**(5), 2849–2865 (2020)..

12. Y. Chen, C. Tsai, Y. Chiu, T. Hsu, L. W. Chen, W. Chen, and S. Huang, "En Face and Cross-sectional Corneal Tomograms Using Sub-micron spatial resolution Optical Coherence Tomography," Sci. Rep. **8**(1), 14349 (2018)..

13. V. Mazlin, K. Irsch, M. Paques, M. Fink, and A. C. Boccara, "Curved-field optical coherence tomography: large-field imaging of human corneal cells and nerves," arXiv preprint arXiv:2004.01016 (2020).

14. G. K. Lang and G. E. Lang, *Augenheilkunde Essentials* (Georg Thieme Verlag, 2015), Chap. 1.

15. H. Niedrig, *Optik – Wellen- und Teilchenoptik* (De Gruyter, 2004), Chap. 3.

16. H. Niedrig, *Optik – Wellen- und Teilchenoptik* (De Gruyter, 2004), Chap. 1.

17. M. M. Rajadhyaksha, S. González, and J. M. Zavislan, "Detectability of contrast agents for confocal reflectance imaging of skin and microcirculation," J. Biomed. Opt. **9**(2), 323–331 (2004)..

18. V. Backman, R. S. Gurjar, L. T. Perelman, V. Gopal, M. Kalashnikov, K. Badizadegan, A. Wax, I. Georgakoudi, M. G. Mueller, C. W. Boone, I. Itzkan, R. R. Dasari, and M. S. Feld, "Imaging and measurement of cell structure and organization with submicron accuracy using light scattering spectroscopy," Proc. SPIE **4613**, 101–110 (2002)..

19. S. Bohn, K. Sperlich, S. Allgeier, A. Bartschat, R. Prakasam, K.-M. Reichert, H. Stolz, R. Guthoff, R. Mikut, B. Köhler, and O. Stachs, "Cellular in vivo 3D imaging of the cornea by confocal laser scanning microscopy," Biomed. Opt. Express **9**(6), 2511–2525 (2018)..

20. S. Bohn, K. Sperlich, H. Stolz, R. F. Guthoff, and O. Stachs, "In vivo corneal confocal microscopy aided by optical coherence tomography," Biomed. Opt. Express **10**(5), 2580–2587 (2019).

21. J. B. Berlau, H.-H. Becker, J. Stave, C. Oriwol, and R. F. Guthoff, "Depth and age-dependent distribution of keratocytes in healthy human corneas: a study using scanning-slit confocal microscopy in vivo," J. Cataract Refractive Surg. **28**(4), 611–616 (2002)..

22. T. Zheng, Q. Le, J. Hong, and J. Xu, "Comparison of human corneal cell density by age and corneal location: an in vivo confocal microscopy study," BMC Ophthalmol. **16**(1), 109 (2016)..

23. R. R. Pfister, "The Normal Surface of Corneal Epithelium: A Scanning Electron Microscopic Study," Invest. Ophthalmol. Vis. Sci. **12**(9), 654–668 (1973).

24. W. Chen, J. Hu, Z. Zhang, L. Chen, H. Xie, N. Dong, Y. Chen, and Z. Liu, "Localization and Expression of Zonula Occludins-1 in the Rabbit Corneal Epithelium following Exposure to Benzalkonium Chloride," PLoS One **7**(7), e40893 (2012)..

25. A. R. Parrish, "The impact of aging on epithelial barriers," Tissue Barriers **5**(4), e1343172 (2017)..

26. Z. Wang, "Multiwavelength reflectance confocal microscopy for immune cell identification," Thesis (Ph. D.), University of Rochester (Institute of Optics, 2008).

In vivo Histology of the Cornea – from the "Rostock Cornea Module" to the "Rostock Electronic Slit Lamp" – a Clinical "Proof of Concept" Study

Sebastian Bohn, Thomas Stahnke, Karsten Sperlich, Stephan J. Linke,
Sanaz Farrokhi, Maren Klemm, Stephan Allgeier, Bernd Köhler, Klaus-Martin
Reichert, Martin Witt, Oliver Stachs, and Rudolf F. Guthoff

Copyright notice

In vivo Histology of the Cornea – from the "Rostock Cornea Module" to the "Rostock Electronic Slit Lamp" – a Clinical "Proof of Concept" Study

In-vivo-Histologie der Hornhaut – vom „Rostocker Cornea Modul" zur „Rostocker Elektronischen Spaltlampe" – eine klinische „Proof-of-Concept"-Studie

Authors

Sebastian Bohn[1,2*], Thomas Stahnke[1,2*] ⓘ, Karsten Sperlich[1,2], Stephan J. Linke[3,4], Sanaz Farrokhi[3], Maren Klemm[3], Stephan Allgeier[5] ⓘ, Bernd Köhler[5] ⓘ, Klaus-Martin Reichert[5], Martin Witt[6], Oliver Stachs[1,2], Rudolf F. Guthoff[1,2]

Affiliations

1 Universitätsaugenklinik, Universitätsmedizin Rostock, Deutschland
2 Department Leben, Licht & Materie, Universität Rostock, Deutschland
3 Klinik und Poliklinik für Augenheilkunde, Universitätsklinikum Hamburg-Eppendorf (UKE), Deutschland
4 Augenarztpraxis am UKE, Zentrumsehstärke, Hamburg, Deutschland
5 Institut für Automation und angewandte Informatik, Karlsruher Institut für Technologie (KIT), Eggenstein-Leopoldshafen, Deutschland
6 Institut für Anatomie, Universitätsmedizin Rostock, Deutschland

Correspondence

Prof. Rudolf F. Guthoff
Universitätsaugenklinik, Universitätsmedizin Rostock
Doberaner Straße 140, 18057 Rostock, Deutschland
Phone: + 49 (0) 38 14 94 85 88, Fax: + 49 (0) 38 14 94 85 49
rudolf.guthoff@med.uni-rostock.de

ABSTRACT

Introduction Confocal in vivo microscopy is an established method in ophthalmology research. As it requires contact coupling and calibration of the instruments is suboptimal, this method has been only rarely used in clinical routine work. As a result of close collaboration between physicists, information scientists and ophthalmologists, confocal laser scanning microscopy (CLSM) of the eye has been developed in recent years and a prototype can now be used in patients. The present study evaluates possible clinical uses of this method.

Material and Methods The essential innovations in CLSM are (1) a newly designed coupling element with superficial adaptation to corneal curvature and (2) the use of a dual computerised piezo drive for rapid and precise focusing. In postprocessing and after elastic imaging registration of the individual images parallel to the surface, it is also possible to produce sagittal sections resembling a split lamp and with resolution in the micrometer range. The concept was tested on enucleated pig bulbi and tested on normal volunteers and selected patients with diseases of the cornea.

Results Simultaneous imaging in planes parallel to the surface and in sagittal planes provided additional information that can help us to understand the processes of wound healing in all substructures of the cornea and the role of immune competent cells. Possible clinical uses were demonstrated in a volunteer with healthy eyes and several groups of patients (keratoconus after CXL, recurrent keratitis, status after PRK). These show that this new approach can be used in morphological studies at cellular level in any desired and appropriate test plane.

Conclusions It could be shown that this new concept of CLSM can be used clinically. It can provide valuable and novel information to both preclinical researchers and to ophthalmologists interested in corneal disease, e.g. density of Langerhans cells and epithelial stratification in ocular surface diseases.

---

*   These authors contributed equally to this work.

ZUSAMMENFASSUNG

Hintergrund Die konfokale In-vivo-Mikroskopie hat sich in der Augenheilkunde als Forschungsmethode etabliert. Wegen der Notwendigkeit einer Kontaktankopplung bei suboptimalen Justierungshilfen der Geräte wird die Methode bisher wenig im klinischen Routinebetrieb eingesetzt. Die konfokale Laserscanning-Mikroskopie (CLSM) des Auges konnte in den letzten Jahren durch die enge Zusammenarbeit von Physikern, Informatikern und Augenärzten weiterentwickelt werden und steht nun als ein am Patienten einsetzbarer Prototyp zur Verfügung. Im Rahmen dieser Studie wurden die Möglichkeiten der Methode im klinischen Einsatz evaluiert.

Material und Methoden Wesentliche Neuerungen der CLSM stellen (1) ein neugestaltetes Koppelelement mit einer der Hornhautkrümmung angepassten Oberfläche und (2) der Einsatz eines dualen computergestützen Piezoantriebs für eine schnelle präzise Fokusführung dar. Im Postprocessing und nach einer elastischen Bildregistrierung der oberflächenparallelen Einzelbilder gelingt es auch, sagittale, spaltlampenähnliche Schnitte mit einer Auflösung im Mikrometerbereich zu erzeugen. Die an enukleierten Schweinebulbi erprobte Konzeption wird bei Normalprobanden und ausgewählten Patienten mit Hornhauterkrankungen eingesetzt.

Ergebnisse Durch die simultane Darstellung von oberflächenparallelen und sagittalen Untersuchungsebenen können Zusatzinformationen zum Verständnis von Wundheilungsvorgängen aller Hornhautsubstrukturen und die Rolle von immunkompetenten Zellen zur Verfügung gestellt werden. Die klinischen Einsatzmöglichkeiten werden an einem Augengesunden und mehreren Beispielen (Keratokonus nach CXL, rezidivierende Keratitis, Zustand nach PRK) demonstriert. Diese zeigen, dass die morphologische Untersuchung der Hornhaut mit dem neuen Ansatz in jeder gewünschten und der Fragestellung angepassten Untersuchungsebene bei zellulärer Auflösung möglich ist.

Schlussfolgerungen Es konnte gezeigt werden, dass die neue Konzeption der CLSM klinisch einsetzbar ist und sowohl den tierexperimentell arbeitenden Forschenden als auch dem an Hornhauterkrankungen interessierten Augenarzt bisher nicht verfügbare Informationen, wie z. B. die Langerhans-Zelldichte und die Epithelschichtung bei Oberflächenerkrankungen des Auges, zur Verfügung stellen kann.

Introduction

The Zehender-Westien "binocular corneal loupe" can be regarded as the precursor of the slit lamp [1]. This enabled completely new insights into diseases of the cornea in living patients. The current possibilities are presented comprehensively in the article by Gellrich [2]. Allvar Gullstrand developed the slit lamp [3] into a universal ophthalmological tool and was awarded the Nobel Prize in medicine and physiology in 1911 for his fundamental work in the area of ophthalmological optics, hitherto the only ophthalmologist. Gullstrand's concept allows up to roughly 40-fold magnification but is unable to show individual cells. Alfred Vogt wrote the 3-volume "Lehrbuch und Atlas der Spaltlampenmikroskopie des lebenden Auges" [Textbook and atlas of slit lamp microscopy of the living eye] [4], which is still the standard work on slit lamp microscopy.

The principle of confocal microscopy was patented by Minsky in 1957 [5,6] but was forgotten until, after the patents expired, initial laboratory microscopes and a preliminary concept of confocal *in vivo* microscopy of the eye were presented in 1968 [6]. User-friendly devices were developed through optical improvements, miniaturisation and the development of rapid electronics. Slit scanning systems [7 – 10] initially enabled microscopy of the cornea. Laser scanning systems finally led to the concept of the confocal scanning laser ophthalmoscope, including in the form of the Heidelberg Retina Tomograph, which forms the basis for the Rostock Cornea Module and thus for confocal laser scanning microscopy (CLSM) of the cornea.

The slit lamp and CLSM differ in the direction of the examination plane as well as in the use of different optical principles. With the slit lamp the examiner obtains information along a sagittal orientation, whereas with CLSM the information is obtained from planes parallel to the surface. Moreover, for confocal microscopy direct contact of the system with the cornea via an immersion gel or differently shaped coupling element is necessary to achieve up to 800-fold magnification because of the different refractive indices of air and cornea and the resulting strong reflection at the superficial cells.

The clinical use of CLSM concentrates on the diagnosis of acanthamoeba keratitis, detection of keratomycosis and differential diagnosis and treatment planning of corneal dystrophies [11 – 13]. A new application has developed in the early identification of neurodegenerative diseases and their secondary complications by quantitative assessment of the sub-basal nerve plexus (SNP) [14].

Because coupling to the cornea is relatively unstable and focussing on the target site is laborious, it was difficult to obtain reproducible results in routine clinical practice so the diffusion of CLSM remained essentially limited to scientific research facilities. A DFG-sponsored collaboration between physicians, engineers, physicists and information scientists to address these deficiencies has eliminated many of these disadvantages and a prototype suitable for clinical use was developed [15]. In this study, the everyday usability of the system was demonstrated using a range of clinical examples.

Material and Methods

The new Rostock Corneal Module RCM 2.0 developed by us is based on the RCM, which is coupled with a HRT for corneal confocal microscopy. Since neither the internal focus drive of the HRT nor the additional focusing unit of the RCM provide suitable possibilities for rapid and controlled focus adjustment, a new mounting device for the objective was developed to obtain dedicated focusing (▶ **Fig. 1**), which completely replaces the previous RCM
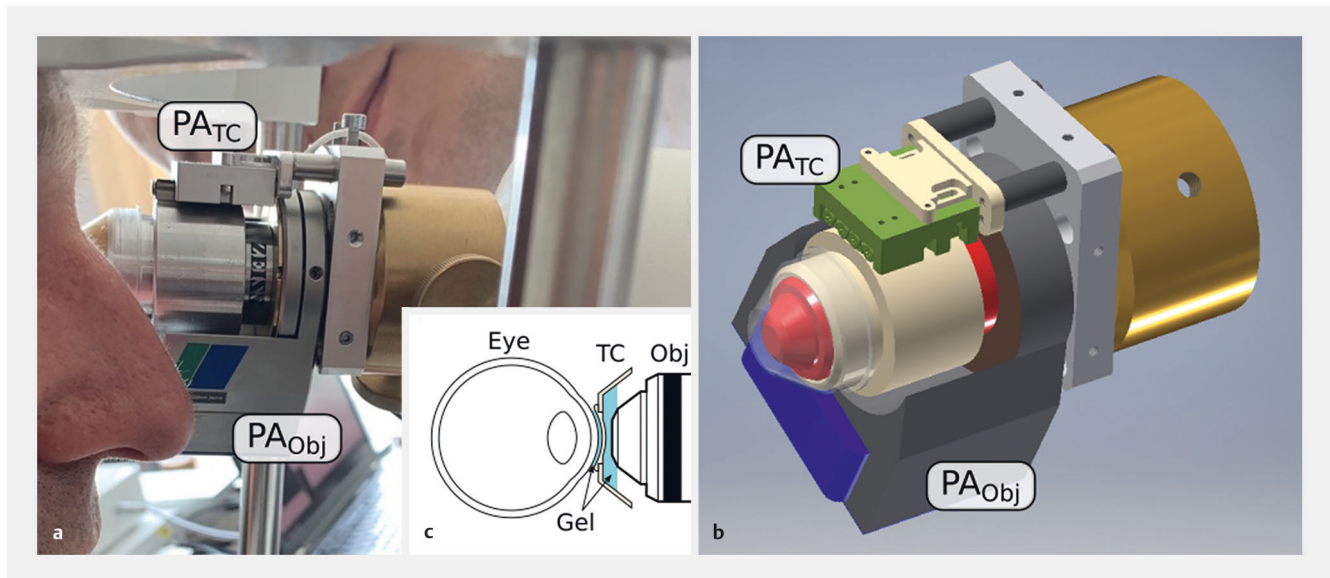
► **Fig. 1** *In vivo* examination with the RCM 2.0 (**a**), its CAD model (**b**) and a diagram of the coupling to the eye (**c**). The RCM 2.0 has two piezo actuators. The first one (PA$_{Obj}$) moves the objective and thus the focusing plane along the optical axis so it travels 500 µm in controlled operation. With the second piezo actuator (PA$_{TC}$) the contact cap can be moved over a total distance of 12 mm along the optical axis. Coupling of the concave contact cap to the eye and of the objective to the contact cap is achieved by a viscous tear substitute (gel), which is shown in blue (**c**).

[15]. With an integrated computer-controlled piezo actuator ($\Delta z_{max} = 500$ µm, $v_{max} = 800$ µm/s) the focusing plane can be adjusted precisely during imaging with the RCM 2.0. Unlike the conventional RCM, the position of the objective's contact cap remains unchanged in the RCM 2.0 when the focus is changed. The gel bridge between contact cap and cornea and consequently the force applied to the eye are thus no longer influenced by a change in focus setting.

A contact gel bridge between the cornea and the contact cap is necessary in confocal microscopic scanning of the cornea with both the RCM and with the RCM 2.0. Direct contact between the cap and the eye surface cannot be avoided and is usually even desirable when acquiring a scan series in order to stabilise the eye and in particular prevent eye movements in an axial direction (e.g., due to respiration and pulse). This always applies a certain force to the corneal tissue, which can lead to the development of tissue deformation. To avoid these fold-like bulges and further reduce eye movements a new contact cap design was developed. By using special contact caps with the radius of curvature of an average cornea, the originally flat contact surface was replaced by a concave curve [15]. In this way, deformation of the cornea in the frame area is reduced to a minimum, and lateral as well as axial eye movements are significantly reduced. This allows depth scans to be obtained over a large area, from which a nearly cuboid volume can be reconstructed with a high degree of reliability. From this, connected sectional images can be produced in any spatial direction. Volumetric scan analysis is possible only after complex elastic image registration [15].

In this study, we generated corneal stacks, as described in more detail in the publication by Bohn et al. (2018) [13].

The entire examination takes roughly 16 seconds to acquire about 500 single images at a feed of about 30 µm per second. The geometry of the coupling element, which is similar to that of a 3-mirror contact lens, stabilises the patient's eye through a roughly 50 µm film of a viscous tear substitute (Vidisic). As shown by Bohn et al. (2018), maximum displacements of 80 µm in the frontal imaging plane occur during the entire scan time under these conditions [13]. The possibilities are illustrated with the following examples:

1. an enucleated porcine eye, where the data set comprises three stacks of different thickness because of the partial overriding of surface structures,
2. a healthy human volunteer and
3. patients with corneal pathology.

To optimise the examination parameters, pig eyeballs were first examined 4 to 6 hours post mortem. In a clinical "proof of concept" study, selected patients from the corneal outpatient clinic were recruited after given written informed consent (positive vote of the ethics committee of University Medicine Rostock no.: A 2016–0197). This study presents and discusses one normal eye and three pathological conditions that can be delivered by the Rostock electronic slit lamp, which appear interesting in this connection.

None of the patients found the examination very uncomfortable. They were given viscous tear substitute for corneal care. Erosions or superficial punctate keratitis requiring treatment did not occur.

Results

Cornea of the porcine eyeball

Imaging of the pig eyeball delivered the best results after the pressure in it was increased by transscleral injection of a small quantity of buffered salt solution. For microscopy, the eyeballs were positioned on the vertically aligned microscope system without further fixing. An example of the imaging results is shown in ▸ **Fig. 2**.

The volume data set in this cases consists of c. 900 single scans in total, from which a sagittal optical section (▸ **Fig. 2a**) was calculated. Superficial cells (▸ **Fig. 2b**) and intermediate cells (▸ **Fig. 2c, d**) can be distinguished. Bowman's layer, which is c. 10 μm thick in humans, is not visualised.

The junction between epithelium and stroma is characterised by a layer of low reflectivity, which cannot be resolved further, and by isolated sub-basal nerves (▸ **Fig. 2e**). Keratocyte nuclei are visible in the stroma, and nerve structures anteriorly (▸ **Fig. 2f–j**). Unlike in humans, the cell nuclei can be identified in the regular endothelium, with c. 4000 cells per mm² (▸ **Fig. 2k**).

Normal human findings

The study subsequently included *in vivo* examinations of persons with healthy eyes (▸ **Fig. 3**). ▸ **Fig. 3a** shows the calculated sagittal section through the volume dataset of a volunteer and in this case the topmost 10 μm of the entire epithelium are highly outshone and do not allow any interpretation. Details of fine structures in the epithelium and anterior stroma are therefore shown in the next figure (▸ **Fig. 4**). Unremarkable wing cells (z = 23 μm) are found in ▸ **Fig. 3b**, a regular SNP (z = 45 μm) in ▸ **Fig. 3c** and the structureless Bowman layer (z = 57 μm) in ▸ **Fig. 3d**. The highly reflective keratocyte nuclei with a diameter of c. 20 μm are packed more densely in the anterior layers of the stroma than in the intermediate and deep stroma (▸ **Fig. 3e–h**). There the nuclear forms are usually elongated with a length/width ratio of c. 1:4 to 1:6 (▸ **Fig. 3b–e**). The nuclei can be seen up to about 10 μm before Descemet's membrane, which itself has no sources of scattered light (▸ **Fig. 3i**). The endothelial cells appear similarly to in specular microscopy and in this example they have a cell density of c. 2200 cells per mm² (▸ **Fig. 3j**). In the present example, the central corneal thickness is 466 μm, corresponding to the position of the superficial cells as far as the endothelial cells.

The details of the cornea as far as a depth of c. 150 μm are shown in ▸ **Fig. 4**. The epithelial layers are readily distinguishable and are bordered by the superficial cells and the surface of the Bowman layer.

▸ **Fig. 4b** shows the roof tile-like overlapping of the superficial cells with a maximum diameter of c. 50 μm and sometimes clearly demarcated cell nuclei. The most superficial of the cells about to desquamate exhibit signal-intensive cytoplasm. The mean cell density is c. 1000 cells per mm². In the wing cell layer shown in ▸ **Fig. 4c** the cell boundaries can be identified particularly well as highly reflective structures, the cytoplasm has a uniform medium to low intensity and cell nuclei are not identifiable. The cell density is c. 3000 cells per mm². The basal cell layer (▸ **Fig. 4d**) is characterised by cells of varying reflectivity with well demarcated cell boundaries and a suggestion of visible cell nuclei. The cell density is c. 8000 cells per mm².

▸ **Fig. 4e** shows an unremarkable SNP with isolated dendritic cells, ▸ **Fig. 4f** shows the largely low-contrast Bowman layer, which has a thickness of c. 10 μm, as can be seen in ▸ **Fig. 4a**. The distance from the superficial cells to the SNP is c. 50 μm and can be used as a measurement of epithelial thickness.

▸ **Figs. 4g–i** show sections through the anterior stromal regions characterised in ▸ **Fig. 4a**. In a few stromal layers in this example, especially at a depth of 131 μm (▸ **Fig. 4i**), indicative cytoplasmic elements of the complex keratocyte meshwork can be identified as fine granular structures under 2 μm.

Corneal pathology

Building on the information obtained from the healthy human cornea, pathological changes are analysed below. ▸ **Fig. 5** shows the findings in a 35-year-old patient 8 months after CXL (Dresden protocol). The slit lamp appearance showed a typical minimal haze in the anterior corneal stroma. Corrected vision was 0.6 and regression can be identified in the differential representation of the corneal tomography with a reduction in the maximum K values. Pachymetry shows that the corneal thickness is reduced by 17 μm 8 months after cross-linking.

Corresponding to the slight haze found clinically and on slit lamp microscopy, fine details at cellular level are identified in the further confocal microscopy analysis. Confocal microscopy shows normal epithelial layers (▸ **Fig. 5b, c**), the SNP (▸ **Fig. 5d**, z = 42 μm deep) is highly rarefied and partly connected with polymorphic and highly reflective structure. At the level directly next to the Bowman layer (▸ **Fig. 5e**, z = 54 μm deep) a network of highly reflective irregular stellate structures is apparent (maximum diameter c. 20 μm). In the anterior stroma (▸ **Fig. 5f**; z = 140 μm), structures are found, some delicate, apparently connected with each other, which correspond to keratocytes in shape and size. 90 μm deeper (▸ **Fig. 5g**, z = 227 μm) there are low-contrast keratocytes without a distinguishable nucleus. These images, which differ from the appearance of a healthy cornea, often contain cells that recall immunocompetent phagocytic cells in their size and morphology, which are probably macrophages. Hypothetically, these remodelling processes still present even after 8 months could be responsible on cellular level for the more prolonged stabilisation/regression of the keratoconus observed after CXL. One of these individual highly reflective cells is shown in the nearly acellular appearing stromal region (▸ **Fig. 6**, z = 205 μm). A further 70 μm deeper (▸ **Fig. 5h**, z = 275 μm), highly reflective cell nuclei and spindle- to needle-shaped structures over 100 μm in length can be seen. At a depth of 371 μm (▸ **Fig. 5i**) poorly reflecting posterior keratocytes without visible nuclear structures can be identified. The endothelium (▸ **Fig. 5j**, z = 407 μm) shows a normal structure with c. 2100 cells per mm².

Compared with the previously described cornea, which appears almost normal under the slit lamp, diffuse clouding can be identified in the anterior stroma in a patient with recurrent keratitis. The example shows the eye of a 49-year-old patient with recurrent keratitis for 2 years, at times with intraocular inflammation, suspected herpes simplex infection, corrected vision 0.1. A zone in the anterior corneal stroma with particles of greater re-
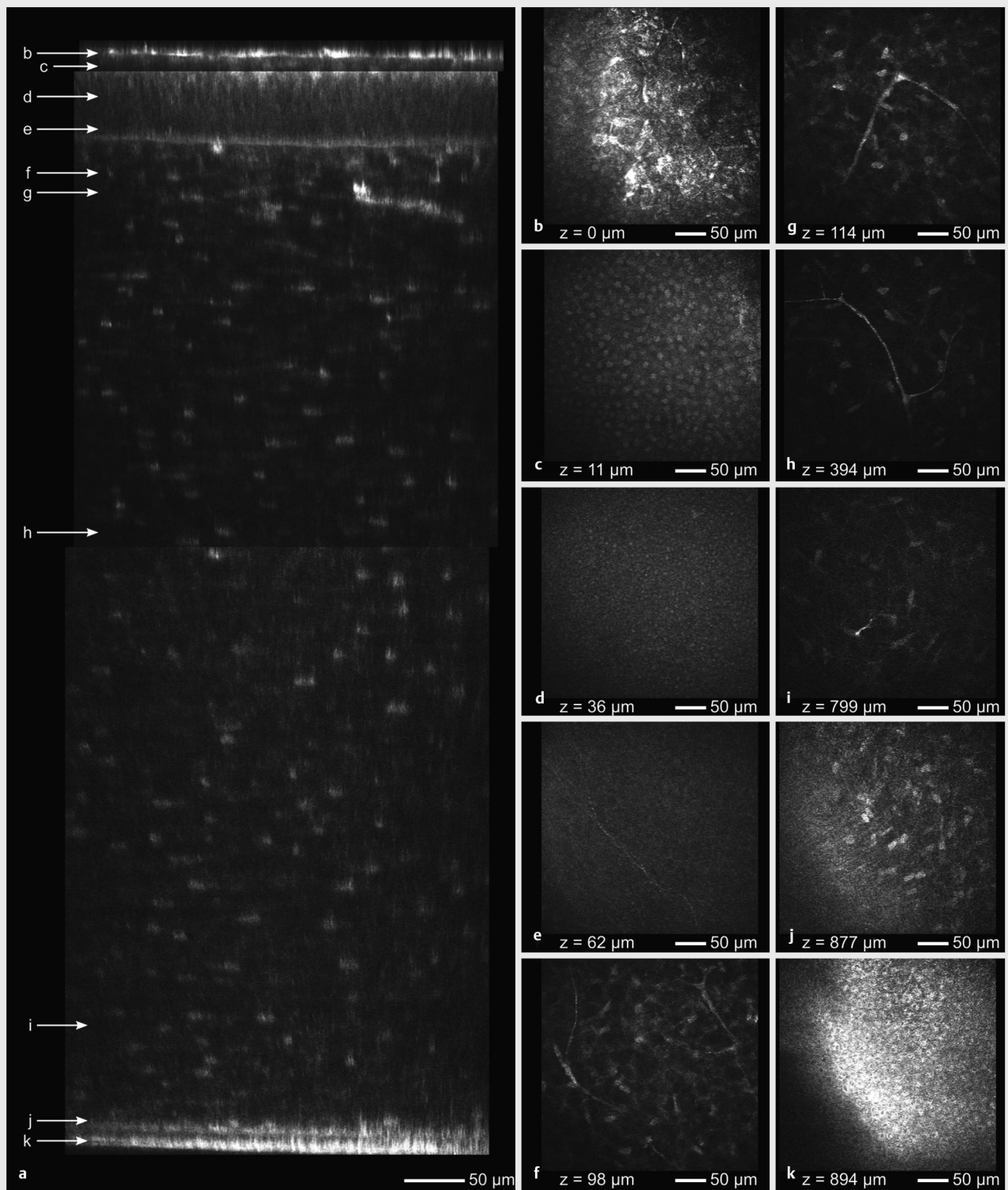
▶ Fig. 2 CLSM of a pig cornea *ex vivo* 5 hours post mortem. The slit lamp sagittal section (**a**) contains c. 900 optical sections scanned parallel to the surface within the underlying dataset, which are shown in the individual figures **b–k** as an example.
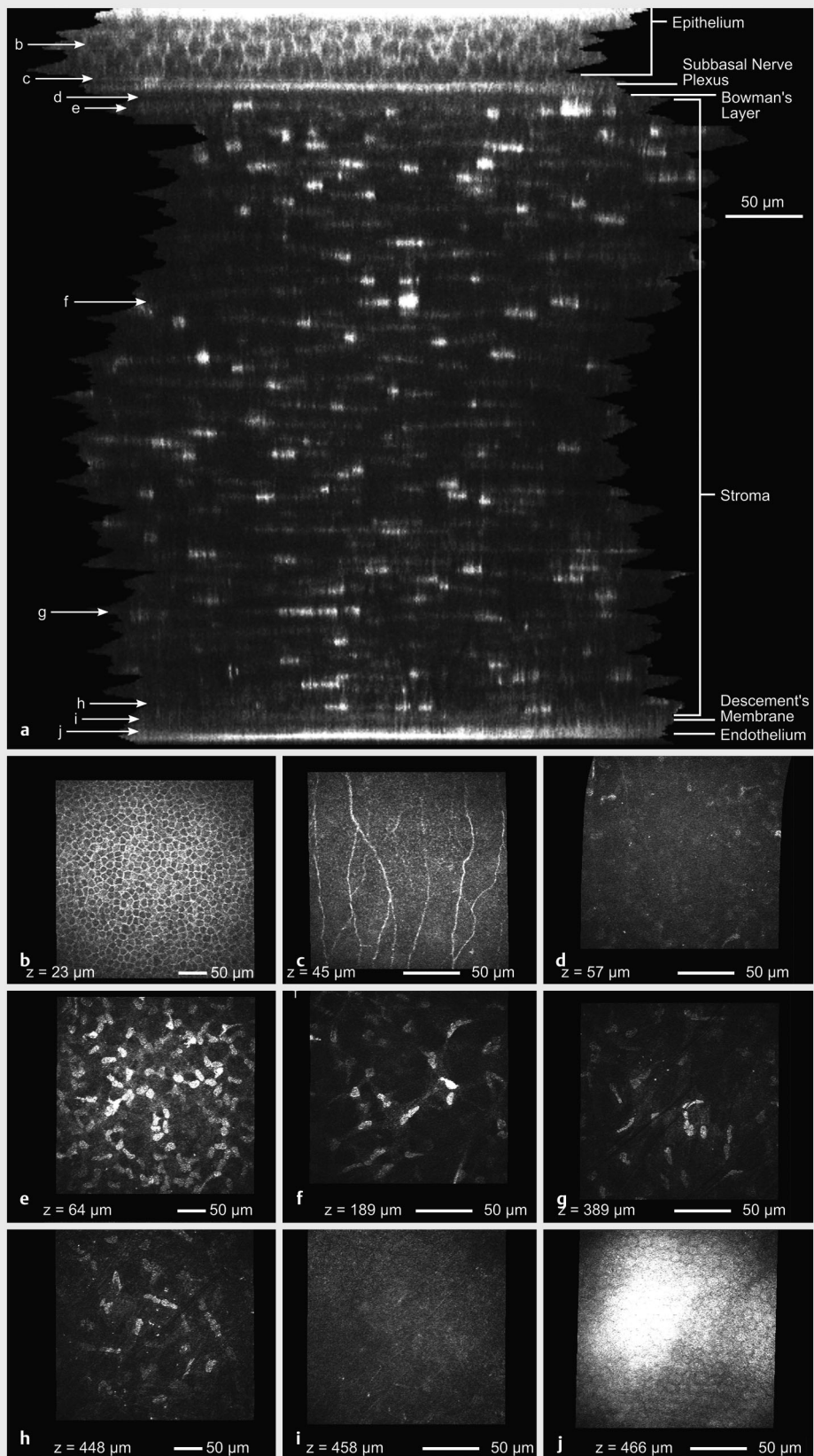
Fig. 3 CLSM-based imaging of a 54-year-old volunteer with healthy eyes. The top epithelial layers are overmodulated. Figures **b–j** show sections parallel to the surface at the depths given in **a**.
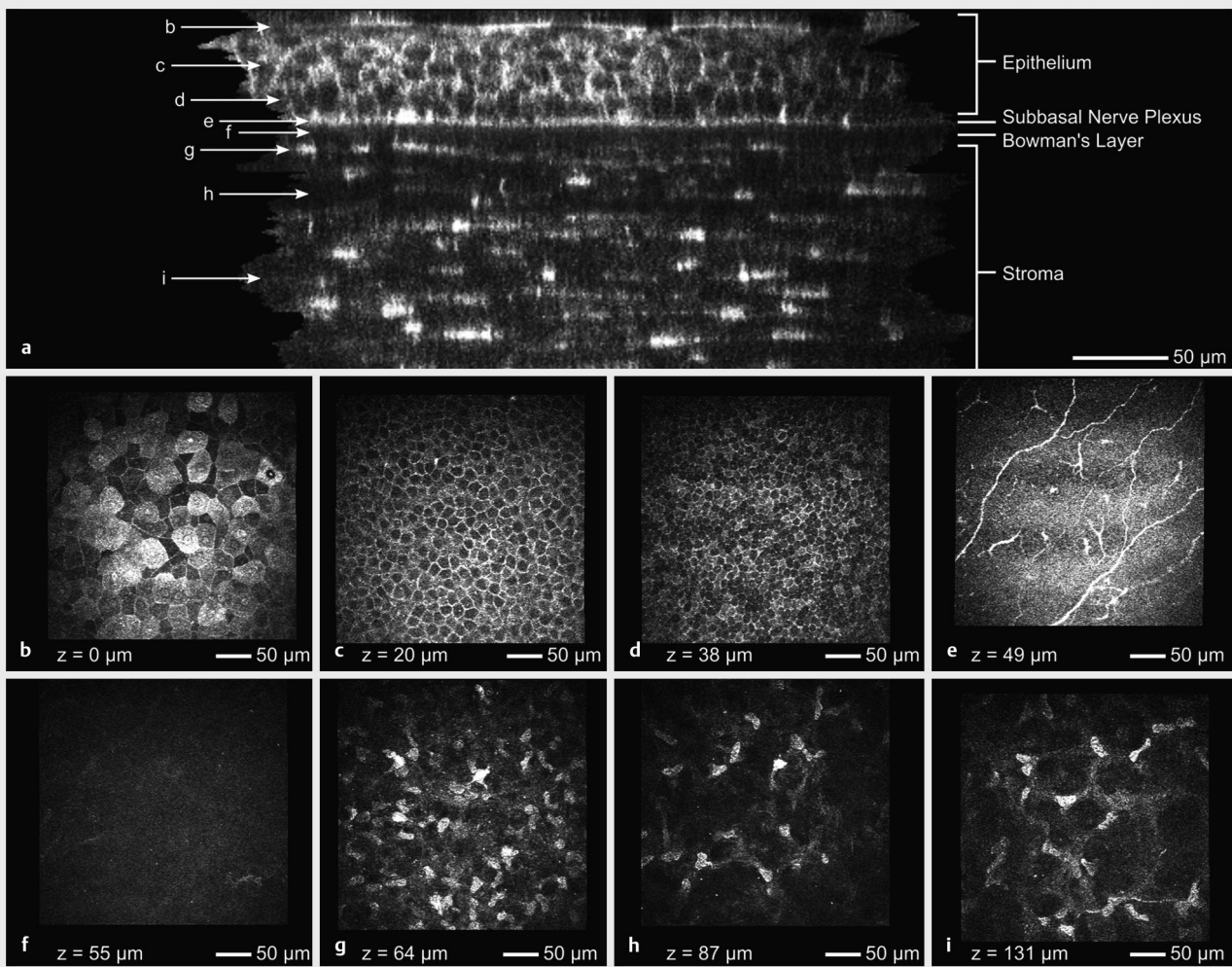
► **Fig. 4** CLSM-based detailed view of the epithelium and anterior stroma of a volunteer with healthy eyes. **a** Calculated sagittal section. **b–i** Images from the stack parallel to the surface as the depths given in **a**.

flectivity but not further resolvable can be seen on slit lamp microscopy (► **Fig. 7 a**) and OCT (► **Fig. 7 b**).

Confocal microscopy in axial section (► **Fig. 8**) shows normally layered epithelium, well demarcated Bowman layer and highly reflective structures located deeper in the anterior and intermediate stroma (► **Fig. 8 a**).

Sections parallel to the surface show normal wing cells at a depth of 30 µm (► **Fig. 8 b**), and massive infiltrates are found between 40 µm and 50 µm (► **Fig. 8 c**) with dendritic cells, which can also be identified on the Bowman layer with markedly reduced SNP at a depth of 52 µm (► **Fig. 8 d**). In the anterior and intermediate stroma there is a dense network of keratocyte structures, some with extremely highly reflective cytoplasm, and cell nuclei can no longer be demarcated in the deeper stroma (► **Fig. 8 e–h**). The endothelial cell density is reduced to c. 1000 cells per mm². Isolated precipitates are found with a maximum extent of 50 µm (► **Fig. 8 i**). ► **Fig. 8 j** is a 3D reconstruction from the Bowman layer as far as the highly reflective anterior stroma (► **Fig. 8 e**).

► **Fig. 9** shows the appearance in a 26-year-old patient a month after PRK with unremarkable healing and uncorrected vision of 0.8.

Confocal microscopy (sagittal section) shows normal epithelial layers in ► **Fig. 9 a**. As expected, no signal-free zone corresponding to the Bowman layer is found beneath it. The anterior stroma appears unremarkable.

The sections parallel to the surface in ► **Fig. 9 b** show a normal superficial layer, the cell boundaries are less clear in the deep epithelial layers and cell nuclei are visible (► **Fig. 9 c**). No sub-basal nerve structures can be seen (► **Fig. 9 d, e**). Round, highly reflective structures with a diameter of c. 5 µm can be identified at the junction with the stroma (► **Fig. 9 d–f**), the top parts of the stroma are characterised by highly branched and highly reflective keratocytes (► **Fig. 9 g**), the highly reflective elements decrease 10 µm deeper (► **Fig. 9 h**) and very fine needle-shaped structures are detectable. In deeper layers (► **Fig. 9 i, j**) normal keratocyte nuclei predominate with shadowy cytoplasmic offshoots, and even deeper stromal layers appear normal.
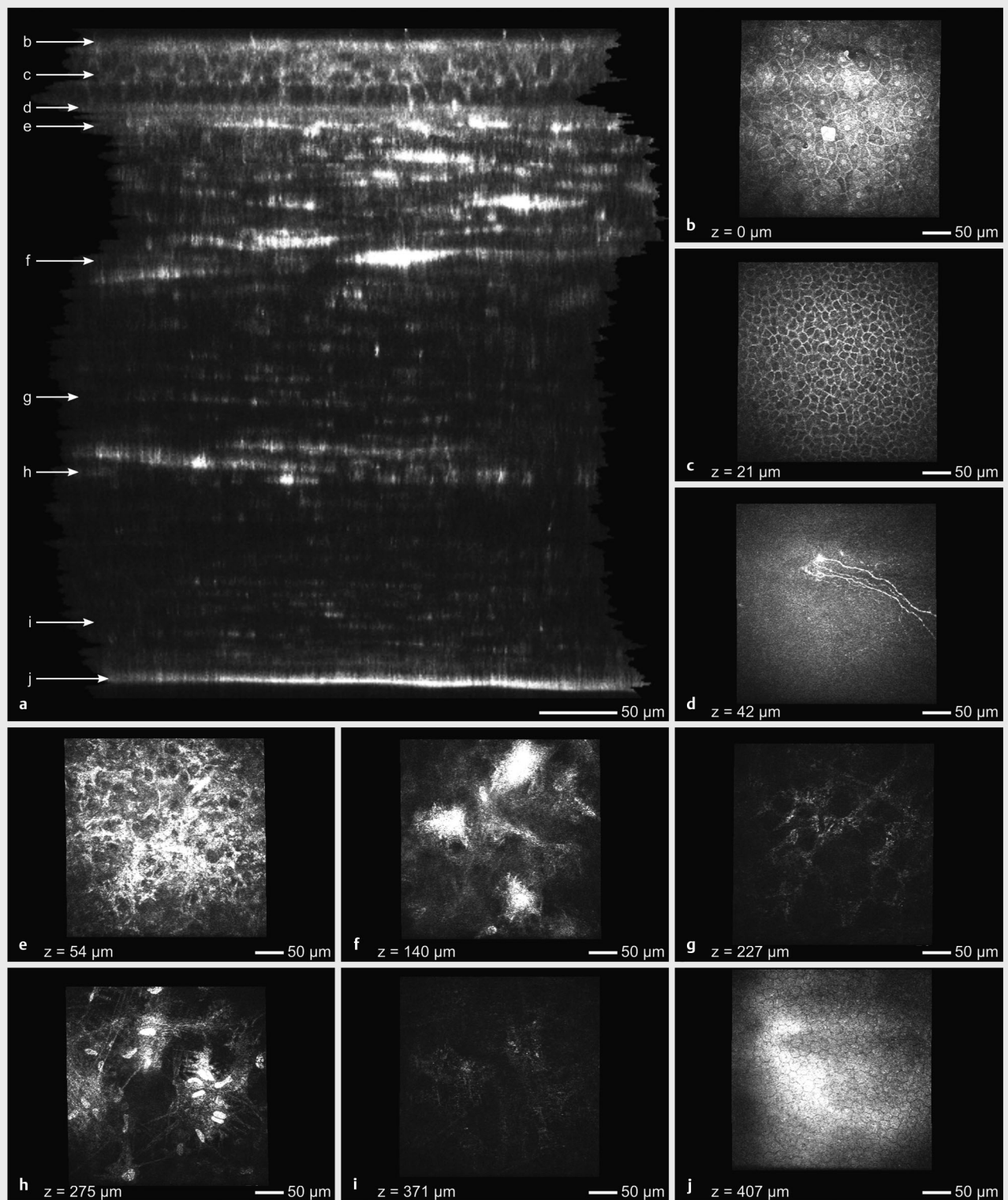
▶ **Fig. 5** CLSM-based imaging of a 35-year-old patient 8 months after CXL (Dresden protocol). Corrected vision 0.6. The computed section (**a**) shows normal epithelial layers (**b, c**), highly rarefied SNP (**d**), and zones of clouding in the anterior stroma, which can be assigned to the hyper-reflecting cytoplasm of keratocytes in sections parallel to the surface (**e, f**). In the intermediate and deep stroma, mesh-like keratocyte structures (**g**) are found, with keratocyte nuclei surrounded by needle-like elements in deeper regions (**h, i**). The endothelium appears normal (**j**).
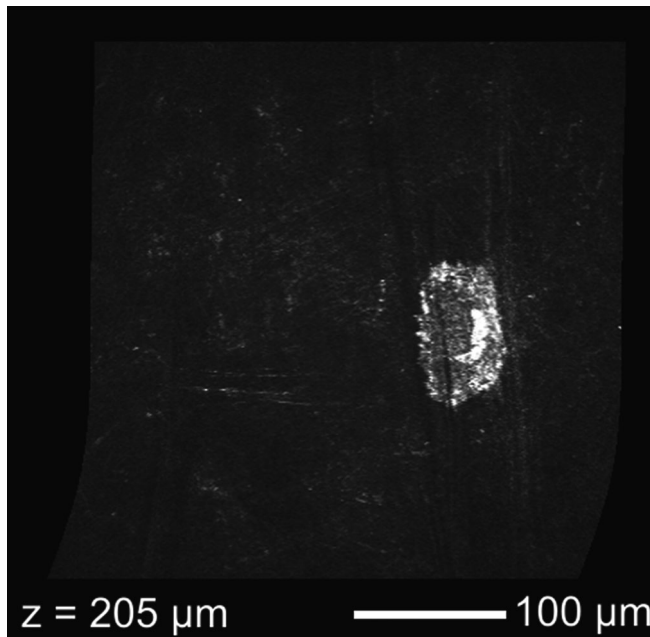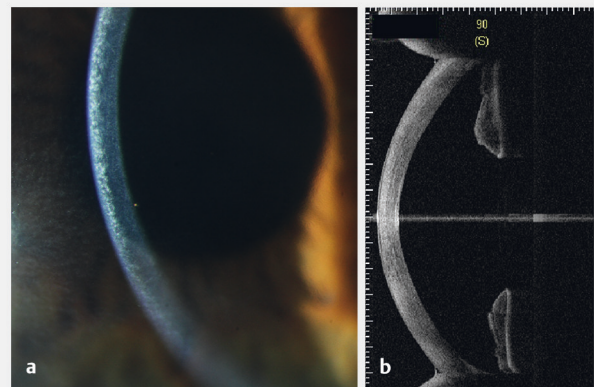
▶ **Fig. 6** CLSM-based appearance of an immunocompetent cell in the stroma of the CXL patient from ▶ **Fig. 5**. In a nearly acellular appearing zone, isolated highly reflective and very large cells could be identified. The morphology of this cell type suggests that they are monocytes or macrophages.


▶ **Fig. 7** A zone in the anterior corneal stroma with particles of greater reflectivity but not further resolvable can be seen on slit lamp microscopy (**a**) and anterior segment OCT (3D CAS-OCT, SS-1000; Tomey GmbH, Nuremberg, Germany) (**b**).

Discussion

The initial results of examination with the Rostock electronic slit lamp show findings that can only be suspected with a conventional slit lamp. Slit lamp photography and anterior segment OCT delivered clearly pathological findings only in keratitis (▶ **Fig. 7**). The changes after CXL and PRK were too slight to allow photographic documentation.

Detection and classification of all the information from a volume region of the cornea available through CLSM enable the clinician to select corneal section planes adjusted to his query and at approximately 800-fold magnification. Similar findings were published in 1990 by Cavanagh et al. from Houston [9]. The same research group impressively demonstrated the additional information that can be obtained by sequential recording of 2D confocal datasets in animal studies of radial keratotomy [16 – 18]. However, these developments were not suitable for routine clinical use.

The system presented in this study now permits this additional information to be used in clinical practice also by precise volume scans with the aid of piezo actuators in association with a reduction in movement artefacts through the use of a contact cap adapted to the curvature of the corneal surface. Measurement of the thickness of epithelial and stromal layers enables the cornea to be assessed in detail, which could play a part in diagnosis and treatment monitoring of patients with ocular surface disease [19]. It can be assumed that the physiological layering and dimensions of the individual epithelial cells are altered at the respective anatomical depth depending on the cause of the ocular surface disease. The other examples presented in this study show that information otherwise obtained only by histological examination can now to a large extent be obtained also by the use of CLSM on patients *in vivo*. In order to better understand the "*in vivo* histology" that is now possible, it will have to be accompanied by experimental studies.

Ex vivo examination of cornea excised from patients having perforating or lamellar keratoplasty would be a potential approach. Directly following these examinations of "living" tissue, the specimens could be passed on to classic histology where all the possibilities of modern staining techniques as well as immunohistochemical techniques are available.

▶ **Fig. 8** CLSM-based imaging of a 49-year-old patient after recurrent keratitis and moderate clouding in the anterior stroma on slit lamp microscopy. The computed section (**a**) shows normal epithelial structure, readily visible Bowman layer and marked elements of clouding in the anterior stroma. Sections of epithelium parallel to the surface show normal wing cells (**b**). In addition, dense infiltration of Langerhans cells can be identified in sections of the deep epithelium parallel to the surface (**c**), which can also be shown at the level of the sub-basal nerve plexus (**d**). The clouding elements in the stroma can be assigned with a large degree of probability to the cytoplasmic structures of the keratocyte (**e**). In deeper sections of the stroma parallel to the surface, keratocyte structures can be seen in which the cell nuclei can no longer be demarcated (**f–h**). In the depth of the endothelium isolated precipitates are visible (**i**). 3D reconstruction of a tissue block c. 300 μm wide (**j**). The structureless surface corresponds to a section through the Bowman layer. The top view of the lower block in this pathology shows highly reflecting keratocytes with cytoplasmic offshoots, which appear to be in contact with their neighbouring cells (syncytium).
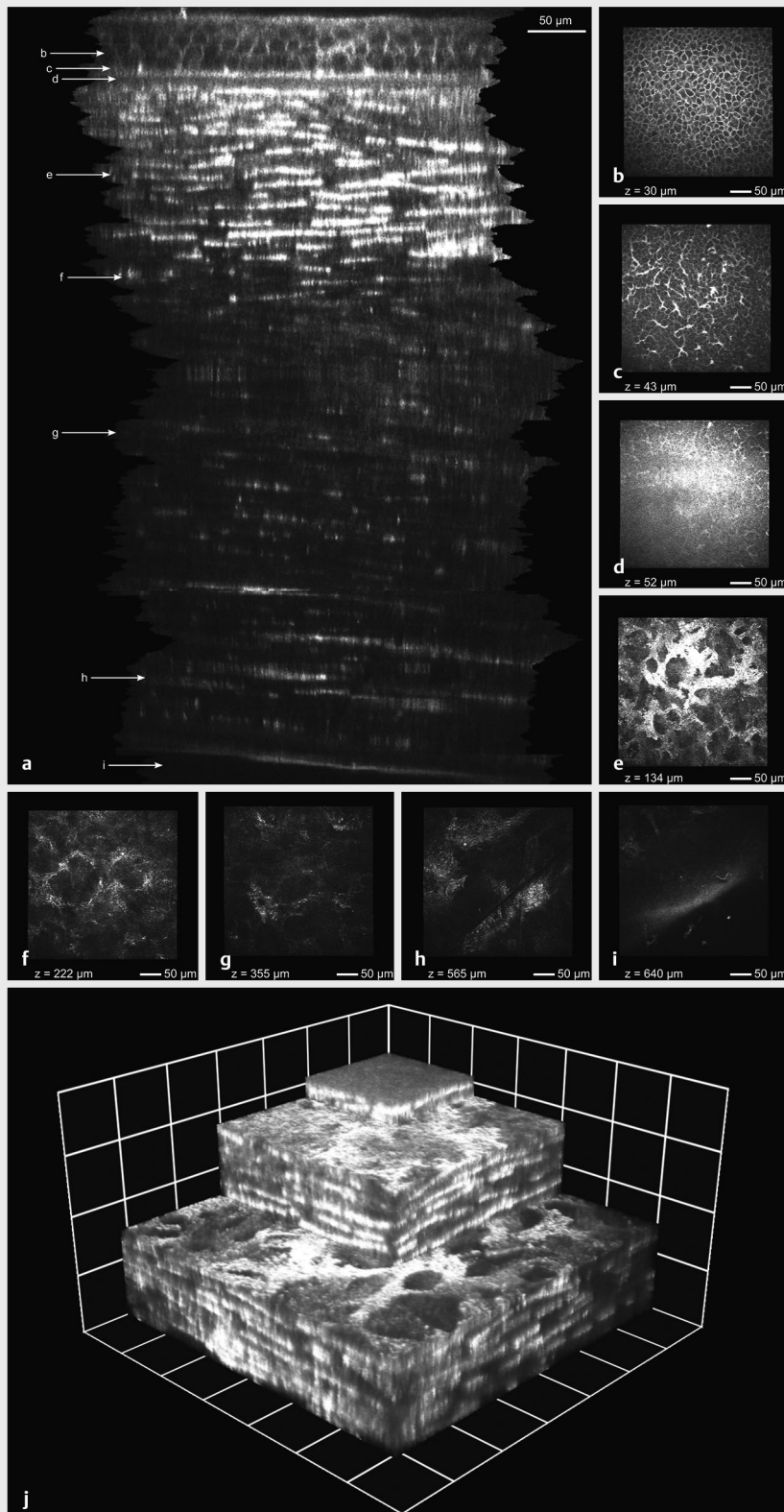
▶ Abb. 8
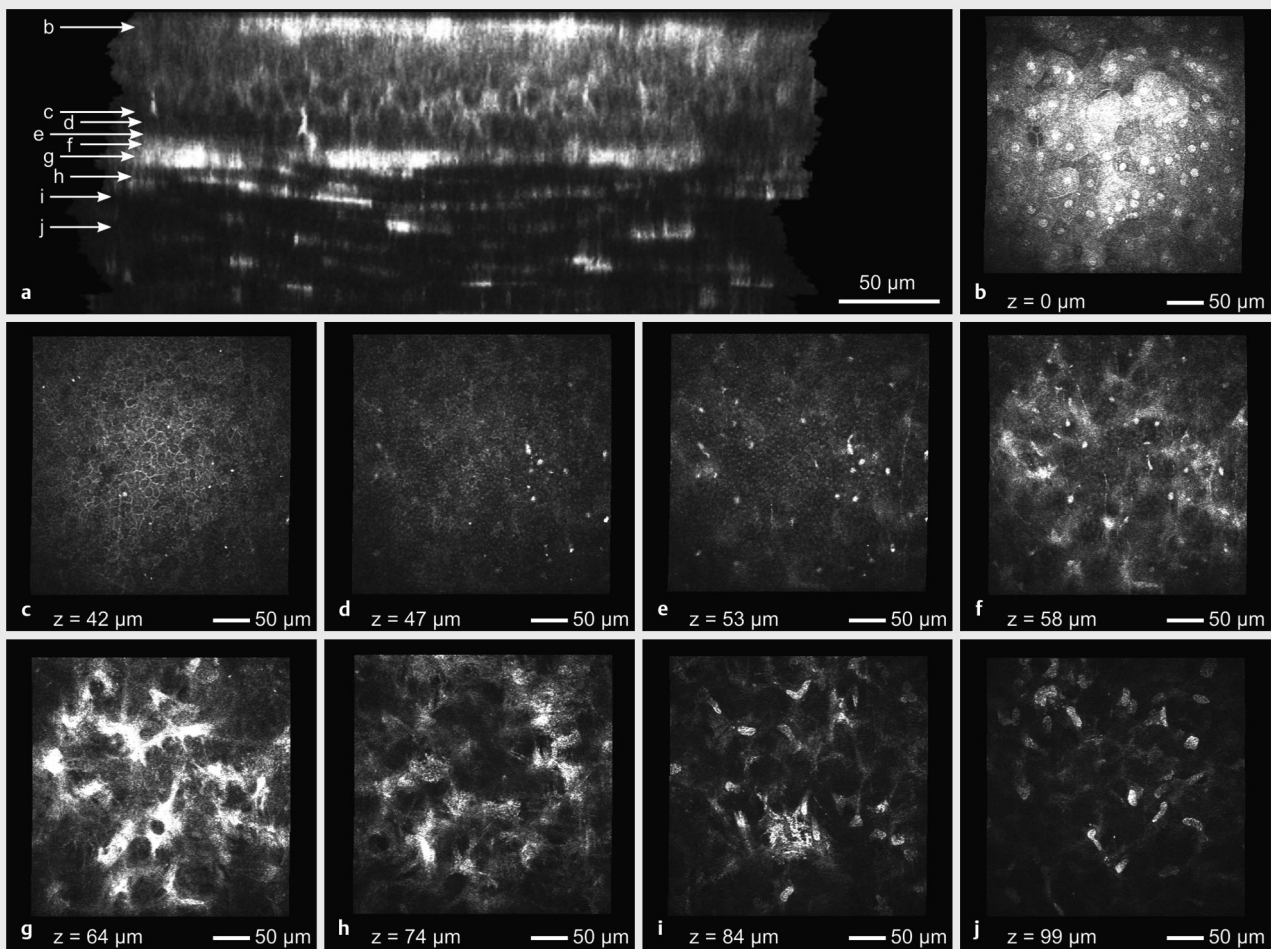
▶ **Fig. 9** CLSM-based imaging of a 26-year-old patient after PRK. The computed section (**a**) shows unremarkable epithelium, no equivalent of the Bowman layer, as well as highly reflective structures in the anterior stroma. **b** Intact superficial cells. **c–f** Basal cells at the junction with the anterior stroma. **g, h** Keratocytes, some with visible cytoplasmic offshoots, some with regular nuclear structure (**i, j**).

Electron microscopy analysis is useful to obtain an understanding of the causes of the highly scattering elements when there are pathological or postoperative findings in the nanometre range. In transmission electron microscopic images of keratocytes from a healthy cornea and from a cornea after CXL the treatment-induced cellular changes and also the modulation of the organisation of the collagen fibre network of the cornea are visible (▶ **Fig. 10**). These supplementary methods should allow Langerhans cells to be assessed at their different maturation stages and also other immunocompetent cells to be specified, thus indirectly including immunological conditions in treatment monitoring via confocal *in vivo* microscopy. Moreover, new knowledge can be gained regarding rejection reactions after transplant surgery or after CXL in keratoconus patients. The studies by Hamrah and Chinnery have already demonstrated different local and immunocompetent cell population (dendritic cells at various maturation stages as well as monocytes and macrophages) in mouse corneal stroma [20–22], which can now be extended to include human findings *in vivo*. As demonstrated in ▶ **Fig. 8 i**, it is also possible to

assess the endothelium when corneal transparency is impaired (in this patient, vision was 0.1 due to the cornea), which would hardly be possible by specular microscopy. In addition, it was only partially possible hitherto
1. to document the exact location of keratocytes and
2. to link keratocyte damage with noxious agents.

The system presented here now makes it possible to record the complex 3D morphology of keratocytes as a syncytium *in vivo* and characterise them according to their number, morphology and functional state [23]. This new information may be of interest for a better understanding of the migration behaviour of keratocytes in the repopulation of the keratocyte-free anterior stroma following CXL and in the possibility of pharmacological cell protection. In this connection, heparan sulphate (Cacicol) has already been shown in animal studies to have a keratocyte-protective effect with defined noxious agents [24].

As the results of confocal microscopy in chronic intrastromal inflammatory processes show (▶ **Fig. 8**), zones of clouding also
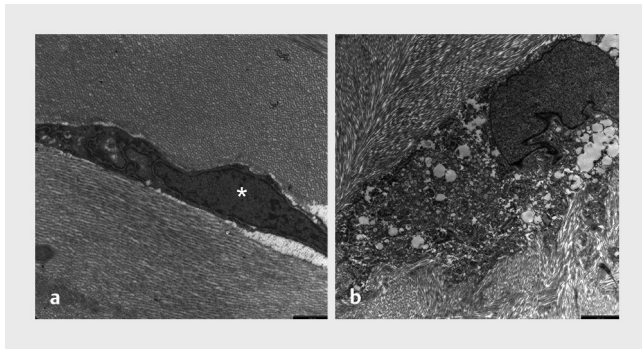
► **Fig. 10** Transmission electron microscopic appearance of keratocytes of the anterior stroma of rabbits. **a** Intact keratocyte of a healthy and untreated rabbit. The cell nucleus can be readily identified within the cytoplasm of the flattened cell (*). Transversely cut collagen fibrils can be seen above and longitudinally cut fibrils beneath the keratocyte. **b** Damaged oedematous keratocyte of a rabbit after experimental cross-linking. The collagen fibril network appears much less ordered. Measuring bar: 2.5 µm.

arise because of intracellular sources of scattered light, but there has been no information in the literature to date regarding the histological correlation. Obviously, they arise independent of clouding that can be explained by destruction of the complex extracellular 3D collagen fibre network.

Apart from the described potential uses of the new system in assessing pathological changes of the cornea, fundamental and controversial anatomical questions can also be re-evaluated. It is known from *ex vivo* confocal microscopy findings, for example, that the morphology and cell density of the keratocytes within the corneal stroma vary by a factor of more than two between anterior and posterior [25, 26]. Because this information was hitherto difficult to quantify *in vivo* these associations depending on different disease conditions have not been investigated so far. Moreover, the method can also be used for more detailed characterisation of the still controversial corneal layer directly in front of Descemet's membrane [27], as described by Dua.

Conclusions

CLSM is a non-invasive imaging technique that can generate *enface* images of the cornea with high resolution and high depth discrimination. The sequential acquisition of tomographs along the depth direction enables 3D reconstruction of the volumetric data stack. The imaging method covers a wide range of experimental and clinical uses. In our view, therefore, the Rostock electronic slit lamp can be useful for basic research into corneal micromorphology and can also assist routine clinical decision-making. The range extends from anatomical studies to a discriminating consideration of corneal pathologies *in vivo*. Intensive research currently is concentrated on extensive image reconstruction of the SNP as this has the potential to act as a biomarker for early neurodegenerative changes. In this connection, Langerhans cells at different maturation stages and of other immunocompetent cells are assessed successfully.

This technology thus enables corneal imaging to be generated and assessed at cellular level with subsequent 2D mosaic or 3D reconstruction. This development was possible through trust-based interdisciplinary collaboration for many years. It is hoped that the new diagnostic possibilities can be made available to a wide circle of user through series production.

Dedication

Dedicated to Joachim Stave on his 80th birthday.

Conflict of Interest

The authors declare that they have no conflict of interest.

References

[1] Schmidt D. Carl Wilhelm von Zehender: Vater der Mikrochirurgie, erster Herausgeber der klinischen Monatsblätter für Augenheilkunde und Mitbegründer der Ophthalmologischen Gesellschaft Heidelberg. In: Krogmann F, Hrsg. Mitteilungen der Julius-Hirschberg-Gesellschaft zur Geschichte der Augenheilkunde. Würzburg: Königshausen & Neumann; 2001: 79–166

[2] Gellrich MM, Schmidt D, Hrsg. Die Spaltlampe. Heidelberg: Kaden; 2011

[3] Gullstrand A. Die Nernstspaltlampe in der ophthalmologischen Praxis. In: Gellrich MM, Schmidt D, Hrsg. Die Spaltlampe. Heidelberg: Kaden; 2011: 165–179

[4] Vogt A. Lehrbuch und Atlas der Spaltlampenmikroskopie des lebenden Auges mit Anleitung und Methodik der Untersuchung. In: Gellrich MM, Schmidt D, Hrsg. Die Spaltlampe. Heidelberg: Kaden; 2011: 165–179

[5] Minsky M. Microscopy Apparatus. US Patent 3,013,467; 1961

[6] Minsky M. Memoir on inventing the confocal scanning microscope. Scanning 1988; 10: 128–138. doi:10.1002/sca.4950100403

[7] Maurice DM. A scanning slit optical microscope. Invest Ophthalmol 1974; 13: 1033–1037

[8] Koester CJ. Scanning mirror microscope with optical sectioning characteristics: applications in ophthalmology. Appl Opt 1980; 19: 1749–1757. doi:10.1364/AO.19.001749

[9] Cavanagh HD, Jester JV, Essepian J et al. Confocal microscopy of the living eye. CLAO J 1990; 16: 65–73

[10] Masters BR, Thaer AA. Real-time scanning slit confocal microscopy of the in vivo human cornea. Appl Opt 1994; 33: 695–701. doi:10.1364/AO.33.000695

[11] Guthoff RF, Zhivov A, Stachs O. In vivo confocal microscopy, an inner vision of the cornea – a major review. Clin Exp Ophthalmol 2009; 37: 100–117. doi:10.1111/j.1442-9071.2009.02016.x

[12] Daas L, Viestenz A, Bischoff M et al. Confocal microscopy for the diagnostics of fungal keratitis. Ophthalmologe 2016; 113: 767–771. doi:10.1007/s00347-015-0206-4

[13] Daas L, Bischoff-Jung M, Viestenz A et al. Confocal microscopy as an early relapse marker after keratoplasty due to Fusarium solani keratitis. Ophthalmologe 2017; 114: 66–69. doi:10.1007/s00347-016-0270-4

[14] De Clerck EEB, Schouten JS, Berendschot TTJM et al. New ophthalmologic imaging techniques for detection and monitoring of neurodegenerative changes in diabetes: a systematic review. Lancet Diabetes Endocrinol 2015; 3: 653–663. doi:10.1016/S2213-8587(15)00136-9

[15] Bohn S, Sperlich K, Allgeier S et al. Cellular in vivo 3D imaging of the cornea by confocal laser scanning microscopy. Biomed Opt Express 2018; 9: 2511–2525. doi:10.1364/BOE.9.002511

[16] Beuerman RW, Laird JA, Kaufman SC et al. Quantification of real-time confocal images of the human cornea. J Neurosci Methods 1994; 54: 197–203. doi:10.1016/0165-0270(94)90193-7

[17] Cavanagh HD, Petroll WM, Jester JV. Confocal Microscopy. In: Krachmer JH, Mannis MJ, Holland EJ, eds. Cornea. Philadelphia: Elsevier Mosby; 2005: 283–297

[18] Petroll WM, Robertson DM. In Vivo Confocal Microscopy of the Cornea: New Developments in Image Acquisition, Reconstruction, and Analysis Using the HRT-Rostock Corneal Module. Ocul Surf 2015; 13: 187–203. doi:10.1016/j.jtos.2015.05.002

[19] Eckard A, Stave J, Guthoff RF. In vivo investigations of the corneal epithelium with the confocal Rostock Laser Scanning Microscope (RLSM). Cornea 2006; 25: 127–131. doi:10.1097/01.ico.0000170694.90455.f7

[20] Hamrah P, Liu Y, Zhang Q et al. The corneal stroma is endowed with a significant number of resident dendritic cells. Invest Ophthalmol Vis Sci 2003; 44: 581–589. doi:10.1167/iovs.02-0838

[21] Chinnery HR, Leong CM, Chen W et al. TLR9 and TLR7/8 activation induces formation of keratic precipitates and giant macrophages in the mouse cornea. J Leukoc Biol 2015; 97: 103–110. doi:10.1189/jlb.3AB0414-216R

[22] Chinnery HR, McMenamin PG, Dando SJ. Macrophage physiology in the eye. Pflugers Arch 2017; 469: 501–515. doi:10.1007/s00424-017-1947-5

[23] Hovakimyan M, Falke K, Stahnke T et al. Morphological analysis of quiescent and activated keratocytes: a review of ex vivo and in vivo findings. Curr Eye Res 2014; 39: 1129–1144. doi:10.3109/02713683.2014.902073

[24] Hovakimyan M, Stachs O, Céline O et al. Matrix-Based Regenerating Agent for Corneal Wound Healing After Collagen Cross-Linking. Cornea 2016; 35: 1638–1643. doi:10.1097/ICO.0000000000001047

[25] Hahnel C, Somodi S, Weiss DG et al. The keratocyte network of human cornea: a three-dimensional study using confocal laser scanning fluorescence microscopy. Cornea 2000; 19: 185–193. doi:10.1097/00003226-200003000-00012

[26] Stave J, Zinser G, Grümmer G et al. [Modified Heidelberg Retinal Tomograph HRT. Initial results of in vivo presentation of corneal structures]. Ophthalmologe 2002; 99: 276–280. doi:10.1007/s003470100535

[27] Dua HS, Faraj LA, Said DG et al. Human corneal anatomy redefined: a novel pre-Descemet's layer (Dua's layer). Ophthalmology 2013; 120: 1778–1785. doi:10.1016/j.ophtha.2013.01.018

Morphological characterization of the human corneal epithelium by *in vivo* confocal laser scanning microscopy

Katharina A. Sterenczak, Karsten Winter, Karsten Sperlich, Thomas Stahnke, Stephan J. Linke, Sanaz Farrokhi, Maren Klemm, Stephan Allgeier, Bernd Köhler, Klaus-Martin Reichert, Rudolf F. Guthoff, **Sebastian Bohn**, and Oliver Stachs

Copyright notice

Original Article

Morphological characterization of the human corneal epithelium by *in vivo* confocal laser scanning microscopy

Katharina A. Sterenczak[1#^], Karsten Winter[2#], Karsten Sperlich[1,3], Thomas Stahnke[1,3], Stephan Linke[4,5], Sanaz Farrokhi[4], Maren Klemm[4], Stephan Allgeier[6], Bernd Köhler[6], Klaus-Martin Reichert[6], Rudolf F. Guthoff[1,3], Sebastian Bohn[1,3], Oliver Stachs[1,3]

[1]Department of Ophthalmology, Rostock University Medical Center, Rostock, Germany; [2]Institute of Anatomy, Medical Faculty, University of Leipzig, Leipzig, Germany; [3]Department Life, Light & Matter, University of Rostock, Rostock, Germany; [4]Department of Ophthalmology, University Medical Center Hamburg-Eppendorf, Hamburg, Germany; [5]Zentrumsehstärke, Hamburg, Germany; [6]Institute for Automation and Applied Informatics, Karlsruhe Institute of Technology (KIT), Karlsruhe, Germany

[#]These authors contributed equally to this work.

Correspondence to: Dr. Katharina Sterenczak. Department of Ophthalmology, Rostock University Medical Center, Doberaner Straße 140, D-18057 Rostock, Germany. Email: katharina.sterenczak@med.uni-rostock.de.

Background: Regarding the growing interest and importance of understanding the cellular changes of the cornea in diseases, a quantitative cellular characterization of the epithelium is becoming increasingly important. Towards this, the latest research offers considerable improvements in imaging of the cornea by confocal laser scanning microscopy (CLSM). This study presents a pipeline to generate normative morphological data of epithelial cell layers of healthy human corneas.

Methods: 3D *in vivo* CLSM was performed on the eyes of volunteers (n=25) with a Heidelberg Retina Tomograph II equipped with an in-house modified version of the Rostock Cornea Module implementing two dedicated piezo actuators and a concave contact cap. Image data were acquired with nearly isotropic voxel resolution. After image registration, stacks of *en-face* sections were used to generate full-thickness volume data sets of the epithelium. Beyond that, an image analysis algorithm quantified *en-face* sections of epithelial cells regarding the depth-dependent mean of cell density, area, diameter, aggregation (Clark and Evans index of aggregation), neighbor count and polygonality.

Results: Imaging and cell segmentation were successfully performed in all subjects. Thereby intermediated cells were efficiently recognized by the segmentation algorithm while efficiency for superficial and basal cells was reduced. Morphological parameters showed an increased mean cell density, decreased mean cell area and mean diameter from anterior to posterior (5,197.02 to 8,190.39 cells/mm^2; 160.51 to 90.29 µm^2; 15.9 to 12.3 µm respectively). Aggregation gradually increased from anterior to posterior ranging from 1.45 to 1.53. Average neighbor count increased from 5.50 to a maximum of 5.66 followed by a gradual decrease to 5.45 within the normalized depth from anterior to posterior. Polygonality gradually decreased ranging from 4.93 to 4.64 sides of cells. The neighbor count and polygonality parameters exhibited profound depth-dependent changes.

Conclusions: This *in vivo* study demonstrates the successful implementation of a CLSM-based imaging pipeline for cellular characterization of the human corneal epithelium. The dedicated hardware in combination with an adapted image registration method to correct the remaining motion-induced image distortions followed by a dedicated algorithm to calculate characteristic quantities of different epithelial cell layers enabled the generation of normative data. Further significant effort is necessary to improve the algorithm for superficial and basal cell segmentation.

^ ORCID: 0000-0002-8122-4203.

Quant Imaging Med Surg 2021;11(5):1737-1750 | http://dx.doi.org/10.21037/qims-20-1052

Introduction

Modern ophthalmology evolved during the last decades from descriptive slit lamp-based findings to *in vivo* monitoring on the cellular level. During the past decades imaging technologies such as optical coherence tomography (OCT) became essential for the noninvasive *in vivo* diagnostics of the living eye—especially for the retinal diagnostics. Addressing the anterior segment (AS) of the eye, the AS-OCT technology enables quantitative as well as qualitative imaging including the cornea, limbus, anterior chamber and angle without the use of topical anesthesia (1). Based on advanced laser and spectrometer technologies during the past years, the axial resolution of OCT has been dramatically increased and thickness measurements of single corneal layers are available by ultrahigh-resolution OCT (2,3) as well as visualization of cellular and sub-cellular structures by spectral domain OCT (4). While OCT is very promising for corneal cross-sectional imaging, confocal laser scanning microscopy (CLSM) offers *en-face* imaging with high optical resolution and depth discrimination at the cellular level (1). Due to its axial resolution, selective intracorneal as well as intraepithelial sectioning can be achieved, and the different corneal epithelial cell-types can be distinguished (5). CLSM is suited for monitoring of the living cornea in its physiological state (6) permitting longitudinal examinations of the same cornea in normal and pathological conditions covering the entire ocular surface including the cornea, bulbar and palpebral conjunctiva and lids (1,7,8).

In general there is a number of CLSM based applications for the corneal diagnostic covering a broad range of applications including corneal nerve degeneration and regeneration, chirurgical interventions, contact lenses, diabetes mellitus (DM), keratoconus, keratomycosis, and ocular surface diseases (OSD) (1,8). The evaluation of the subbasal nerve plexus (SNP) of the cornea might add value to the diagnosis of a variety of diseases including limbal stem cell deficiency (LSCD), DM and infection (1). Until today, many studies have aimed in establishing of morphometric features of the SNP as a sensitive marker for ocular and systemic disorders (9,10).

Regarding OSDs, the cellular characterization of the corneal epithelial cell morphology is becoming increasingly important and recent studies have focused on understanding the microstructure of the epithelial cell layers in the cornea (11-13). Besides OSDs, in LSCD for example, a positive correlation between the reduction of basal cell density and the severity of LSCD was reported and basal cell density could be used as a parameter to measure limbal stem cell function at the early stages of the disease process (14,15). In DM, alterations in corneal innervation and basal cell density were reported and it could be demonstrated that reduced basal cell density correlated with changes in innervation (16).

Given the importance of understanding cellular changes in ophthalmological disorders such as OSDs or cellular changes that occur as secondary effects of diseases or treatment regimens, a CLSM-based 3D imaging and automated quantification pipeline could represent a powerful non-invasive tool providing valuable diagnostic information. CLSM has the ability to resolve structural and functional interrelationships, both temporally and spatially in the cornea. Cellular details of biological processes such as inflammation, wound healing, toxicity, and disease could be evaluated over time and help in the design of therapeutic strategies and the assessment of treatment effectivity.

The present study addresses the growing interest in quantitative data of the corneal epithelium and follows up on our initial study (13) that used 3D scanning techniques with fewer capabilities and required OCT data for epithelial thickness determination. The aim was to demonstrate a CLSM-based 3D *in vivo* image processing pipeline and an automated software for the morphological characterization and quantification of the different epithelial cell layers of the human corneal epithelium.

Methods

Confocal microscopy and volume data acquisition

To perform 3D *in vivo* CLSM, the Heidelberg Retina Tomograph II (HRTII, Heidelberg Engineering GmbH,
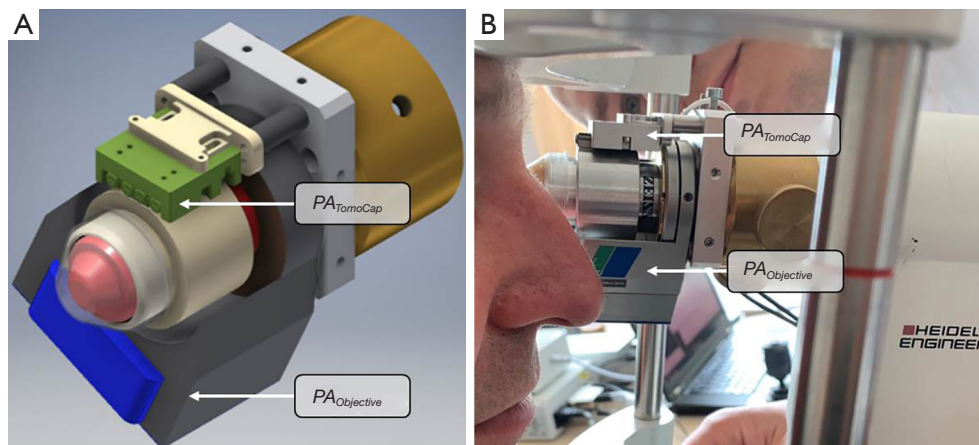
Figure 1 CAD model (A) and patient investigation (B) using the HRTII with an in-house-developed version of the RCM equipped with two piezo actuators: $PA_{Objective}$ with a closed-loop travel range of 500 µm and $PA_{TomoCap}$ with a rough travel range up to 12 mm to control the position of a TomoCap. Please note, $PA_{Objective}$ moves the objective lens and $PA_{TomoCap}$ the TomoCap.

Heidelberg, Germany) in combination with a modified version of the Rostock Cornea Module (RCM)—RCM 2.0—was used (RCM, Heidelberg Engineering GmbH, Heidelberg, Germany), see *Figure 1*. The in-house developed modified version of the RCM was previously presented as RCM 2.0 (12). There, the RCM was equipped with a piezo actuator with a closed-loop travel range of 500 µm (MIPOS 600 SG OEM, piezosystem jena GmbH, Jena, Germany). This actuator $PA_{Objective}$ moves a water immersion objective lens (Zeiss, Jena, Germany; 63 x/0.95 w, 670 nm, ∞/0) and enables a precise focus control. Additionally, the present study introduces a second piezo actuator $PA_{TomoCap}$ (SLC-1720-020-W-L; SmarAct GmbH, Oldenburg, Germany) to control the position of a contact element (TomoCap; Heidelberg Engineering, Heidelberg, Germany) during measurement. This allows the TomoCap to be moved in a controlled manner while in contact with the cornea in order to set the optimal starting focus position for achieving the largest possible height of the cornea stack and to minimize patient's examination time. As suggested in (12), a modified TomoCap is used to reduce lateral eye movements and applanation artifacts. The modified TomoCap has a concave surface with a diameter of 10 mm and a curvature radius of 7.8 mm, corresponding to the curvature of an average human cornea, thus creating a form closure with the cornea surface during *in vivo* CLSM (12).

The study included 25 volunteers (average age 44 years, ranging from 25 to 62 years) with normal corneas for investigation by *in vivo* CLSM. Exclusion criteria were: contact lens wear, keratoconus, and any corneal surgeries in

the past. Refraction error was not considered. In accordance with the Declaration of Helsinki, this study was conducted and explained in detail to all volunteers. Informed consent was obtained prior to conducting any investigative procedures.

A carbomer gel (Vidisic; Bausch & Lomb/Dr. Mann Pharma, Berlin, Germany) was used as the immersion medium. It was inserted between the objective lens and the TomoCap as well as between the TomoCap and the cornea. Before the immersion gel was applied to the cornea, a drop of topical anesthetic (Proparakain-POS; Ursapharm, Saarbrücken, Germany) was instilled. The immersion gel minimizes back reflections from interfaces, enables the high numerical aperture of the objective lens and thus improves the image quality.

The scans were performed in the central cornea and in both eyes of the respective test person. To acquire full-thickness volume data sets of the epithelium, we utilized the $PA_{TomoCap}$ to position the TomoCap so that the initial focus was slightly outside the cornea. Then, with the $PA_{Objective}$, the image focus was moved at a constant speed of 30 µm/s through the entire epithelium. During this through-focusing, the HRT acquired the images with 30 frames per second. The field of view of the images was 350 µm × 350 µm at 384 × 384 pixels. This resulted in a voxel resolution of 0.91 µm × 0.91 µm × 1 µm per voxel.

Image registration

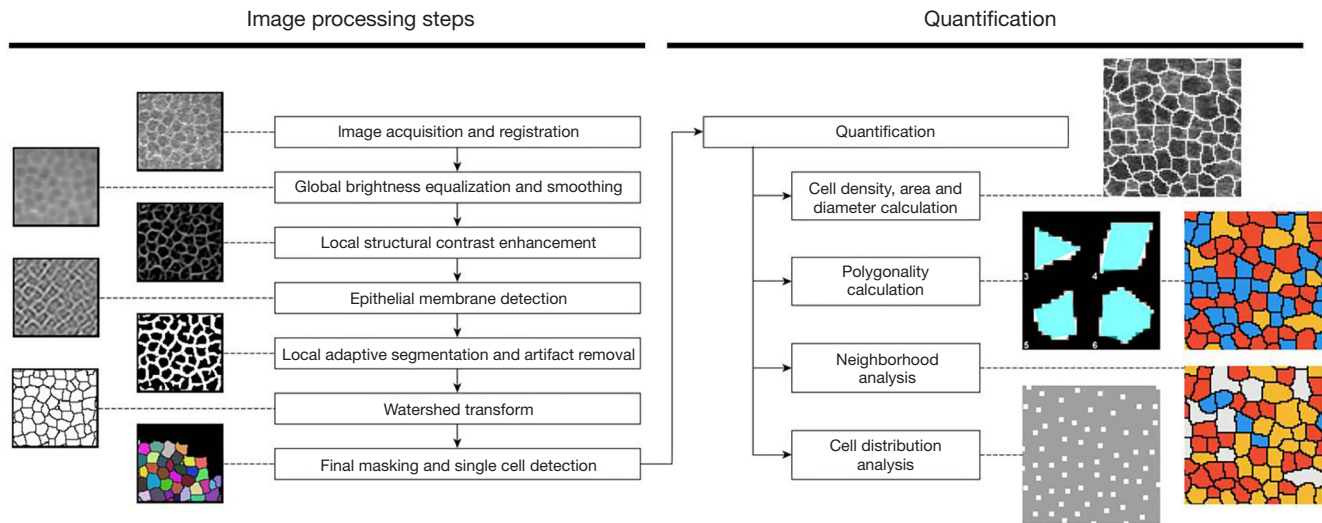It is well-known that during the fixation of a stationary

Figure 2 Schematic overview of all image processing (left side) and quantification (right side) steps: Image processing includes all methods needed for the detection of single cells from the original gray-scale images. Single cells were subsequently counted, quantified based on morphological parameters, and analyzed regarding their spatial relations.

target, the human eyes are continuously affected by small involuntary movements, commonly categorized as microsaccades, ocular drifts and ocular microtremors (17,18), ordered by decreasing amplitude. Because of the point-wise scanning of CLSM, these movements cause characteristic image distortion (13,19). The high-velocity microsaccades in particular lead to significant deformation of the cell shapes in the affected image data. Even though the curved contact cap effectively attenuates the eye movements, clearly visible motion artifacts are still present. In order to avoid adverse effects on cell characterization, the same motion-compensating image registration algorithm is used as in the previous study (13). The motion-corrected and aligned image frames are finally stacked to create a nearly isotropic volume representation.

Reconstruction of epithelium, automatic cell segmentation and quantification

Further image processing and analysis were performed using Mathematica (Version 12.0, Wolfram Research Inc., Champaign, IL, USA). *Figure 2* shows a schematic overview of the applied methods. Global brightness equalization was performed on all stack images to compensate varying image illumination ("vignette effect"). Equalized image stacks were smoothed with a 3×3×3 pixel wide 3D Gaussian filter (σ=1.5) to enhance transitions of cell membranes between adjacent volume slices. For each image slice, image noise was removed and local structural coherence of membranes (and other present structures) was amplified by using a ridge-detecting image filter ("RidgeFilter", σ=1). A bandpass filter for epithelial membrane detection was empirically designed ("BandpassFilter", cutoff frequencies of 0.28 and 1, filter kernel with a width of 62 pixels) and applied to all preprocessed images. This filter attenuates low (e.g., illumination gradients) and high (e.g., image noise) image frequencies while leaving the mid-range image frequencies (i.e., membranes and structures similar in diameter) unchanged. For each image stack, per pixel bandpass filter responses were summarized for individual images and normalized to respective image sizes. Resulting curves of depth-depending detection values were smoothed with a 3 pixel wide 1D mean filter and an empirically determined threshold value of 0.035 (representing images with still recognizable membranes) was applied to each curve to identify images from the epithelium of the respective image stack. Structure segmentation of all identified epithelial images was performed by local adaptive binarization (5×5 pixel wide window) and small artifacts were removed. Resulting binary images were inverted and a watershed transformation was performed for cell detection. Due to the vignette effect inherent to CLSM images of the cornea, contrast and visibility of the imaged cells decrease significantly towards the image borders. This property results

in a loss of cell detection quality with increasing distance from image centers. Therefore, a central circular area with a diameter of 250 pixels (corresponding to almost 0.041 mm^2) was defined around image centers and all cells outside this area were excluded from further processing and analysis.

Cross-sections of all detected epithelial cells were quantified and measurements were averaged for each image slice. Quantities included cell density (cells/mm^2), cell area (µm^2) and cell diameter (µm). Polygonality (sides) of cells was calculated by approximating polygons to cell shapes using a modified Ramer-Douglas-Peucker algorithm (20,21). The neighborhood count (n) was calculated based on the number of adjacent neighbors of each cell. Finally, cell patterns were analyzed based on the Clark-Evans aggregation index (CE-Index) (22).

For each parameter analyzed, data were separated by age group and functions were fitted within the defined intervals. Detailed ratios of neighborhood count and polygonality of cells across the defined interval were visualized in the form of stacked bar charts.

Results

Volume data acquisition, image registration

CLSM imaging with RCM 2.0 using two dedicated piezo stages enabled successful full-thickness volume data collection of the epithelium. Furthermore, the attenuation of the eye movements by the concave TomoCap led to registered image stacks with an increased lateral coverage. The median of the area projected into the x-y-plane, in which all registered images of a stack contain information was 45,723 µm^2 (min: 27,253 µm^2, max: 47,794 µm^2). Additionally, the integrated $PA_{TomoCap}$ accelerated the entire acquisition procedure by simplifying the adjustment of this cap prior to the start of the acquisition process.

All scans were manually checked for the presence of superficial cells (SCs) and the SNP, for contrast and the signal-to-noise ratio. In total 43 scans of 25 volunteers were used for the following segmentation and quantification procedures. The presence of SCs and the SNP allowed a definition of a normalized depth scale ranging from 0 to 1 (first SC =0, SNP =1) from anterior to posterior. Thereby the comparison of corresponding epithelial cell layers between the data sets independent of the actual epithelial thickness was possible. For the evaluation of a possible age dependency, the 25 volunteers were divided into three age groups: Group 1: 20–35 years (n=10); group 2: 36–55 years

(n=9) and group 3: 56–70 (n=6).

Reconstruction of the corneal epithelium

The 3D reconstruction and segmentation of the corneal epithelial cell layers was performed for all scans (*Figure 3*). Visual inspection of the image registration results revealed good alignment performance with no visible errors in the regions from the SNP through the basal and intermediate epithelium. Several visible distortion artifacts, mainly caused by overexposed regions, were found in a few superficial images. Individual characteristic cell layers including superficial, upper wing, lower wing-, and basal cells could be reconstructed in 3D (*Figure 3B*). The developed automatic segmentation algorithm did not work efficiently for superficial and deeper regions of basal cells. Therefore, manual segmentation for one scan was performed to visualize the extreme changes in morphology from anterior (SCs) to posterior (basal cells). Thereby, the mean cell areas ranged from 1,121.8 to 57.2 µm^2 and mean cell diameters ranged from 39.5 to 8.9 µm (*Figure 3C*).

Automated segmentation and quantification

Figure 4 shows an overview of the data collected for the study and used for quantification. Because of individual differences of the epithelial thickness, the interslice distance varied between the datasets when expressed in normalized depth coordinates. Depth dependent cell characteristics could be exemplified for all analyzed scans (*Figure 5*). The segmentation algorithm worked reliably within the upper and lower wing cell area covering 70–95% of the available image sections, while the percentage of available image data went down within superficial and basal cell area (*Figure 5A*).

Segmented cells were color-coded depending on the number of surrounding neighbors (*Figure 5D*) and the polygonality (*Figure 5E*). Depending on the depth from anterior to posterior, changes of the color-patterns could be observed (*Figure 5D,E*). The corresponding values are summarized in *Figure 5F*. Depth depending changes were present in the number of surrounding neighbors and the polygonality showing different morphological characteristics.

Repeatability of measurements

In advance of the study, we have performed repeated scans of volunteers and analyzed the data respectively. An
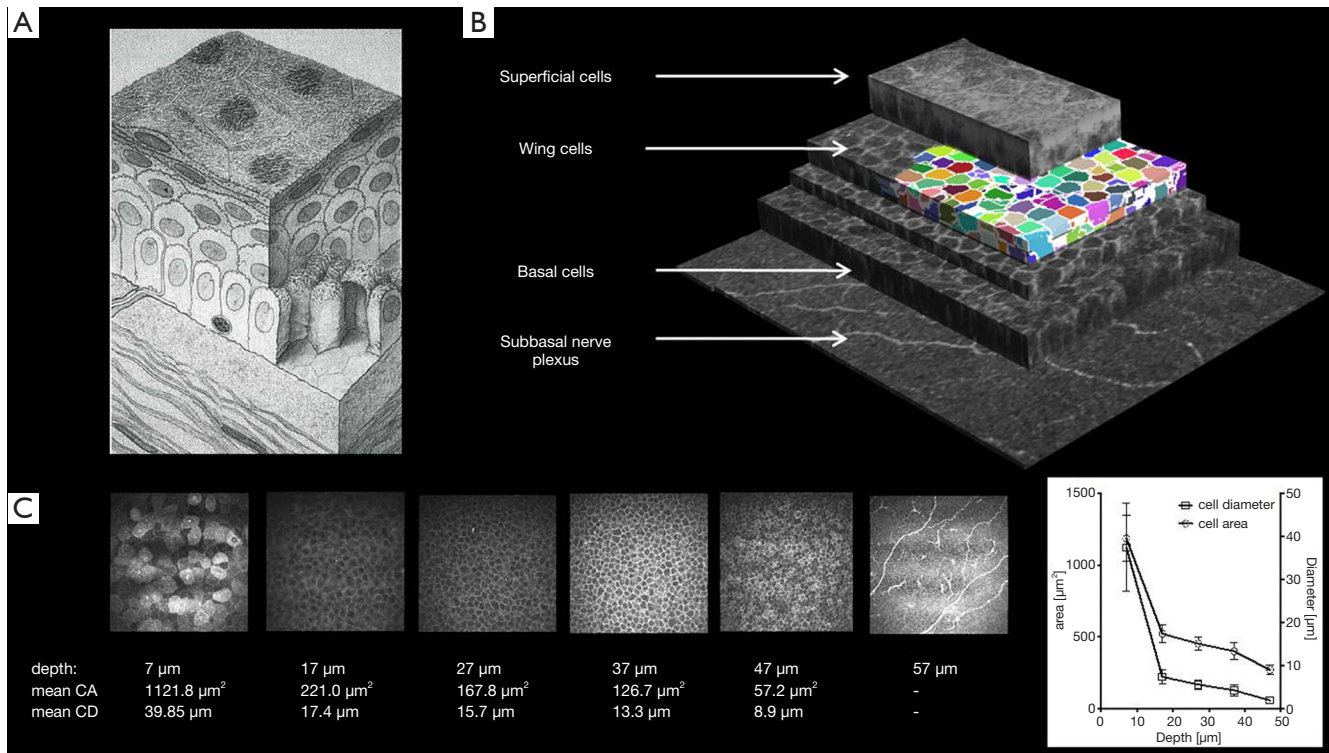
Figure 3 Reconstruction and segmentation of the corneal epithelial cell layers. Corneal epithelium sketch (A) (23) and corneal image stack with cut-outs according to figure (A) recorded with the concave TomoCap in isometric view using KIT- alignment (B) (19). Each of the cells were colored individually after segmentation and 3D reconstruction. (C) Selected images of a stack are shown, exemplifying the typical depth depending cell morphology ranging from the outer superficial cells (depth 7 µm) to basal cells (depth 47 µm). Using manual segmentation, mean cell areas (CA) ranged from 1,121.8 to 57.2 µm^2 and mean cell diameters (CD) ranged from 39.85 to 8.9 µm. Furthermore a graph of the determined values for area and diameter by manual segmentation is shown.

averaged coefficient of variation was determined. In order to exemplify the error range, four independent depth scans of one volunteer were performed and used for automated segmentation, quantification and analysis of variation. The mean coefficient of variation was found for each parameter using the data of successful segmented areas: cell density 0.040; cell area 0.045; cell diameter 0.022; CE-Index 0.005; neighbor count 0.005; polygonality count 0.004.

Generation of normative data

Figure 6 shows the analyzed quantities for the respective parameters (column A: total mean values; column B: age-dependent mean values). In *Table 1* the analyzed parameters and in *Table 2* total mean values are listed.

The neighborhood and polygonality parameters were additionally evaluated according to their percentage of distribution from anterior to posterior for all analyzed scans (*Figure* 7). Depth-dependent changes in the number of neighbors and the polygonality of cells were detected confirming the morphological characteristics within the different layers of the corneal epithelium.

Conclusions

The morphological characterization and quantification as well as the understanding of the proliferative and differentiation behavior of the different corneal epithelial cell layers is of clinical relevance as changes affecting corneal cells and nerves are not only characteristic for unified corneal pathologies but also reflect non-specific pathological processes present in many diseases.

Anatomically, the healthy human corneal epithelium consists of five to six layers of nucleated cells which
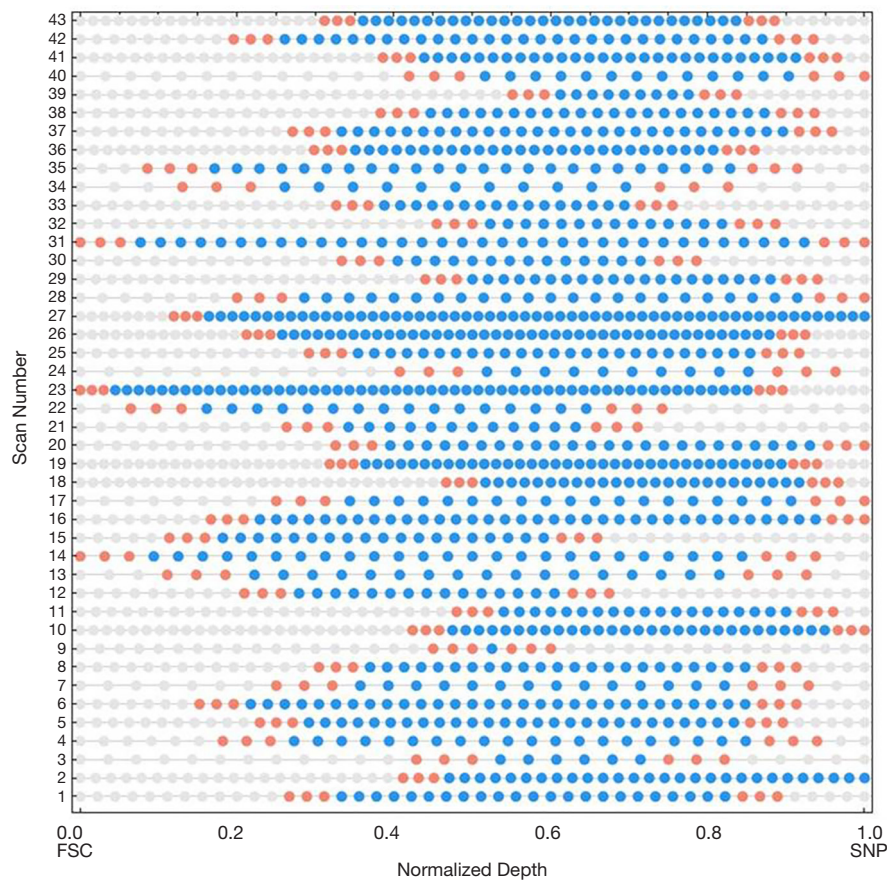
Figure 4 Overview of the data collected for the study and used for quantification: The epithelial thickness was normalized to 1 starting from the first superficial cell (FSC) [0] to the center of the SNP [1]. The definition of start [0] and end [1] point was done by the investigator. Differences in epithelial thickness are causing non-equidistant interslice distance. Blue points represent image slices which have been assigned to the layers of the epithelium with certainty by the algorithm software and which were available for automated quantification. Orange points represent the three image safety margin slices applied by the software and grey points represent image slices which could not be detected by the software with certainty and which were not available for quantification.

were categorized into SCs, intermediate cells and basal cells according to their functionality and morphology. During both, homeostasis and wound healing, the corneal epithelium is in a constant state of self-renewing and a complete turnover occurs in approx. 5 to 7 days. The epithelium is thereby maintained by basal cells which are the source of wing and SCs and a delicate balance of shedding followed by proliferation is critical in maintaining a smooth and uniform epithelial surface (24).

SCs are characterized by a polygonal cell pattern, bright illuminated cytoplasm, reflecting nuclei and perinuclear dark halo (25) and appear brighter in CLSM images than cells towards the posterior of the cornea (26). About 1/7 of these cells are lost by desquamation within 24 hrs with a

precedent change in their optical characteristics (25) with the darker ones being those about to desquamate from the surface (27). The intermediate layer is composed of wing cells. These cells form a regular mosaic of cells with sharp and reflecting cell borders showing the same reflectivity as SCs (8,28). However, their cell nuclei are not well defined and the cytoplasm appears dark (24). They are smaller in size when compared to SCs but more regular in form, and they can be further subdivided according to their position into upper and lower wing cells, with the latter being smaller. The innermost part of the epithelium is formed by a monolayer of basal cells. These cells show the smallest diameter when compared to the layers above and have a cylindrical, columnar form (25,28). They display a uniformly
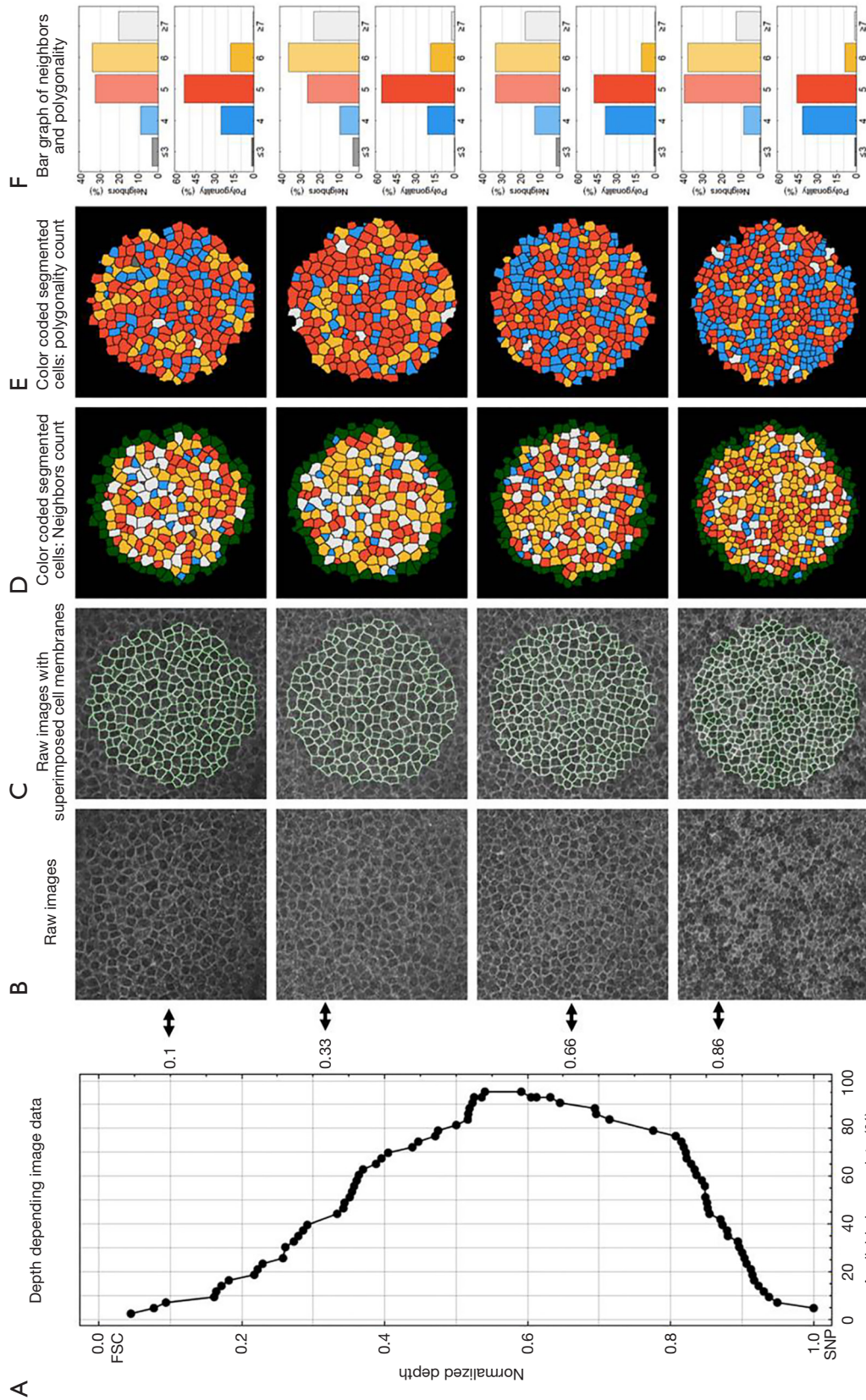
Figure 5 Depth dependent cell characteristics for all analyzed scans. Images from different interval positions with corresponding image data availability and quantification algorithm: Percentage of available image data of all investigated scans depending on normalized depth and the according epithelial cell layers (A,B). Original image with superimposed cell membranes (C), color-coded neighbor counts (≥7: white; 6: orange; 5: red; 4: blue; ≤3: grey) (D), color-coded polygonality (≥7: white; 6: orange; 5: red; 4: blue; ≤3: grey) (E) and bar graphs for neighbor counts and polygonality (F) (top and bottom, respectively).
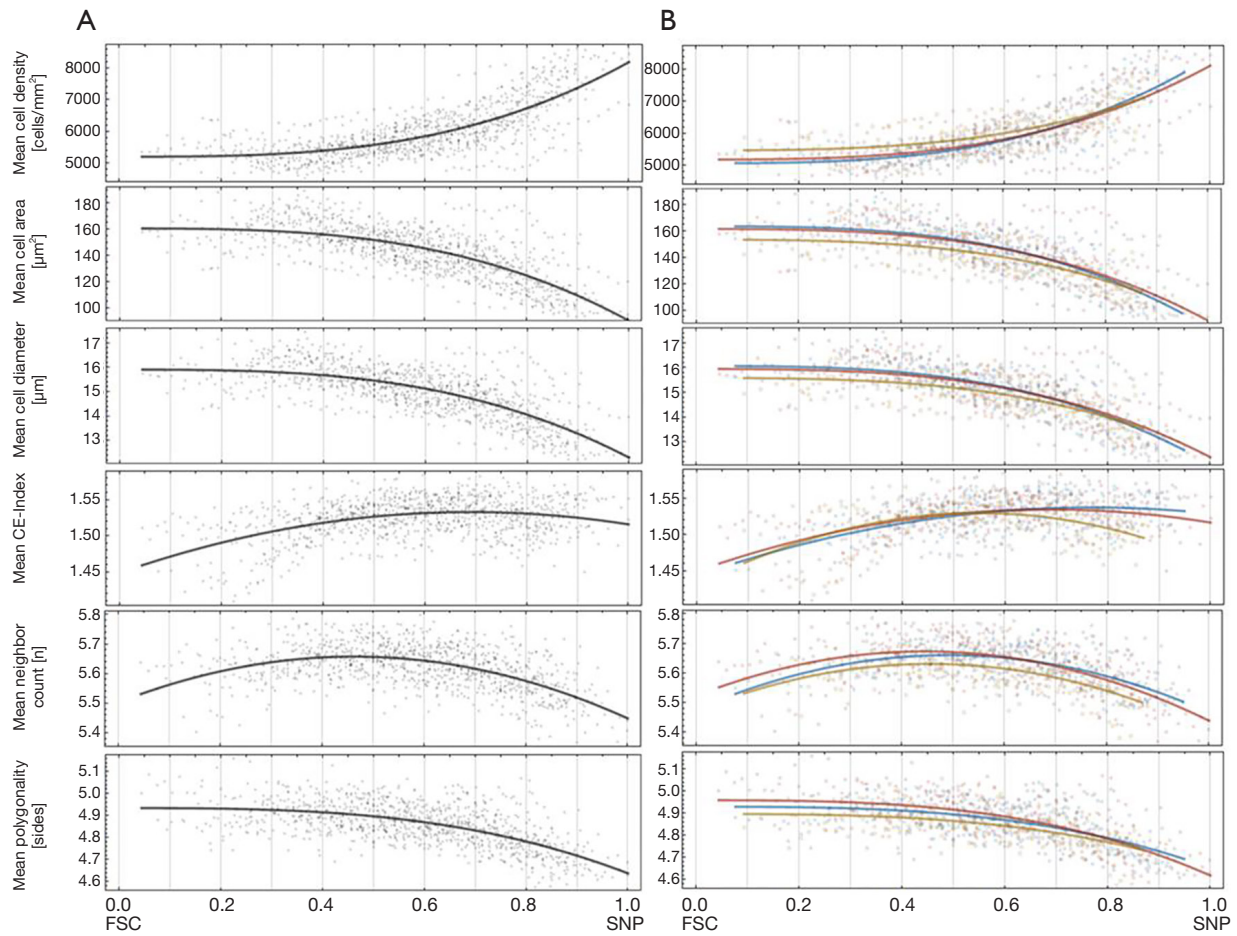
Figure 6 Characteristic quantities of corneal epithelial structures. Left column from top to bottom: mean of cell density, cell area, cell diameter, CE-Index, neighbor count and polygonality plotted against normalized scale. Right column from top to bottom: same parameters as left, but for different age groups. Age group definition was as follows: 20–25 years (orange); 36–55 years (olive); 56–70 years (blue).

Table 1 Summary of quantified epithelial cell parameters

Parameters	Definition
Cell density	Number of cells per mm^2 (cells/mm^2)
Cell area	Number pixels x area of a pixel (μm^2)
Cell diameter	Length of a straight line passing through the center of a cell (μm)
CE-Index	Pattern of cell centroids
Neighbor count	Number of adjacent neighbors of each cell
Polygonality	Number of sides of a cell

Cross-sections of epithelial cells were quantified using appropriate image analysis algorithms.

Table 2 Interpolated values of epithelial cell parameters

Interval position normalized depth	Mean cell density (cells/mm²)	Mean cell area (µm²)	Mean cell diameter (µm)	Mean CE-Index	Mean neighbor count (n)	Mean polygonality (sides)
0	5,197.02	160.51	15.90	1.45	5.50	4.93
0.1	5,200.01	160.44	15.90	1.47	5.56	4.93
0.2	5,220.97	159.95	15.87	1.49	5.61	4.93
0.3	5,277.84	158.62	15.81	1.51	5.64	4.93
0.4	5,388.60	156.02	15.67	1.52	5.65	4.92
0.5	5,571.19	151.74	15.45	1.53	5.66	4.90
0.6	5,843.59	145.35	15.12	1.53	5.64	4.87
0.7	6,223.75	136.43	14.67	1.53	5.62	4.83
0.8	6,729.63	124.56	14.06	1.53	5.58	4.78
0.9	7,379.19	109.32	13.28	1.53	5.52	4.72
1	8,190.39	90.29	12.30	1.52	5.45	4.64

Cross-sections of epithelial cells were quantified using appropriate image analysis algorithms. The scale between first superficial cell (FSC) to subbasal nerve plexus (SNP) was normalized from 0 to 1 (FSC =0, SNP =1; increment: 0.1).
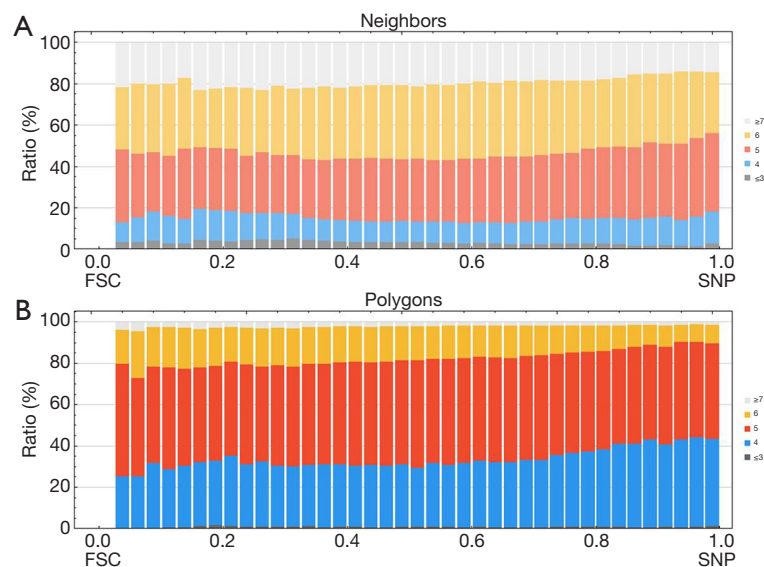

Figure 7 Distribution of neighbor count (A) and polygonality (B): stacked bar-charts show the variability in percentage of distribution from anterior to posterior for all analyzed scans.

bright cell border with dark cytoplasmic mass (27). Besides stem cells and transient amplifying cells, they are the only corneal epithelial cells capable of mitosis (29). During the renewing process of the corneal epithelium, the basal cells differentiate and migrate vertically towards the anterior surface to repopulate the cornea (30).

The present study represents a further development of a fully automated software tool for epithelial cell quantification. Compared to our former publication (13), the detection of epithelial cells was improved due to global brightness equalization and local structural contrast amplification in combination with bandpass-

based membrane detection. The segmentation results reveal that efforts for further improvements on cell segmentation should be focused at the challenging regions of the superficial and deep sections of basal cells in order to provide automated cell characterization for the entire extent of the corneal epithelium. In addition to the cell features examined in the previous study (13), we have also introduced new parameters including density, aggregation (CE-Index), the count of surrounding cells and the polygonality of cells.

The mean cell densities gradually increased from anterior to posterior corresponding to the above-mentioned characteristics of the three different cell zones of the epithelium. Starting from the surface with the SCs and moving towards to the SNP, the cell morphology changes in size and shape from large but flat polygonal cells (SCs) to thin but long cylindrical cells (basal cells) and consequently their density in cross-sections increases. Comparison of our results with Eckard *et al.* (26) showed a general agreement regarding intermediate and basal cell layers. It must be mentioned that in our study the algorithm did not work sufficiently for SCs and the lowest parts of the basal cells located directly above the Bowman's membrane where the highest density is expected (8,25). Regarding cell area, Prakasam *et al.* (13) reported a linear decrease from anterior to posterior which could be confirmed in this study while similarities and differences with other studies have already been discussed there. The minimal differences within the basal cell area were probably caused by the fact, that in the former evaluation the membranes were segmented comparatively thicker due to lower image quality and thus the minimum size was slightly lower.

The comparison of the herein performed manual count *vs.* the segmentation algorithm showed similar values in the depth range between 27 and 47 µm of the analyzed scan representing the wing cell area and the upper part of the basal cells. Furthermore, the manually determined values were in accordance with other published works like by Gaujoux *et al.* (11).

The analyzed mean cell diameters showed a gradual decrease from anterior to posterior thereby showing comparable results to our previous study (13). When the herein performed manual count is compared with the segmentation algorithm, the values are comparable within the wing cells and could show comparable trends to former studies as well (13,25,31).

The analyzed CE-Index showed a gradual increase from anterior to posterior displaying a regular distribution of the

cells. In future studies, it would be important to evaluate whether this parameter also changes in pathologies of the corneal epithelium.

Regarding the number of neighbors surrounding a cell, the analysis demonstrated depth-dependent changes. In the majority, cells were surrounded by either 5 or 6 neighbors and fluctuations were detected in the front part and further downstream from point 0.75 towards 1 within the normalized depth. The variations in the anterior section may have been caused by the limited data available while the percentage of available image data within middle and posterior section accounted for between 40% to 90%. It appears that there was a structural change in the section 0.75 of the normalized depth, i.e., the transition from lower wing cells to basal cells.

The polygonality of cells decreased from anterior to posterior confirming the previously described characteristic of the epithelial cell shapes changing from polygonal to cylindrical cells. The predominant shape of the cells was pentagonal with the relative amount decreasing towards the SNP. The second-most dominant shape was represented by quadrangular cells. Here the percentage remained stable at 30% while after section 0.75 of the normalized depth the relative amount rose to a maximum of 45% indicating the transition zone between lower wing cells and basal cells. However, it must be considered that SCs are the only cells that can be displayed in their entirety. In contrast, wing cells are arranged like roof tiles and with only part of their cell surface accessible in one section, thus influencing the analysis of all the above-mentioned parameters. Nevertheless, within this study we were able to present normative data for future comparison with data analyzed in pathologies of the corneal epithelium.

We have divided our subjects into three age groups whereas no age dependency was found. However, there are studies reporting age dependency in the human cornea. Zheng *et al.* examined 80 subjects and found age-related changes in peripheral basal epithelial cell density and in peripheral basal endothelial cell density. It must be mentioned that a significance was only found within the youngest age group (32). Gambato *et al.* (33) reported an increase in cell diameter of superficial epithelial cells with subject age while basal epithelium and the SNP did not change depending on age in the 108 subjects studied (33). On the other hand, based on a study with 45 subjects, Mustonen *et al.* (34) reported no statistically significant correlation between superficial and basal epithelial cell density or age. Furthermore, no statistically significant differences

in cell densities or cell areas of any corneal layer between gender nor between left or right eyes were reported (34). Eckard *et al.* (26) reported no statistically significant relationship between cell densities and age, sex or refraction as well in 68 subjects examined. In summary, all these studies mentioned above show controversial results.

It should be considered that our number of analyzed subjects was smaller when compared with all of the above-mentioned studies. The question of whether a larger number of test persons examined further increases the significance of the normative data cannot be answered unequivocally. On the one hand, it can be assumed that an increased number of subjects improves the significance, but on the other, we postulate that newly determined quantities would be within the already determined quantity ranges. From our point of view, it is imperative to first improve the imaging strategy and the cell segmentation tools for superficial and deeper basal cell sections and then, in a second step, to increase the size of the normative cohort with these improved tools. However, the segmentation of SCs requires completely different tools that have yet to be developed.

As an outlook to possible future algorithmic developments, the 3D reconstructions could be potentially used for 3D characterization by volumetric cell features. However, even though the 3D reconstruction process achieves good structural coherence between adjacent images, the anisotropic optical resolution of the CLSM volumes presents a challenge for the segmentation and quantification algorithms. We have an almost isotropic voxel resolution of 0.91 µm × 0.91 µm × 1 µm per voxel, but the optical resolution differs significantly between the z-direction (about 4 µm) and the *en-face* directions (about 1 µm) (35). Due to this, a reliable 3D segmentation and quantification of epithelial cells based on current data was not feasible.

This *in vivo* study demonstrates a CLSM-based imaging pipeline for cellular characterization of the human corneal epithelium. The concave contact cap and the integration of a second, large travel-range piezo actuator significantly improved the usability of this method. Furthermore, characteristic quantities of different epithelial cell layers were presented, whereas no age dependency was found. Given the growing interest and the importance of understanding the cellular changes in ophthalmological disorders or disorders which were described to affect cornea's morphology as well, a non-invasive *in vivo* CLSM-based imaging and quantification pipeline could serve as a

powerful diagnostic tool and thereby improve the evaluation of therapeutic regimens. Changes in the herein analyzed parameters could be evaluated over longer periods of time and help in the understanding of underlying biological processes such as inflammation and wound healing. Moreover, longitudinal analyses of these parameters could help in the assessment of treatment efficacy and regeneration of the cornea. The data gained herein could serve as a first step to generate more normative epithelial data towards further investigations. Further significant effort is necessary to improve the algorithm for superficial and basal cell segmentation.

Acknowledgments

Footnote

Conflicts of Interest: All authors have completed the ICMJE uniform disclosure form (available at http://dx.doi.org/10.21037/qims-20-1052). Dr. KAS reports grants from German Federal Ministry of Education and Research, during the conduct of the study; Dr. KS reports grants from Deutsche Forschungsgemeinschaft (DFG, German Research Foundation), during the conduct of the study; Dr. TS reports grants from German Federal Ministry of Education and Research, during the conduct of the study; Dr. SA reports grants from Deutsche Forschungsgemeinschaft (DFG, German Research Foundation), during the conduct of the study; Dr. BK reports grants from Deutsche Forschungsgemeinschaft (DFG, German Research Foundation), during the conduct of the study; SB reports grants from Deutsche Forschungsgemeinschaft (DFG, German Research Foundation), during the conduct of the study. The other authors have no conflicts of interest to declare.

Ethical Statement: The study protocol was approved by the Institutional Review Board [Rostock University Medical Center Ethics Committee, Registration number: A 2018-0162 (dated 23 August 2018)]. All study procedures followed the tenets of the Declaration of Helsinki, and informed

consent was obtained from all subjects before enrollment.

Open Access Statement: This is an Open Access article distributed in accordance with the Creative Commons Attribution-NonCommercial-NoDerivs 4.0 International License (CC BY-NC-ND 4.0), which permits the non-commercial replication and distribution of the article with the strict proviso that no changes or edits are made and the original work is properly cited (including links to both the formal publication through the relevant DOI and the license). See: https://creativecommons.org/licenses/by-nc-nd/4.0/.

References

1. Bille JF, editor. High Resolution Imaging in Microscopy and Ophthalmology: New Frontiers in Biomedical Optics. Springer International Publishing; 2019.

2. Bizheva K, Tan B, MacLelan B, Kralj O, Hajialamdari M, Hileeto D, Sorbara L. Sub-micrometer axial resolution OCT for in-vivo imaging of the cellular structure of healthy and keratoconic human corneas. Biomed Opt Express 2017;8:800-12.

3. Werkmeister RM, Sapeta S, Schmidl D, Garhöfer G, Schmidinger G, Aranha Dos Santos V, Aschinger GC, Baumgartner I, Pircher N, Schwarzhans F, Pantalon A, Dua H, Schmetterer L. Ultrahigh-resolution OCT imaging of the human cornea. Biomed Opt Express 2017;8:1221-39.

4. Tan B, Hosseinaee Z, Han L, Kralj O, Sorbara L, Bizheva K. 250 kHz, 1.5 μm resolution SD-OCT for in-vivo cellular imaging of the human cornea. Biomed Opt Express 2018;9:6569-83.

5. Petroll WM, Robertson DM. In Vivo Confocal Microscopy of the Cornea: New Developments in Image Acquisition, Reconstruction, and Analysis Using the HRT-Rostock Corneal Module. Ocul Surf 2015;13:187-203.

6. Erie JC, McLaren JW, Patel SV. Confocal Microscopy in Ophthalmology. Am J Ophthalmol 2009;148:639-46.

7. Zhivov A, Guthoff RF, Stachs O. In vivo confocal microscopy of the ocular sur-face: from bench to bedside and back again. Br J Ophthalmol 2010;94:1557-8.

8. Zhivov A, Stachs O, Kraak R, Stave J, Guthoff RF. In vivo confocal microscopy of the ocular surface. Ocul Surf 2006;4:81-93.

9. Al-Aqaba MA, Dhillon VK, Mohammed I, Said DG, Dua HS. Corneal nerves in health and disease. Prog Retin Eye Res 2019;73:100762.

10. Kokot J, Wylęgała A, Wowra B, Wójcik Ł, Dobrowolski

D, Wylęgała E. Corneal confocal sub-basal nerve plexus evaluation: a review. Acta Ophthalmol 2018;96:232-42.

11. Gaujoux T, Touzeau O, Laroche L, Borderie VM. Morphometry of corneal ep-ithelial cells on normal eyes and after anterior lamellar keratoplasty. Cornea 2010;29:1118-24.

12. Bohn S, Sperlich K, Allgeier S, Bartschat A, Prakasam R, Reichert KM, Stolz H, Guthoff R, Mikut R, Köhler B, Stachs O. Cellular in vivo 3D imaging of the cornea by confocal laser scanning microscopy. Biomed Opt Express 2018;9:2511-25.

13. Prakasam RK, Winter K, Schwiede M, Allgeier S, Zhivov A, Köhler B, Guthoff RF, Stachs O. Characteristic quantities of corneal epithelial structures in confocal laser scanning microscopic volume data sets. Cornea 2013;32:636-43.

14. Le Q, Xu J, Deng SX. The diagnosis of limbal stem cell deficiency. Ocul Surf 2018;16:58-69.

15. Chan EH, Chen L, Rao JY, Yu F, Deng SX. Limbal Basal Cell Density Decreases in Limbal Stem Cell Deficiency. Am J Ophthalmol 2015;160:678-84.e4.

16. Chang PY, Carrel H, Huang JS, Wang IJ, Hou YC, Chen WL, Wang JY, Hu FR. Decreased density of corneal basal epithelium and subbasal corneal nerve bundle changes in patients with diabetic retinopathy. Am J Ophthalmol 2006;142:488-90.

17. Bowers NR, Boehm AE, Roorda A. The effects of fixational tremor on the ret-inal image. J Vis 2019;19:8.

18. Martinez-Conde S, Macknik SL, Hubel DH. The role of fixational eye move-ments in visual perception. Nat Rev Neurosci 2004;5:229-40.

19. Allgeier S, Zhivov A, Eberle F, Koehler B, Maier S, Bretthauer G, Guthoff RF, Stachs O. Image reconstruction of the subbasal nerve plexus with in vivo confocal microscopy. Invest Ophthalmol Vis Sci 2011;52:5022-8.

20. Ramer U. An iterative procedure for the polygonal approximation of plane curves. Comput Graph Image Process 1972;1:244-56.

21. Douglas DH, Peucker TK. Algorithms for the reduction of the number of points required to represent a digitized line or its caricature. Cartogr Int J Geogr Inf Geo-visualization 1973;10:112-22.

22. Clark PJ, Evans FC. Distance to Nearest Neighbor as a Measure of Spatial Re-lationships in Populations. Ecology 1954;35:445-53.

23. Guthoff RF, Baudouin C, Stave J. General Anatomical Considerations. In: Atlas of Confocal Laser Scanning In-vivo Microscopy in Ophthalmology. Berlin, Heidel-berg:

Springer, 2006.

24. Levin LA, Nilsson SFE, Ver Hoeve J, Wu SM, Kaufman PL. Cornea and Sclera. In: Adler's Physiology of the Eye E-Book. Elsevier Health Sciences, 2011.

25. Guthoff RF, Zhivov A, Stachs O. In vivo confocal microscopy, an inner vision of the cornea - a major review. Clin Exp Ophthalmol 2009;37:100-17.

26. Eckard A, Stave J, Guthoff RF. In vivo investigations of the corneal epithelium with the confocal Rostock Laser Scanning Microscope (RLSM). Cornea 2006;25:127-31.

27. Tavakoli M, Hossain P, Malik RA. Clinical applications of corneal confocal microscopy. Clin Ophthalmol 2008;2:435-45.

28. Guthoff RF, Stave J. In Vivo Micromorphology of the Cornea: Confocal Mi-croscopy Principles and Clinical Applications. In: Reinhard T., Larkin D. (eds) Cornea and External Eye Disease. Essentials in Ophthalmology. Berlin, Heidelberg: Springer, 2006;173-208.

29. DelMonte DW, Kim T. Anatomy and physiology of the cornea. J Cataract Refract Surg 2011;37:588-98.

30. Eghrari AO, Riazuddin SA, Gottsch JD. Overview of the Cornea: Structure, Function, and Development. Prog Mol Biol Transl Sci 2015;134:7-23.

31. Beuerman RW, Pedroza L. Ultrastructure of the human cornea. Microsc Res Tech 1996;33:320-35.

32. Zheng T, Le Q, Hong J, Xu J. Comparison of human corneal cell density by age and corneal location: an in vivo confocal microscopy study. BMC Ophthalmol 2016;16:109.

33. Gambato C, Longhin E, Catania AG, Lazzarini D, Parrozzani R, Midena E. Aging and corneal layers: an in vivo corneal confocal microscopy study. Graefes Arch Clin Exp Ophthalmol 2015;253:267-75.

34. Mustonen RK, McDonald MB, Srivannaboon S, Tan AL, Doubrava MW, Kim CK. Normal human corneal cell populations evaluated by in vivo scanning slit confocal microscopy. Cornea 1998;17:485-92.

35. Heidelberg Retina Tomograph 2 Operating Instructions of Software Ver-sion 1.1. Dossenheim Germany: Heidelberg Engineering GmbH, 2004.

Danksagung

An dieser Stelle möchte ich allen Leuten danken, die mich in den letzten Jahren auf dem Weg zum Abschluss meiner Dissertation begleitet und unterstützt haben. Großer Dank gilt dabei Herrn Prof. Dr. Heinrich Stolz, der mir diese Arbeit ermöglichte und als Betreuer für Fragen immer zur Verfügung stand. Ebenso möchte ich Prof. Dr. Oliver Stachs für die Aufnahme in die Arbeitsgruppe Experimentelle Ophthalmologie der Augenklinik der Universitätsmedizin Rostock danken sowie für die unzähligen Ratschläge und die anhaltende Motivation. An alle Mitarbeiterinnen und Mitarbeiter der Augenklink sei ein großes Dankeschön für das durchweg angenehme Arbeitsklima gerichtet. Besonders möchte ich Dr. Katharina Anna Sterenczak, Dr. Thomas Stahnke und Prof. Dr. Rudolf F. Guthoff für ihre Expertise bei biologischen und medizinischen Themen sowie die immer netten und aufschlussreichen Unterhaltungen danken. Ein riesen Dankeschön geht an Dr. Karsten Sperlich, der immer für Fragen aller Art offen war und stets mit konstruktiver Kritik das Beste aus meinen Leistungen hervorbrachte. Ein ausdrückliches Dankeschön gilt Herrn Prof. Dr. Joachim Stave, der mir und der Weiterentwicklung seiner Erfindung mit viel Freude und Interesse entgegen kam. Auch den Kollegen Klaus-Martin Reichert, Dr. Stephan Allgeier, Dr. Bernd Köhler, Andreas Bartschat und Prof. Dr. Ralf Mikut vom Karlsruher Institut für Technologie möchte ich für die Zusammenarbeit danken, welche großartige Ergebnisse hervorbrachte. Weiterhin möchte ich der feinmechanischen Werkstatt des Instituts für Physik für ihre hervorragende Arbeit bei der Fertigung diverser Komponenten und für ihre technischen Ratschläge danken. Zu guter Letzt möchte ich meinen Freunden und meiner Familie danken, die immer an mich geglaubt haben und hinter mir standen. Ohne euch wäre diese Arbeit niemals möglich gewesen.

Selbstständigkeitserklärung

Hiermit versichere ich, dass ich diese Arbeit selbstständig verfasst und keine anderen als die angegeben Hilfsmittel und Quellen verwendet habe. Stellen, die anderen Werken wörtlich oder inhaltlich entnommen sind, wurden mit angegebener Quelle kenntlich gemacht.

Rostock, 18. Februar 2022

Sebastian Bohn